

DTIC FILE COPY

4

RADC-TR-89-67  
Final Technical Report  
June 1989

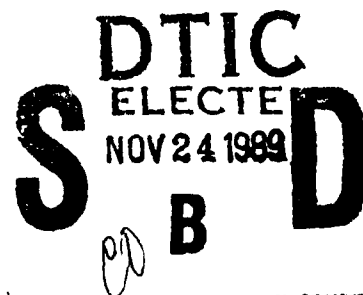


AD-A215 033

## OPTO-EM AND DEVICES INVESTIGATION

Parke Mathematical Laboratories, Inc.

J. A. Adamski, J. H. Bloom, H. J. Caulfield, J. J. Comer, R. S. Kennedy,  
J. D. Klerstead, M. Salour

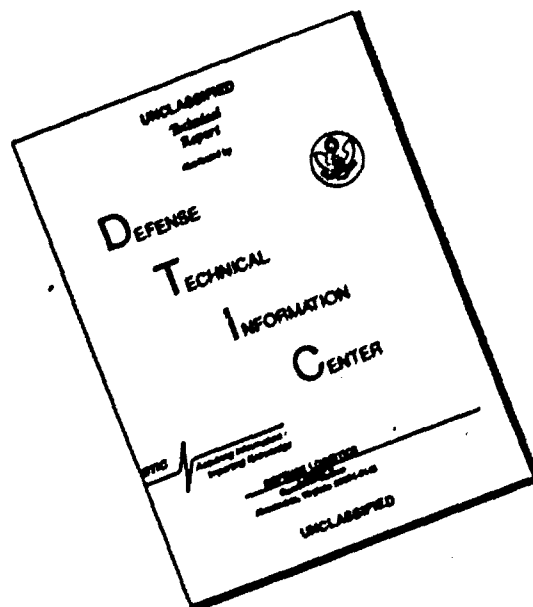


APPROVED FOR PUBLIC RELEASE; DISTRIBUTION UNLIMITED.

ROME AIR DEVELOPMENT CENTER  
Air Force Systems Command  
Griffiss Air Force Base, NY 13441-5700

89 11 21 127

# DISCLAIMER NOTICE



THIS DOCUMENT IS BEST QUALITY AVAILABLE. THE COPY FURNISHED TO DTIC CONTAINED A SIGNIFICANT NUMBER OF PAGES WHICH DO NOT REPRODUCE LEGIBLY.

UNCLASSIFIED

SECURITY CLASSIFICATION OF THIS PAGE

REPORT DOCUMENTATION PAGE				Form Approved OMB No. 0704-0188	
1a. REPORT SECURITY CLASSIFICATION Unclassified			1b. RESTRICTIVE MARKINGS N/A		
2a. SECURITY CLASSIFICATION AUTHORITY N/A			3. DISTRIBUTION/AVAILABILITY OF REPORT Approved for public release; distribution unlimited.		
2b. DECLASSIFICATION/DOWNGRADING SCHEDULE N/A					
4. PERFORMING ORGANIZATION REPORT NUMBER(S) N/A			5. MONITORING ORGANIZATION REPORT NUMBER(S) RADC-TR-89-67		
6a. NAME OF PERFORMING ORGANIZATION Parke Mathematical Laboratories Inc		6b. OFFICE SYMBOL (if applicable)	7a. NAME OF MONITORING ORGANIZATION Rome Air Development Center (ESOP)		
6c. ADDRESS (City, State, and ZIP Code) 1 River Road P O Box A Carlisle MA 01741			7b. ADDRESS (City, State, and ZIP Code) Hanscom AFB MA 01731-5000		
8a. NAME OF FUNDING / SPONSORING ORGANIZATION Rome Air Development Center		8b. OFFICE SYMBOL (if applicable) ESOP	9. PROCUREMENT INSTRUMENT IDENTIFICATION NUMBER F19628-87-C-0155		
8c. ADDRESS (City, State, and ZIP Code) Hanscom AFB MA 01731-5000			10. SOURCE OF FUNDING NUMBERS		
			PROGRAM ELEMENT NO. 62702F	PROJECT NO. 4600	TASK NO. 19
11. TITLE (Include Security Classification) OPTO-FM AND DEVICES INVESTIGATION					
12. PERSONAL AUTHOR(S) J.A. Adamski, J.H. Bloom, H.J. Caulfield, J.J. Comer, R.S. Kennedy, J.D. Kierstead, M. Salour					
13a. TYPE OF REPORT Final		13b. TIME COVERED FROM May 87 TO May 88		14. DATE OF REPORT (Year, Month, Day) June 1989	
15. PAGE COUNT 134					
16. SUPPLEMENTARY NOTATION					
17. COSATI CODES			18. SUBJECT TERMS (Continue on reverse if necessary and identify by block number) Indium Phosphide, Infrared Device, Electro-Optic Substrates, Single Crystal, Optical Signal Processing		
FIELD	GROUP	SUB-GROUP			
17	02				
19. ABSTRACT (Continue on reverse if necessary and identify by block number)  1. Synthesis, Single Crystal Growth, Purification and Characterization of Indium Phosphide 2. Deposition of Select Silicides Under High Vacuum Conditions 3. Use of Electron Microscopy as a Tool for Identifying and Evaluating Electronic and Optical Materials 4. Use of Fiber Optics and Communication Systems (IROCS)					
20. DISTRIBUTION / AVAILABILITY OF ABSTRACT <input checked="" type="checkbox"/> UNCLASSIFIED/UNLIMITED <input type="checkbox"/> SAME AS RPT. <input type="checkbox"/> DTIC USERS			21. ABSTRACT SECURITY CLASSIFICATION Unclassified		
22a. NAME OF RESPONSIBLE INDIVIDUAL Carl A Pitha			22b. TELEPHONE (Include Area Code) (617) 377-3488		22c. OFFICE SYMBOL RADC/ESOP

## FOREWARD

This report is the Annual Scientific Report for Contract F19628-87-C-0155 covering the period 29 May 1987 through 31 May 1988. It covers the investigative effort dealing with Opto-Electronic Material and Device Investigation.

The following individuals have contributed to results reported in these reports:

Joseph A. Adamski - Parke Mathematical Laboratories (PML)  
Jerome H. Bloom - Consultant to PML  
H. John Caulfield - Consultant to PML  
Joseph Comer - Consultant to PML  
Robert Kennedy - Consultant to PML  
John Kierstead - Consultant to PML  
Michael Salour - Consultant to PML

Accession For	
NTIS GRA&I	<input checked="checked" type="checkbox"/>
DTIC TAB	<input type="checkbox"/>
Unannounced	<input type="checkbox"/>
Justification	
By _____	
Distribution/	
Availability Codes	
Dist	Avail and/or Special
A-1	

## TABLE OF CONTENTS

	<u>Page</u>
Preface	v
SECTION I:      Synthesis, Single Crystal Growth of Indium Phosphide-Single Crystal Growth and Feed Preparation of $\text{SrTiO}_3$ Super- conductors (J.A. Adamski)	1
SECTION II:     Device Processing Techniques (J.H. Bloom)	22
SECTION III:    Reducing Ambiguities Using Neural Networks with More Than Two Hidden Layers (H.J. Caulfield)	54
SECTION IV:     Materials Evaluation Techniques (J. Comer)	60
SECTION V:      Fiber Optics in Communication Systems (IROCS) (R. Kennedy)	71
SECTION VI:     Development of Efficient High Speed Nonlinear Optical Materials that Operate at Relatively Low Laser Intensities (J. Kierstead)	88
SECTION VII:    Optical Signal Processing in Nonlinear Polymers and Other Materials (M. Salour)	100

## PREFACE

This report is composed of seven sections. It provides a summary of work accomplished under this contract in several diverse areas of optical transmission, materials processing. The areas include:

I. A description is given of the experimental program on the synthesis and single crystal growth of indium phosphide. The work is directed toward developing a single step, two phase process for the synthesis and single crystal growth of the material. A detailed description of the Magnetic Liquid Encapsulated Czochralski is given together with the new electromagnetic to produce dislocation free InP crystals. Also, a description of the flame fusion furnace is given with some details in an attempt to grow superconducting materials and Strontium Titanate single crystals. A recipe is given to produce strontium titanate powder to grow these  $\text{SrTiO}_3$  crystals.

II. Device processing techniques covering the use of ultra high vacuum deposition system for evaporating a dielectric layer of silicon monoxide. This section also includes a discussion on the use of an ion beam implanter for forming special buried layers on silicon devices. The extreme usefulness of a residual gas analyzer to determine gas species within the vacuum chamber is shown.

III. Materials evaluation techniques under the general heading of electron microscopy. This includes the following methods of analysis: transmission electron microscopy, scanning electron microscopy, electron beam channeling, electron diffraction, and energy dispersive X-ray analysis.

IV. A description is given regarding connecting a two-hidden-layer neural network through an intermediate multiplicative layer showing that it can yield full or partial disambiguities of

results from a single "traditional" neural network.

V. Communication security has been achieved in fiber optic communication systems (IROCS) by ensuring that any undetected intrusion will deliver so little power to a potential intruder that no useful information can be extracted from it. Work during the past year has been concerned with determining the user performance in intrusion resistance that can be achieved using the modulation/coding method.

VI. Photorefractive and resonant nonlinear optical interactions are being studied. Resonant interactions are the most promising, but have been difficult to study in detail because of broadening mechanisms that are present in most material, for example crystal fields in solids and collisions in vapors. To eliminate the complications the nonlinear optical properties of an atomic beam will be studied.

VII. In this report the requirements of nonlinear optical materials are discussed and fundamental limits are derived. Of particular interest are a new class of materials based on nonlinear optical effects in polymers.

J. Adamski

#### SYNTHESIS OF INDIUM PHOSPHIDE

The TRICO furnace was down for several weeks during this reporting period because the automatic pressure control valve was damaged due to an explosion of an indium phosphide experiment. The motorized valve was sent back to the manufacturer and completely overhauled. The valve was returned from being repaired, the automatic pressure system was re-assembled, and tests were conducted to check the calibration of the system.

The TRICO furnace is in operation and synthesis of indium phosphide at high pressures has resumed.

Several synthesis experiments have been completed and all were successful. Synthesis of InP has been temporarily terminated, as the present effort is towards accomplishing in-situ single crystal growth. The in-situ growth of InP to be performed, using a new Magnetic Liquid Encapsulated Czochralski (MLEC) furnace (shown in Figure 1) will accomplish in one work day (8 hours) what now takes approximately 3 days (24 hours). This method will eliminate most of the impurity problems, as the crystal does not require all the handling operations needed to prepare the synthesized ingot to be used in the high pressure Czochralski furnace.

The synthesized ingot used as feed material in the high pressure Czochralski system needs to be cut into pieces to fit into a crucible. After the pieces are cut, they must be thoroughly cleaned, acid etched and rinsed with P.I. water several times. In handling these ingots during the cleaning and etching operation, there is not guarantee that all the cut pieces are free from contaminants. Conversely, using the Czochralski in-situ technique, growth is started using the raw high purity elements (In and P) to form the compound (InP). These materials are placed in the high pressure Czochralski furnace, and if successful, the product will be high purity single crystal InP. thus, synthesis is accomplished in a similar way as the synthesis in the TRICO furnace, but the high pressure Czochralski furnace



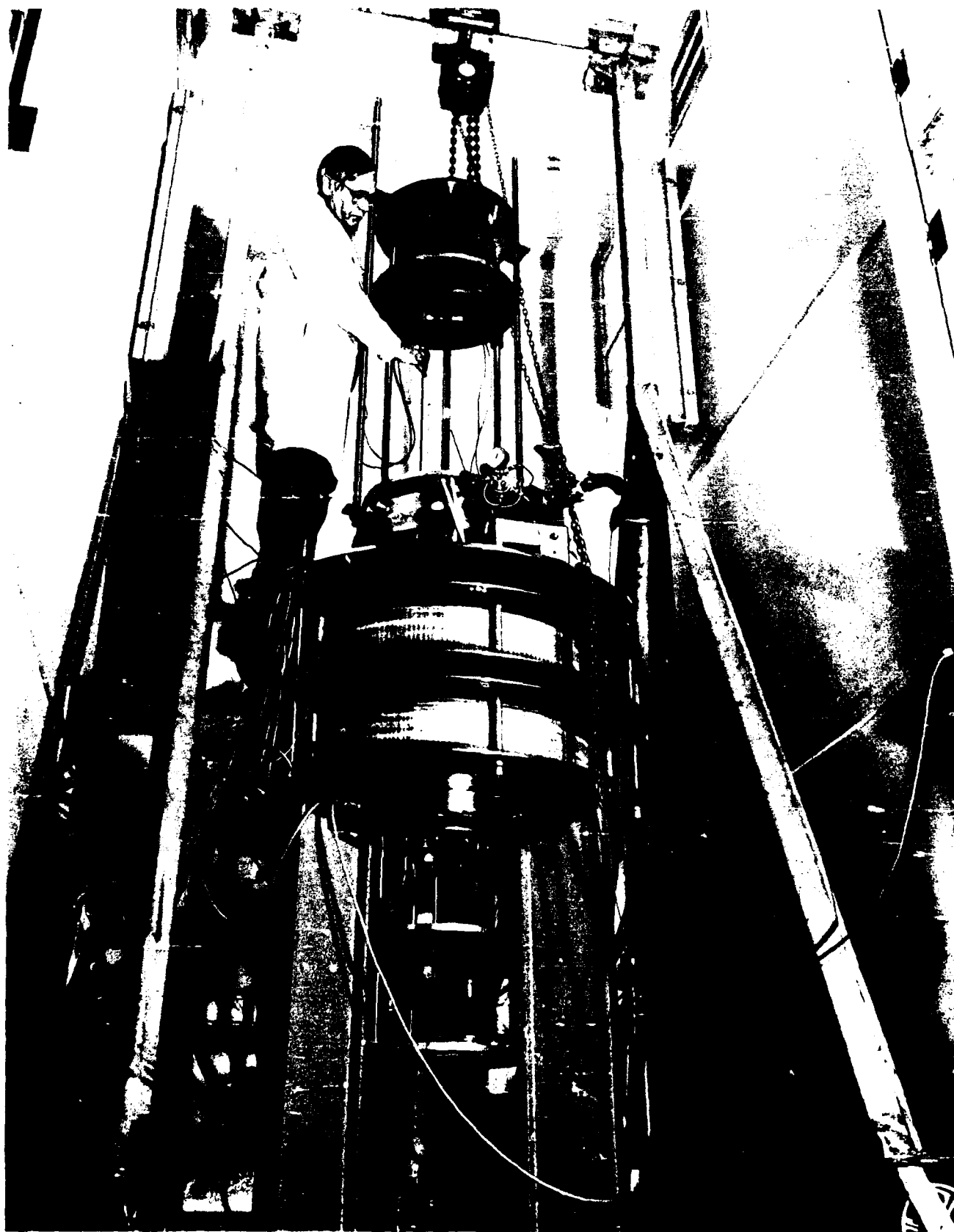


FIGURE 1

has a pulling mechanism incorporated into the system. This allows a seed crystal to be attached to a pull rod. The seed goes down into the molten InP that has just been formed through an injection process. By maintaining the proper melt temperature, meniscus forms around the seed crystal, and by rotating and pulling the seed crystal out of the melt with the pull rod, one can achieve single crystal growth in this one step procedure.

#### IN-SITU PROCESSING

In-situ processing for combining the indium and phosphorus has several advantages over conventional reactions. The indium is loaded into the MLEC furnace, heated and encapsulated with  $\text{B}_2\text{O}_3$ . Figure 2 shows the sequence used to inject phosphorus into the indium, thus producing InP. A silica injector loaded with high purity elemental phosphorus (shown in (a)) is lowered into the molten indium ( $T=1180^\circ\text{C}$ ). A self controlled reaction occurs as the P is heated and is convected into the molten indium where it reacts to InP shown in (b). After complete reaction of the elements, the injector is removed from the hot zone location and a single crystal seed is lowered into the InP melt for Czochralski growth shown in (c). At this time, the high field strength electromagnet is turned on and a single crystal of approximately 400 grams is produced. There are no intermediate steps for cleaning and etching of pre-processed InP, therefore this InP will have fewer opportunities for contamination.

Currently, 100 grams of P is being injected into 300 grams of Indium in the new RADC magnetic crystal furnace. This process can easily be scaled up to several kilograms of InP.

The first in-situ injection experiment was incomplete, because the injector was not adequately heated by the radiated heat from the crucible and susceptor. To remedy this a new hot zone was fabricated that decouples the RF induction from the axial position of the crucible. An outer susceptor sleeve that is fixed in a given axial location surrounds an inner graphite pedestal and crucible. The inner assembly can be processed up in

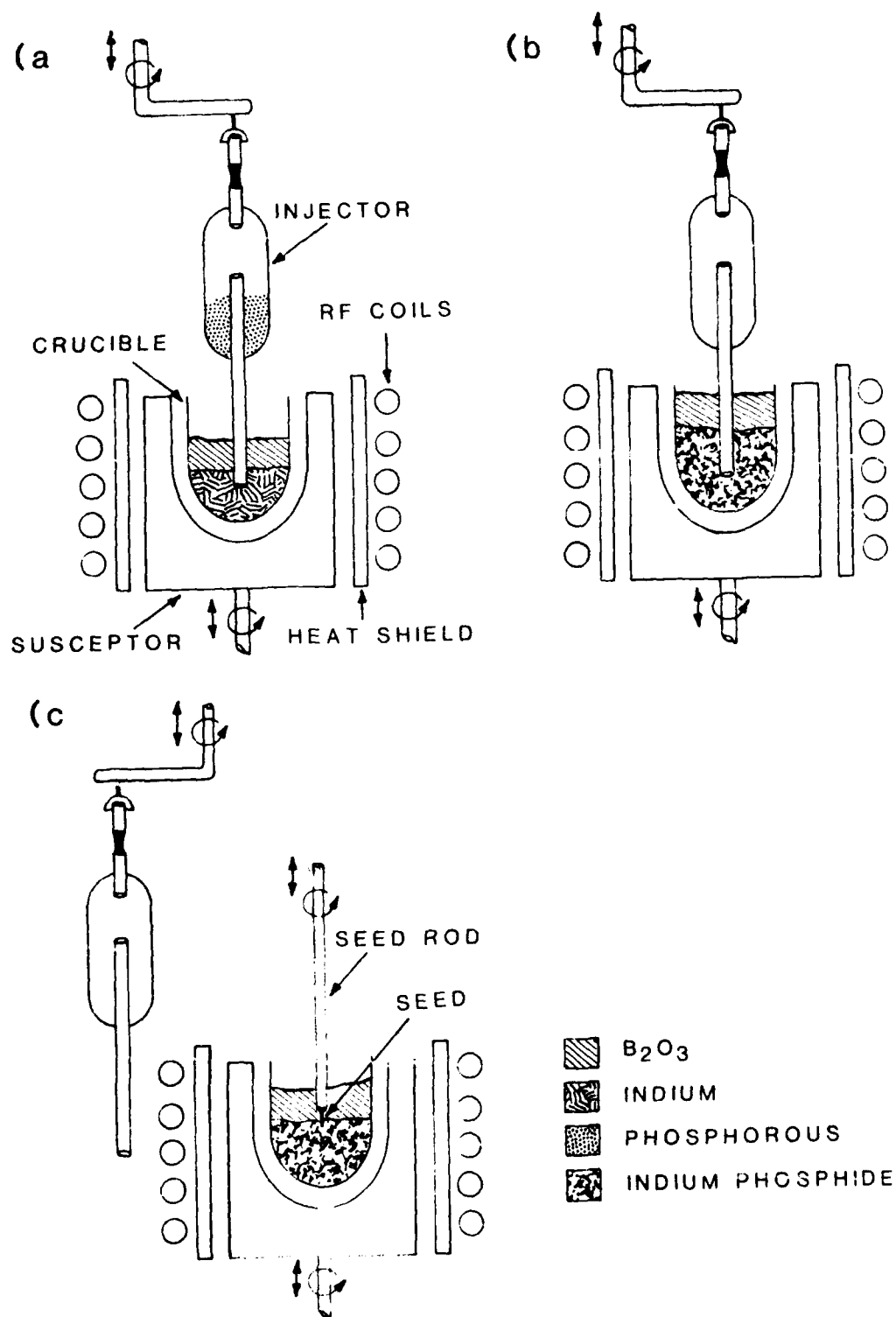


FIGURE 2

drum to adjust its position in the hot zone. This allows for independent heating of the P injector during in situ processing.

Problems were encountered in working with this new phosphorus injection system. Phosphorus was injected into the indium, but we were unable to inject the total amount of phosphorus needed to obtain stoichiometry. The second experiment was going well, and it appeared that most of the phosphorus had left the injector. It was decided to leave the injector in position a little longer to make sure that all the phosphorus vapors had gone into the molten indium. The injector was left in the hot zone too long, causing the quartz to devitrify. Because of the devitrification problem, the quartz weakened and cracked, causing the phosphorus to escape and start dissociating from the indium. By losing the phosphorus from the melt, the furnace system became coated with the vapor, the pressure lines from the nitrogen gas manifold became plugged with a by-product formed with the phosphorus vapor and oxygen. This by-product was a gummy substance and the whole furnace system and the pressure lines had to be taken apart and cleaned thoroughly. During clean-up, many small outburst of fire would occur, causing a tremendous amount of smoke.

After the clean-up was completed, the apparatus was completely checked out and a simulated experiment was conducted. Several experiments were completed using different types of insulating materials at the top of the injection to prevent heat loss. None of these materials were satisfactory (quartz, alumina and fire brick). A new insulating cap is being designed and fabricated (shown in Figure 3) to fit over the top of the quartz injector to prevent heat loss. This should allow proper heating of the phosphorus and injector during the in situ process and complete reaction can be expected. Presently, injection experiments shows that only 50% of the phosphorus is being injected into the molten indium.

For the growth of InP single crystals, the high pressure liquid encapsulated Czochralski (LEC) method is employed. As stated by Moricke et al., this method has the following

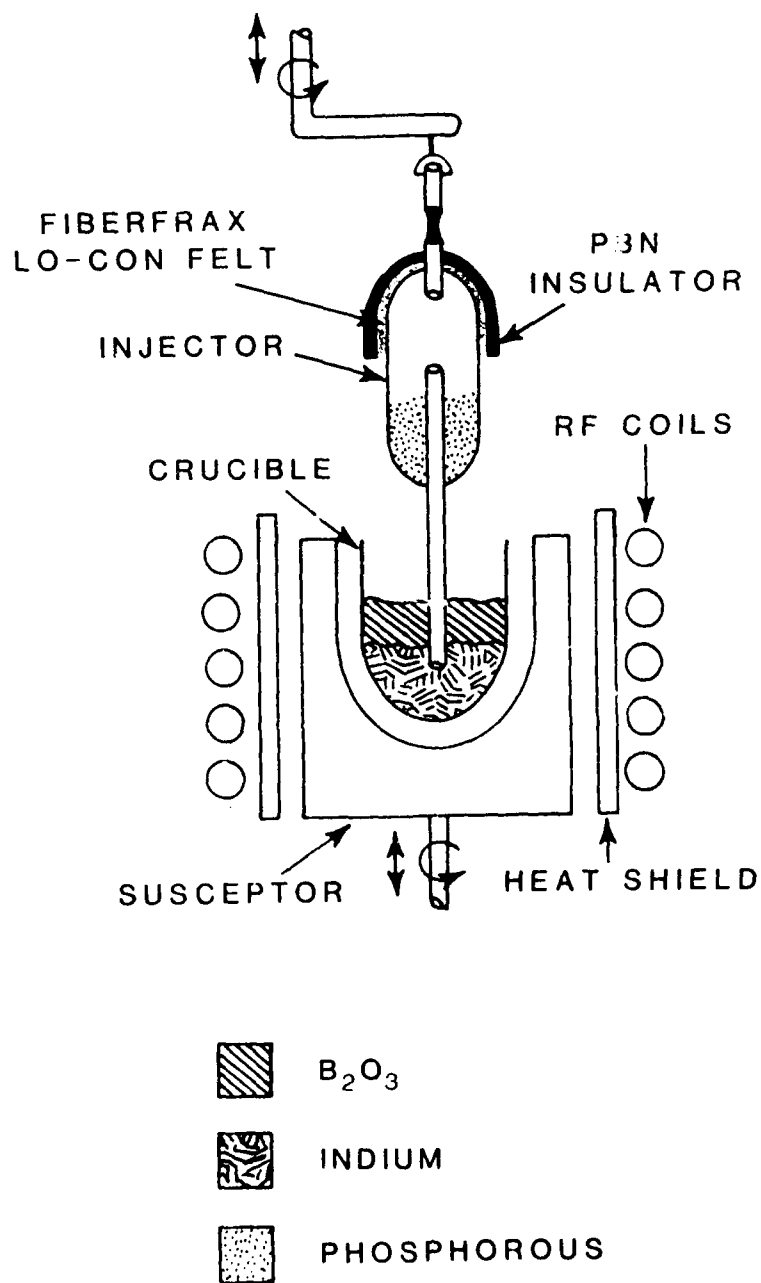


FIGURE 3

advantages: the growth rate is as high as 1-2mm/hr., crystallization is easy along the  $\langle 100 \rangle$  direction, and a large disk-shaped substrate can be obtained.

In the crystal growth of a III-V compound semiconductor it is important to suppress the dissociation of group V elements, which have high dissociation pressures near the melting point. This dissociation pressure of P near the melting point of the InP crystal is 25-27.5 atmospheres, which is much higher than the value of As of GaAs crystals (0.9 atm.). To suppress the dissociation of P, InP crystals are pulled through a liquid encapsulated ( $B_2O_3$ ) layer over the InP melt surface under the pressure of an inert gas.

A major problem in the growth of single-crystal InP is the generation of twinning, which occurs more frequently than in other III-V compounds such as GaAs and GaP. The cause of twinning is not yet clear. However, several experimental methods to prevent it have been examined, and it has been found that twinning can be reduced by one-half to one-third if the following guidelines are followed.

1. Use stoichiometric InP as the source.
2. Suppress temperature fluctuations at the crystal-melt interface.
3. Use  $B_2O_3$  with low water content.
4. Keep the  $B_2O_3$  in a clear, transparent condition.
5. Realize a melt-crystal interface free of impurities such as oxides.
6. Make the melt-crystal interface convex with the melt side concave. Control this shape by changing the pulling rate and the rotation rate.
7. Avoid decomposition of phosphorous from the surface of the pulled crystal by keeping the surface temperature of the  $B_2O_3$  layer down at 600-700°C.

Indium phosphide is a strategic opto-electronic material. The crystalline quality of the MLEC ingots is directly related to the purity of the starting materials and the subsequent handling

of them throughout the processing sequence. Figures 4 and 5 are InP crystals recently grown in the new MLEC apparatus. Figure 5 was the best crystal grown to date. It was grown at full field of the magnet (4.0 kilo-Gauss) and was better than 90% single. Only marginal twinning was observed. The growth rate of the two crystals was approximately 12mm/hr., the diameter was 50mm and the lengths were 8cm and 5cm respectively.

#### MAGNETIC CZOCHRALSKI CRYSTAL GROWTH

The new magnetic crystal growth system shown in Figure 1 is now completely assembled and in operation. Several tests were conducted using germanium metal as feed material to grow single crystals. Germanium was used in the initial testing phase of the system, as it is much easier to grow single crystal of this material than indium phosphide. Three experiments were completed using germanium. One experiment was completed where the germanium was doped with 1 percent gallium. Figure 6 shows three of the germanium crystals grown. The crystal on the left was grown with very poor control of the 50kW-450kHz RF generator.

Time was spent to design a better control system for the RF generator to the heating coil inside the MLEC growth chamber. An Omega temperature controller was slightly modified and an RF pick-up coil was used. The crystals in Figure 6 that are shown in the center and to the right were grown using this new temperature controller. A fourth crystal, (not shown), doped with gallium, was grown in an automatic control mode and no problems were encountered during the growth time, which was approximately six hours. All four experiments were completed using the electro-magnet. The magnetic field used was approximately 1.2 kilo-Gauss.

One experiment using an InP single crystal seed was completed in an attempt to grow a single crystal of indium phosphide. The growth chamber was pressurized to 500 psig and this pressure was maintained throughout the growth period. The indium phosphide charge weighed 360 grams and boron oxide was used as the encapsulant to prevent the phosphorus from dis-



FIGURE 4



FIGURE 5





FIGURE 6

associating from the indium. The electro-magnet was turned on after the crystal was growing for approximately two hours. During the next two hours, the magnet was turned on and a magnetic field of 1 kilo-Gauss was established. Figure 7 shows the crystal grown in the MLEC apparatus, which is the first InP crystal grown in the new furnace.

Magnetic stabilization will permit controlled growth in lower thermal gradients, which is expected to translate directly into a low dislocation product. Furthermore, the magnetic stabilization will reduce the magnitude of impurity striations and increase the yield of twin free crystals.

The InP experiments include encapsulation with Boric Oxide. This molten glass is adversely affected by water vapor. Therefore a pre-bake cycle to clear the graphite susceptor of H<sub>2</sub>O has become a part of the growth routine. The silica crucibles have been optimized for InP charges of 500 to 1000 grams. The first InP growth run was conducted with 360 grams of presynthesized InP from the high pressure growth runs (TRICO furnace).

The goal of this project is to establish the capability to synthesize and grow large diameter InP with 4.3 kilo-Gauss magnetic stabilization. The magnetic field will be modulated to control the diameter of the growing crystals. Ultimately, an IBM AT computer will control virtually every aspect of the apparatus (including four motors; 50 kW, RF power supply; 50kW DC Magnet Power Supply).

#### ELECTROMAGNET

A number of experiments were planned for the growth of InP during this reporting period, but a problem developed with the cooling system to the electromagnet. It wasn't until the magnet could safely operate at full power that the overheating of the copper coils developed. The manufacturer was called in to inspect the plumbing and water flow drawings. It was discovered that the designer made an error in the design of the input and output with ports to the separate windings. The copper windings through the center of the magnet had no water flowing through



MLEC Grown InP

FIGURE 7

them. The water flow pattern was corrected and the magnet can now be used at full power (4.3 kilo-Gauss). The specifications for cooling this magnet is to have a constant flow of water at a rate of 10 gallons per minute.

### SUPERCONDUCTORS

Superconductivity research within the past few months has exploded because of new theories and "warmer" materials that are based on oxides rather than metals. Attempts to raise the temperature at which materials become superconducting have so far been promising but inconclusive. RADC/ESM has embarked on a program recently using yttrium-barium-copper oxide. Several pellets have been produced using various techniques, and when placed in a dish containing liquid nitrogen, small magnets levitate over the cooled yttrium-barium-copper oxide pellets. This testing procedure has become a basic test for true conductivity. The expulsion of magnetic flux from superconductors is known as the Meissner effect.

In discussing superconductor materials with the RADC scientists, it was suggested that a flame fusion apparatus, previously used to grow rubies and sapphires, be used in an attempt to produce some of these new ceramic oxide materials. Everyone involved in the discussion agreed that this method of crystal growth should be incorporated in the research program.

Figure 8 shows the flame fusion apparatus, invented by August Verneuil<sup>2</sup> over 75 years ago. It has been used for the growth of sapphire, ruby, spinel, rutile, strontium titanate, and other refractory crystals. The process consists of feeding finely powdered material into a high-temperature flame produced by oxygen and hydrogen. The flame from the torch is directed downward at a pedestal or seed crystal and growth is initiated. The powder particles are melted in the flame produced by the torch and fall upon the seed which is placed in the lower part of the flame so that only it's surface is molten. As the melt is enlarged by powder dropping on the seed, the pedestal which supports the seed is withdrawn slowly so that the position of the

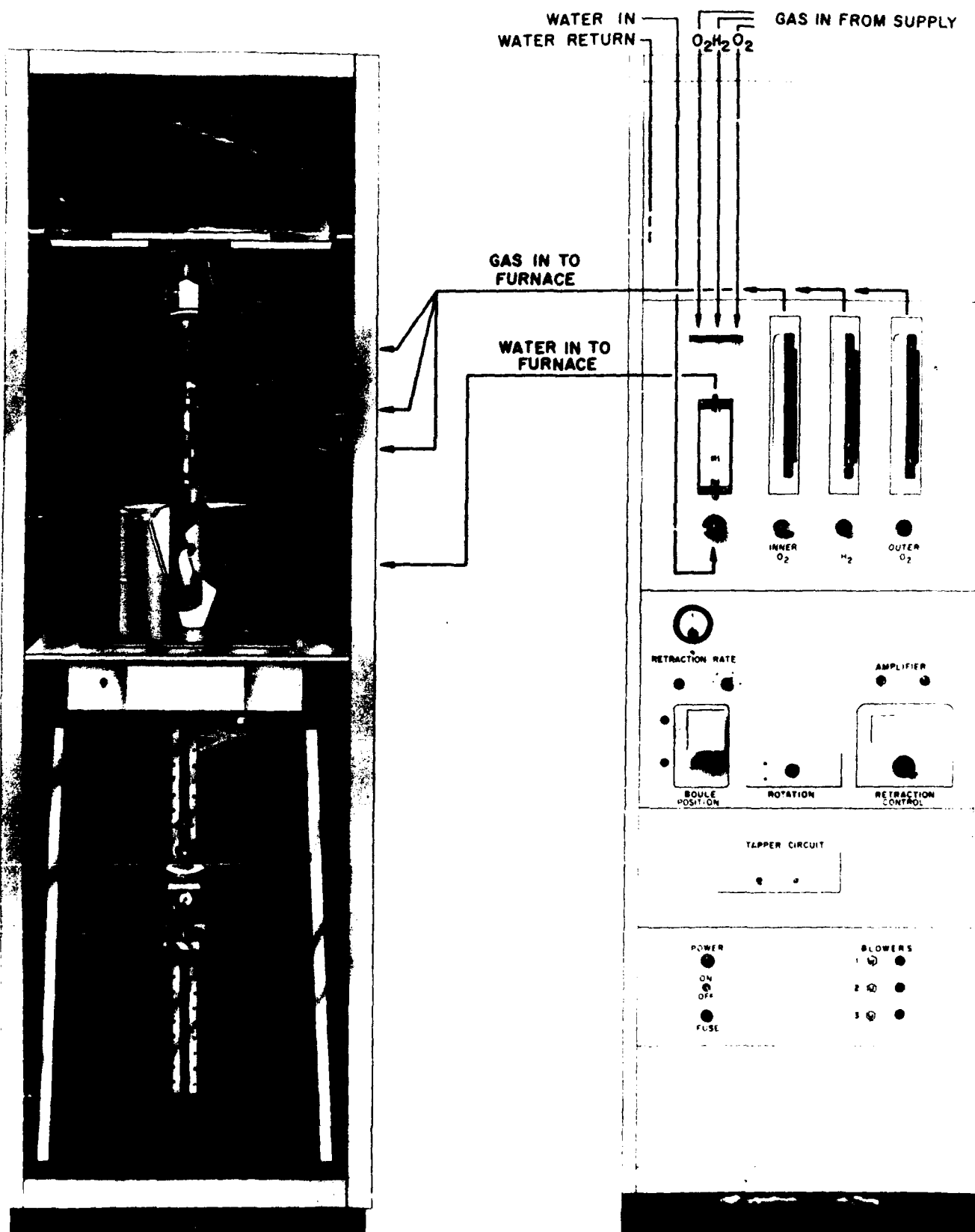


FIGURE 8

liquid-crystal interface is maintained at a constant level. This method allows refractory crystals to be grown at temperatures for which crucibles are either non-existent or unsatisfactory. This technique is used to grow single crystal materials whose melting temperatures do not exceed 2400°C.

A device has been invented<sup>11</sup> for diverting the flow of a carrier gas (oxygen) from the normal flow pattern of a conventional Verneuil apparatus, which was a batch process and closed system. Replenishment of the feed container can be accomplished thus allowing growth of unusually long crystals of varying compositions.<sup>12</sup>

Several attempts (6) were made to grow the superconductor material ( $\text{YBa}_2\text{Cu}_3\text{O}_{7-x}$ ) using the flame fusion apparatus. Problems were encountered in trying to establish the gas flow rates (oxygen-hydrogen-oxygen) to produce the proper flame temperature needed to melt this material. In the beginning, the temperature was too hot and all the barium and copper oxide volatilized. Upon examination and characterization, it was found that an yttrium oxide crystal was grown. There was no trace of barium or copper in the crystal.

The gas flow rates were changed to produce a much cooler flame and several samples of the desired superconductor material were grown. Although these crystals were not satisfactory for testing using the Messnier technique, they were of the proper composition. New powders that have better flow characteristics and small particle size are being produced and this should make the growth of these materials more desirable.

#### STRONTIUM TITANATE

An interest has been shown in the laboratory to grow single crystals of strontium titanate. It has been found that the new superconducting ceramic material ( $\text{YBa}_2\text{Cu}_3\text{O}_{7-x}$ ) is of the perovskite family as is strontium titanate. Being that the crystal lattice of the  $\text{YBa}_2\text{Cu}_3\text{O}_{7-x}$  is the same as strontium titanate, this latter crystal could be used as a substrate to deposit this new material onto, from which devices could be fabricated.

Several experiments were conducted in an attempt to grow strontium titanate using powder purchased from A.D. MacKay several years ago. This feed powder has not produced a single crystal of good quality and does not have good flowing characteristics. An attempt to prepare strontium titanate feed powder in the laboratory will be made from a receipt found in Technical Report 178.<sup>2</sup> Experiments to grow these crystals will continue, as there is no known source at this time where these crystals can be purchased commercially. If the yttrium-barium-copper superconducting material could be successfully deposited onto a strontium titanate substrate, it could be a tremendous breakthrough in the electronic device industry.

#### PREPARATION OF $\text{SrTiO}_3$ FEED POWDER

The apparatus used to prepare the  $\text{SrTiO}_3$  feed powder to be used in the flame-fusion apparatus is shown in Figures 9 and 10. The powder was prepared as follows:

177 g. of oxalic acid ( $\text{C}_2\text{O}_4\text{H}_2 \cdot 2\text{H}_2\text{O}$ ) was put into the constant temperature (jacket) beaker and 320 ml of  $\text{H}_2\text{O}$  was added. This was stirred and went into solution at the higher temperature.

40 ml of  $\text{TiCl}_4$  was added slowly to 121 ml of  $\text{H}_2\text{O}$  into a 250 ml beaker. The beaker was in an ice bath. The 40 ml of  $\text{TiCl}_4$  was contained in a 50 ml graduated cylinder and this was added slowly to the 121 ml of  $\text{H}_2\text{O}$ .

152 g of  $\text{SrCl}_2 \cdot 6\text{H}_2\text{O}$  was placed in a 1 liter beaker. To the  $\text{SrCl}_2 \cdot 6\text{H}_2\text{O}$  was added 590 ml of distilled water. To the oxalic acid solution at  $70^\circ\text{C}$ , the solution containing the  $\text{TiCl}_4$  was added. The solution was slightly yellowish. A certain amount of time was passed so that the total solution was at  $70^\circ\text{C}$ . To this solution of the oxalic acid and  $\text{TiCl}_4$ , the 590 ml containing the  $\text{SrCl}_2 \cdot 6\text{H}_2\text{O}$  was added. A white precipitate came out of solution. This was stirred for approximately 2.5 hours at  $70^\circ\text{C}$ .

The precipitate and solution was filtered by suction as shown in Figure 10.

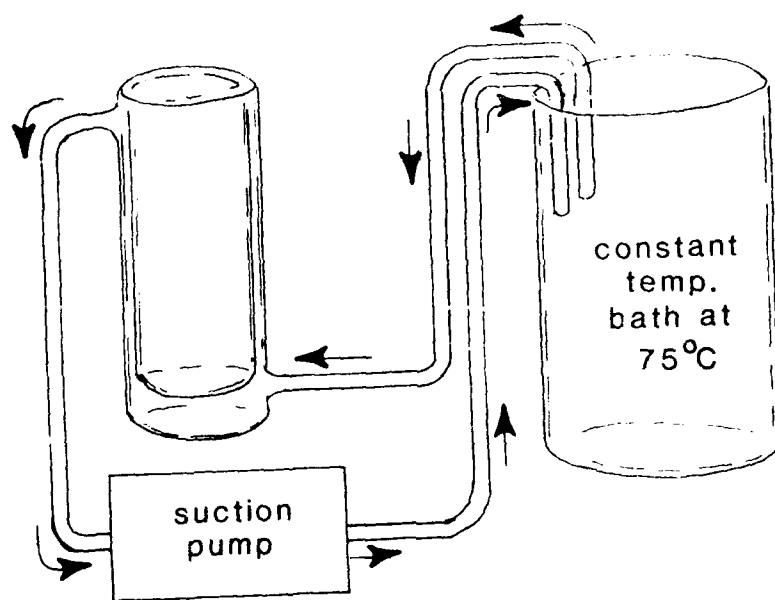


FIGURE 9

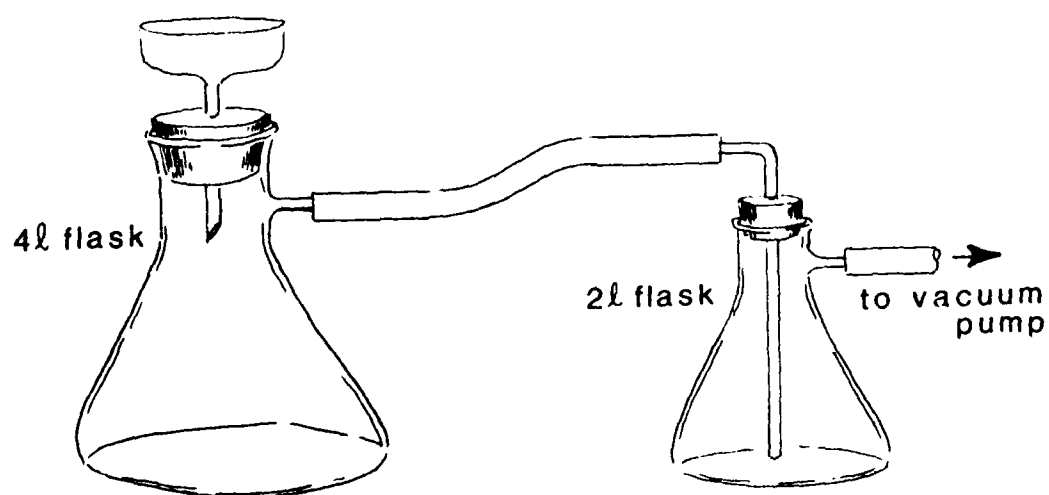


FIGURE 10



The  $\text{SrTiO}_3$  was washed with approximately 6 liters of distilled water. The precipitate was dried overnight by sucking air through the filter containing the  $\text{SrTiO}_3$ .

White finely divided  $\text{SrTiO}_3$  was transferred to four zirconic crucibles. The crucibles were put into a warm oven and allowed to sit at this temperature for 1 hour. After this time, the temperature of the oven was set at  $1000^\circ\text{C}$  and approximately 6 hours later, the oven was turned off. The  $\text{SrTiO}_3$  powder cooled to room temperature and was now ready to be used to grow single crystals of  $\text{SrTiO}_3$ .

Ten experiments were completed in an attempt to grow single crystals of  $\text{SrTiO}_3$ . Several crystals grown produced large areas where substrates will be cut so that thin films of ceramic superconductor materials can be deposited on the  $\text{SrTiO}_3$  substrates. Figure 11 is a schematic diagram of the oxy-hydrogen torch used to grow the  $\text{SrTiO}_3$  single crystals. The flame-fusion apparatus used in the present study is that of J.A. Adamski, and a paper published by J.G. Bednorz et al<sup>11</sup> was studied to get a better understanding of the growth conditions needed for reproducible production of  $\text{SrTiO}_3$  crystals of optical quality.

Strontium titanate substrates have been shown to be an attractive substrate for the deposition of thin films of the current superconductors. The program currently underway is to investigate and develop the flame-fusion technique to produce substrates of strontium titanate. Emphasis has been placed on the two following aspects of the Figure 11 preparation: 1. The method for preparation of the feed powder as described above, and 2. Determination of the flow rates of hydrogen and oxygen in the flame fusion apparatus. The results show that if the precipitation of  $\text{SrTiO}_3$  is undertaken rapidly and the dried powder is aged, a greater proportion of the particle size is between 0.074 and 0.044 mm. This particle size has been shown to be necessary for the preparation of single crystals of strontium titanate. Crystals have been grown with an oxidizing flame ( $\text{H}_2/\text{O}_2=1$ ). Slices of the boule show that single crystal growth of  $\text{SrTiO}_3$  has been attained.

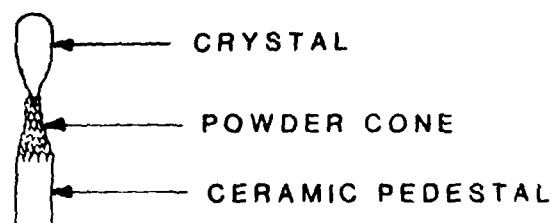
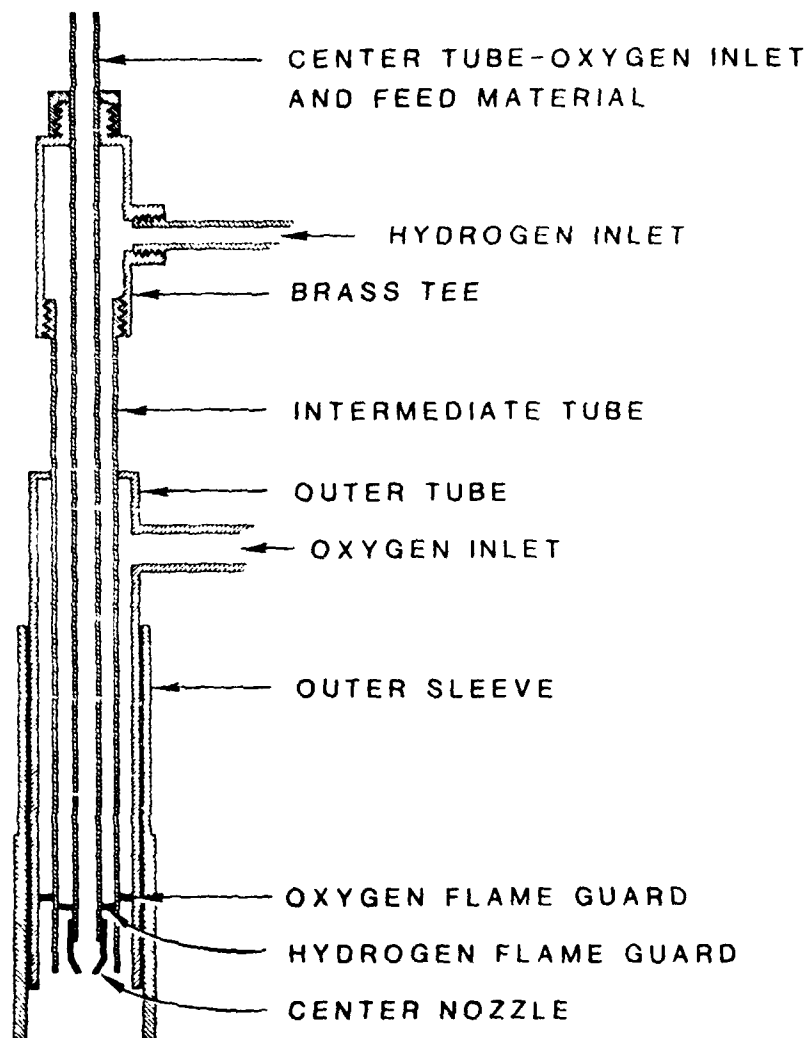


FIGURE 11

Work is continuing to determine the optimum parameter for the growth of single crystals of  $\text{SrTiO}_3$  by the flame-fusion technique. Also, the MLEC system is back in operation and several experiments have been designed and will be used during the next reporting period.

#### SUBSTRATE PREPARATION FOR HIGH $T_c$ SUPERCONDUCTING THIN FILMS

Superconductors with transition temperatures above that of liquid nitrogen have received an unprecedented amount of investigation since their discovery. These superconductive materials have been predicted to revolutionize transportation, electrical transmission, magnetic instrumentation, and microcircuitry (microelectronics and hybrid optoelectronics). The immediate application for these superconductors will be realized in the area of conventional semiconductor electronics.

The application of superconductors in electronics necessitates the development of techniques to prepare thin films of the superconductive materials. Various approaches for the preparation of the high  $T_c$  (critical temperature) superconducting films are currently underway, e.g., e-beam evaporation, single target magnetron sputtering, magnetron sputtering from three metal targets, laser deposition and molecular beam deposition. Thin film deposition required substrates that are compatible with the superconductor being deposited, viz. 1) same crystal structure with matched lattice constants, 2) similar thermal expansion, and 3) minimum interface reactions. Strontium titanate has been shown by various investigators to exhibit the most promise as substrates for these superconductive thin films.

A program has been initiated to develop the flame-fusion technique for the growth of single crystals of strontium titanate. The flame-fusion apparatus used in the present study is that of J.H. Adam et al. The preparation of the strontium titanate feed powder is critical. The grain size must fall between 0.05 and 0.1  $\mu\text{m}$ . The  $\text{SrTiO}_3$  feed powder is currently being prepared by the method of Linz et al. A bug but better  $\text{SrTiO}_3$  feed powder can be prepared by the above method and the size

fraction below 200 mesh was used to grow a b.c.10 crystal. The crystal obtained weighed 10.4g with dimensions of 2cm long and 1cm wide. The crystal was shown by x-ray diffraction studies to be polycrystalline. The crystal is currently being sliced for future characterization.

Work is continuing to determine the optimum parameters for the growth of single crystals of b.c.10 by the flame fusion technique.

#### REFERENCES

1. Horioaka, M., Iada, K., Akai, C. (1977) *Proc. Dev. Mater. Sci.* 12:75-100.
2. Verneuil, A., (1902) *Comp. Rend.* 134:791-794.
3. Adamski, J.A. (1969) *Rev. of Scientific Inst.* Vol. 40, 12:1634-1635.
4. Adamski, J.A. et. al. (1971) U.S. Patent 3,607,111.
5. Adamski, J.A., Powell, R.C., and Sampson, J.L. (1968) *J. Cryst. Growth*, 3, 4:246-249.
6. von Hippel, A., and co-workers (1963) Technical Report 170, Laboratory of Insulation Research, MIT (AFOSR 63-92) 32-35.
7. Adamski, J.A., (1965) *J. Appl. Phys.* 36, 1784.
8. Bednorz, J.G. and Scheel, H.J. (1977) *J. Crystal Growth* 41, 5-12.

J. Bloom

This annual report is divided into two sections as follows:

Section 1 discusses the procedure for acquiring a guideline for a "normal" reference for residual gas analysis.

Section 2 covers problems with system #2 and gives a discussion on a comparison of iridium silicide and platinum silicide photodiodes.

### SECTION 1

This section discusses the procedure for acquiring a guideline for a "normal" reference for residual gas analysis.

The instrumentation used is a quadrupole mass analyzer. The instruments display spectra to mass 100. In our normal operation we check gasses to mass 50, as the systems, when processed and in normal use, have no organic residue that are detectable. When we receive the gas analyser head we always bake them with the heater to eliminate the residual organic cleaning agents which are left on the head assembly.

In the discussions that follow, reference will be made to three ultra-high vacuum systems. System 1 is a Varian system mainly used at this time to fabricate iridium silicide. System 2 is a G.E. system that has been modified to have a load lock. System 3 is also a G.E. system but without the modification of a load lock.

Figures 1-4 are spectra of the residual gas of system 1. System 1 has a large bell jar and is pumped by a Varian diode sputter ion pump. The sensor head is the old design which gives an extraneous peak at mass 16. Figure 1 is a bar graph of mass 1 to 50. A large reading on a specific mass can cause a spillover to an adjacent mass number. The vacuum reading is not accurate so we always use the vacuum read by an ion gauge. The vacuum in the chamber is  $1.0 \times 10^{-10}$  Torr as read by a Varian ion gauge control using a needle tube inserted in the vacuum chamber. Figure 2 is an analog spectra of masses up to mass 20.

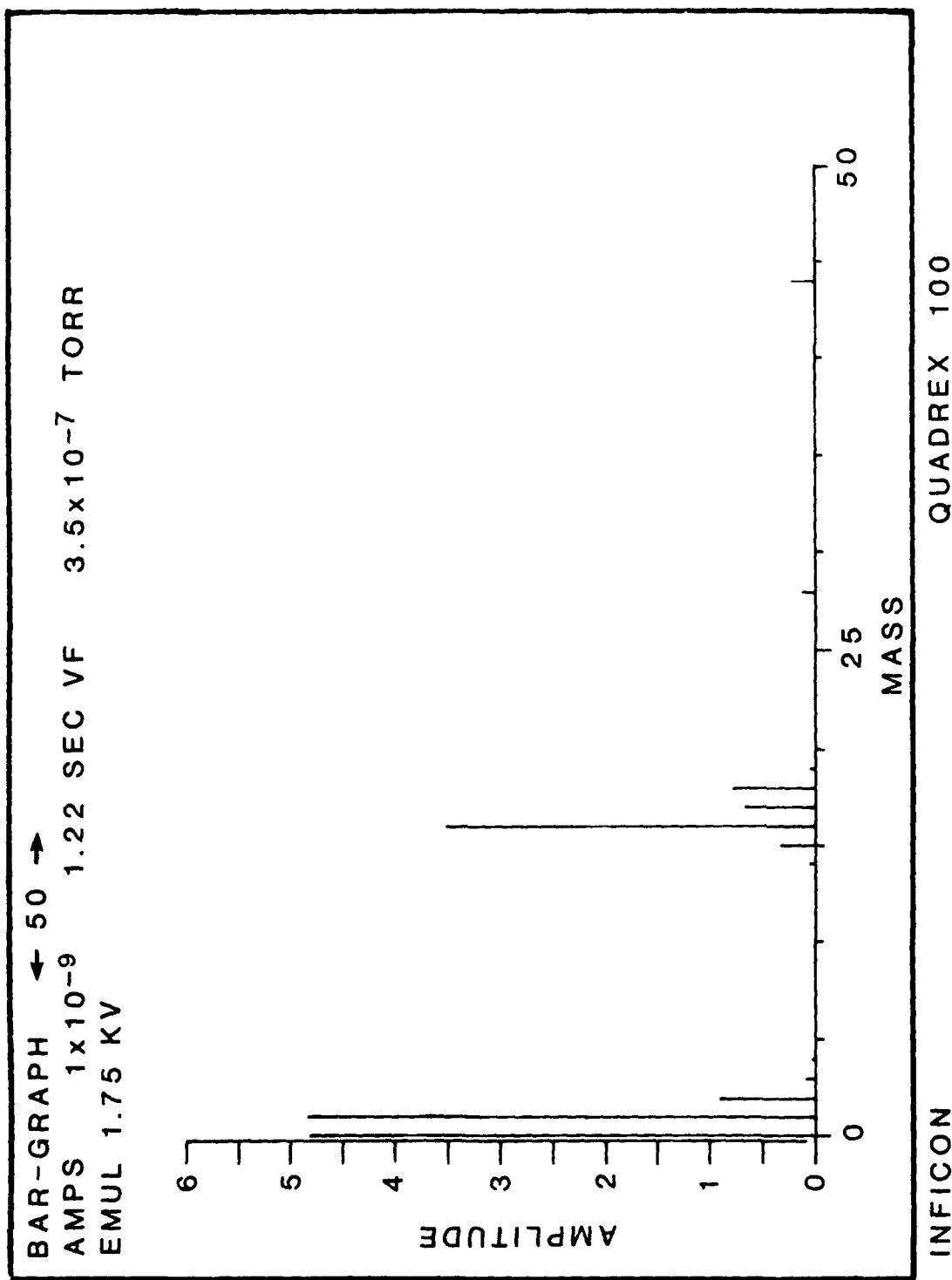


FIGURE 1

QUADREX 100

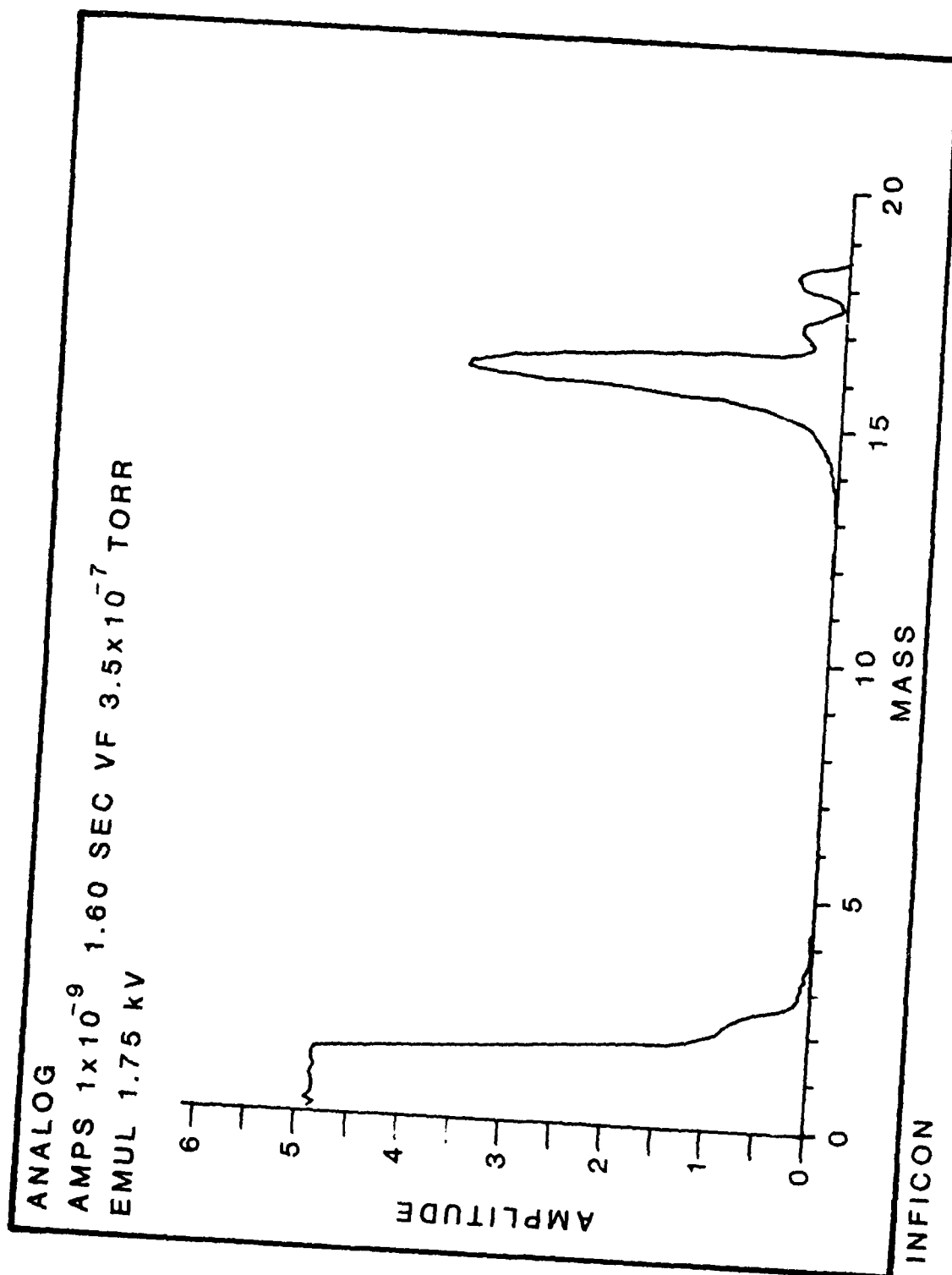


FIGURE 2

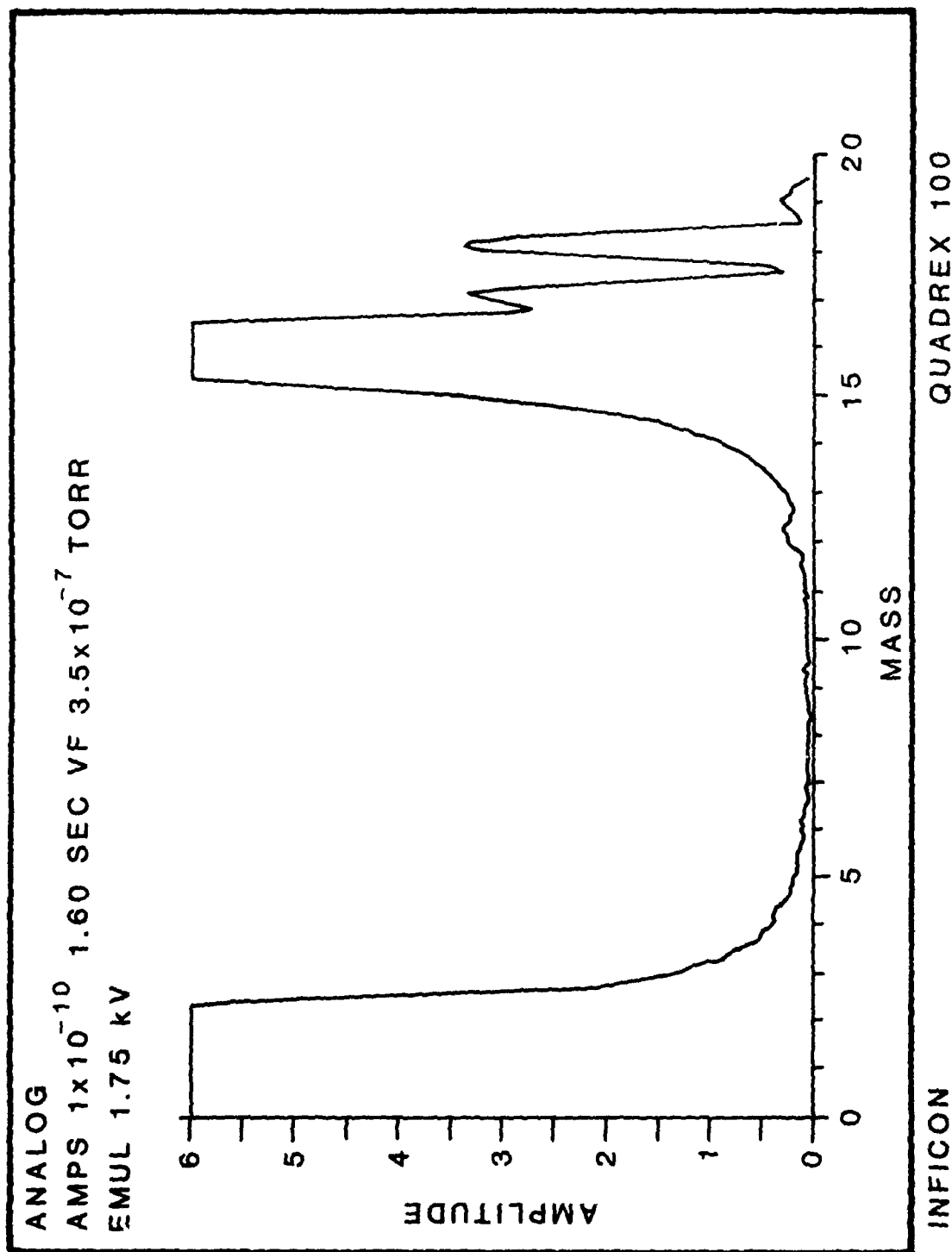


FIGURE 3



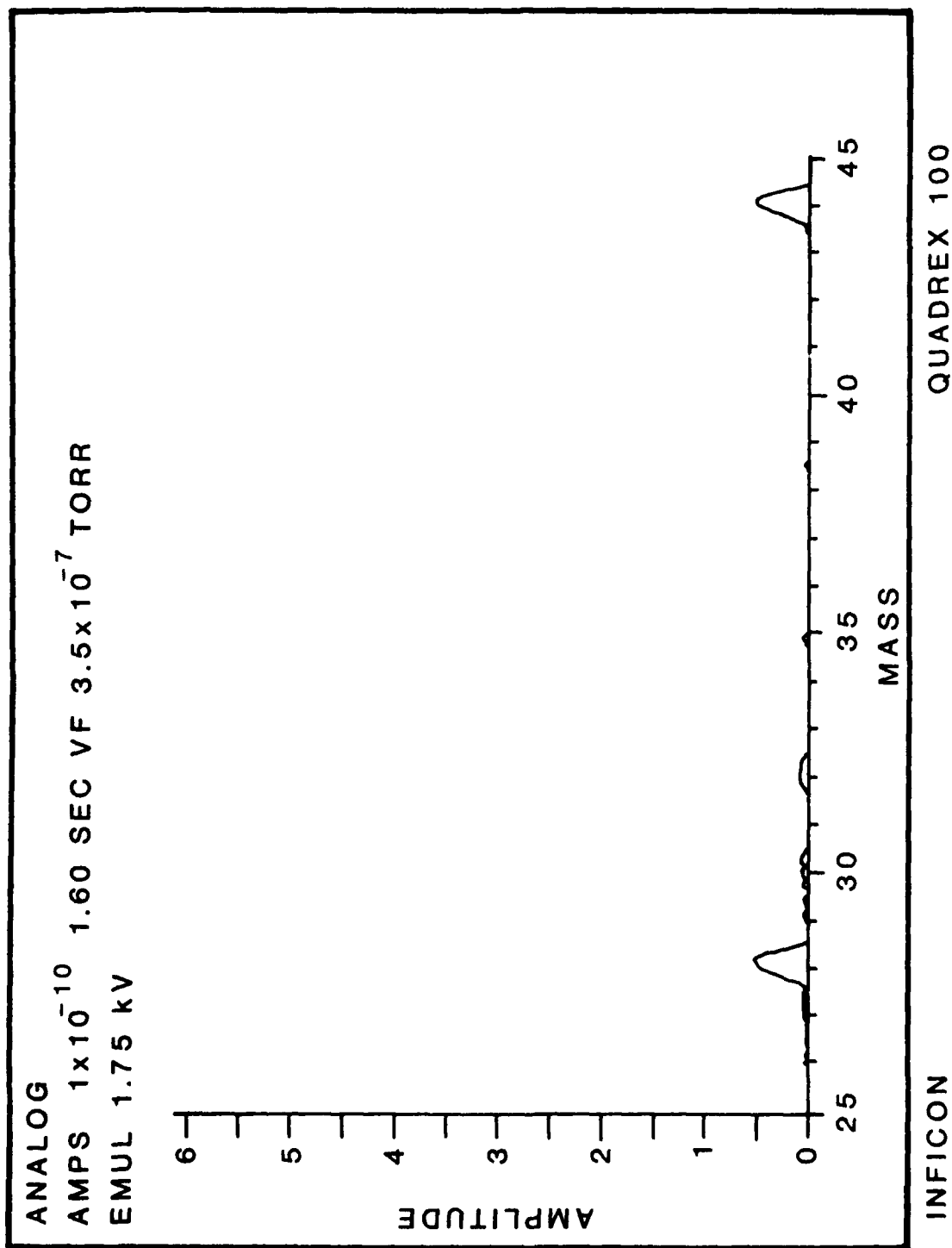


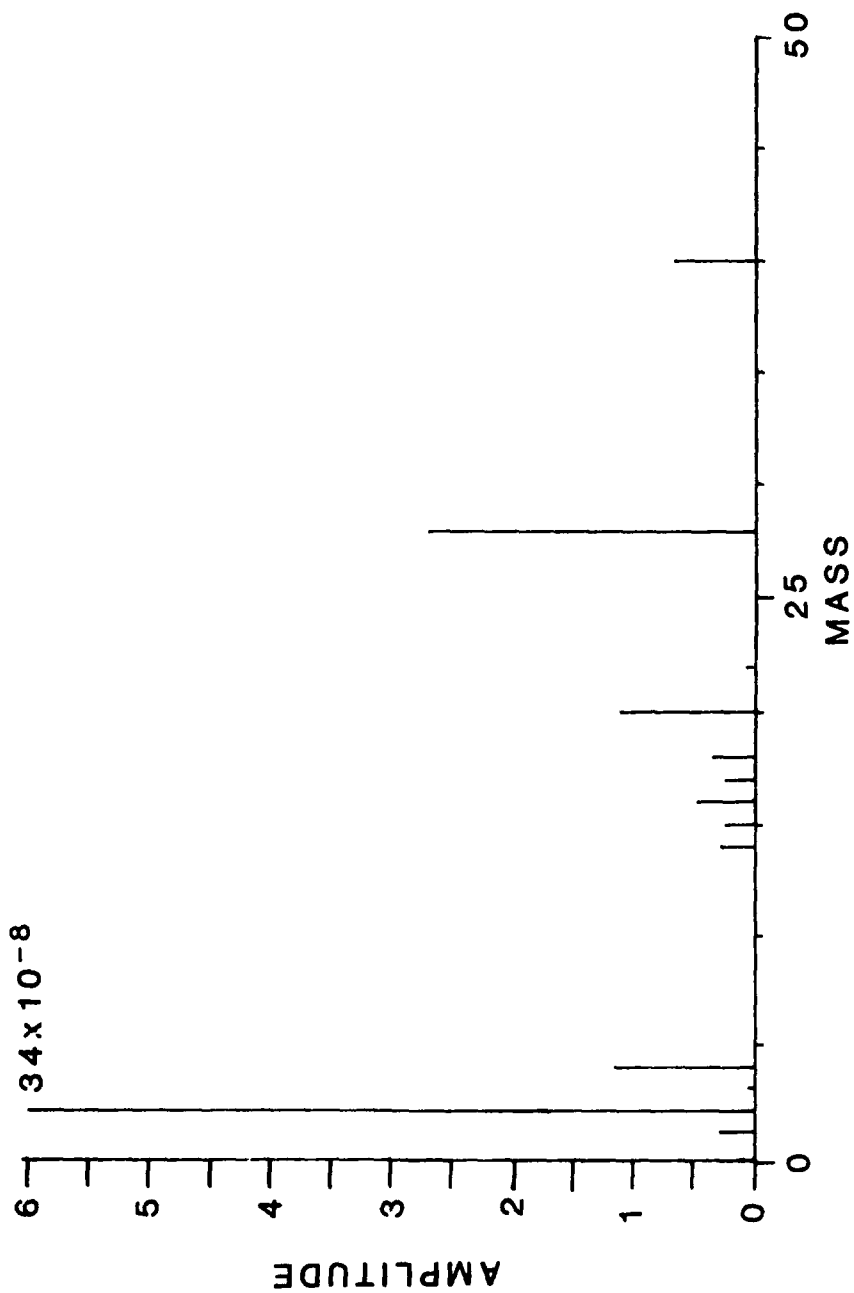
FIGURE 4

Examination of this Figure shows that spill-over from zero mass to mass 2 has occurred. The amplitude of the bar graph at mass 2 is close to the half peak seen at mass 2 on the analog picture. The peak at mass 16 is primarily made up of background due to contamination of the head sensor. (A new design sensor has eliminated this problem.) Figure 3 is the result of increasing the sensitivity by a factor of ten. Examination of Figures 3 and 4 shows a small amount of mass 12 due to carbon ( $C$ ); mass 16 if present is due to methane ( $CH_4$ ); mass 17 due to a fragment of water ( $OH$ ); mass 18 due to water vapor ( $H_2O$ ); mass 19, which seems to be an anomaly of the head sensor, as fluorine ( $F$ ) which should not be present; and mass 28 is due to nitrogen ( $N_2$ ) or carbon monoxide ( $CO$ ). Examination of daughter peaks, caused by electron bombardment of the original material, can tell if  $CO$  or  $N_2$  is present. Masses 29 and 30 are possible isotopes of nitrogen. Mass 44 is carbon dioxide ( $CO_2$ ).

Analysis of the gas ambient of system 2 can be done by examining Figures 5 to 11. Figure 4 is a bar graph of the spectra. Figures 6, 7 and 8 are analog spectra of the same gas ambient. Mass 1 is spill-over from mass 2 which is the main constituent and would be at an amplitude of 34 on this scale; it is hydrogen ( $H_2$ ). Mass 3 is spill-over; mass 4 is helium ( $He$ ); mass 14 is double ionized nitrogen ( $N_2^+$ ); masses 15 ( $CH_4$ ) and 16 are due to methane ( $CH_4$ ) which is sometimes made in ion sputter pumps; mass 17 is due to water vapor ( $OH$ ) as is mass 18 ( $H_2O$ ). Figures 7 and 9, which have three times the sensitivity of Figures 5 and 6, show a mass 20 which could be due to hydrogen fluoride ( $HF$ ); mass 22 is unknown; mass 28, which is at an amplitude of 27 on this scale, is due to nitrogen ( $N_2$ ); mass 29 and 30 can be due to isotopes of nitrogen; mass 23 is oxygen ( $O_2$ ); and mass 40 is due to argon ( $Ar$ ).

Figure 9 is a bar graph of the gas ambient at a later date. Examination of the analog spectra shows a typical spectra of an air leak. There is a large peak at mass 28 due to nitrogen and at mass 14 doubly-ionized nitrogen, high mass 4 due to helium and high mass 40 from argon. Mass 32 due to oxygen ( $O_2$ ) is also

BAR-GRAPH ← 50 →  
 AMPS  $1 \times 10^{-8}$  7.34 SEC VS  $1.5 \times 10^{-7}$  TORR  
 EMUL 1.75 KV



INFICON

QUADREX 100

FIGURE 5

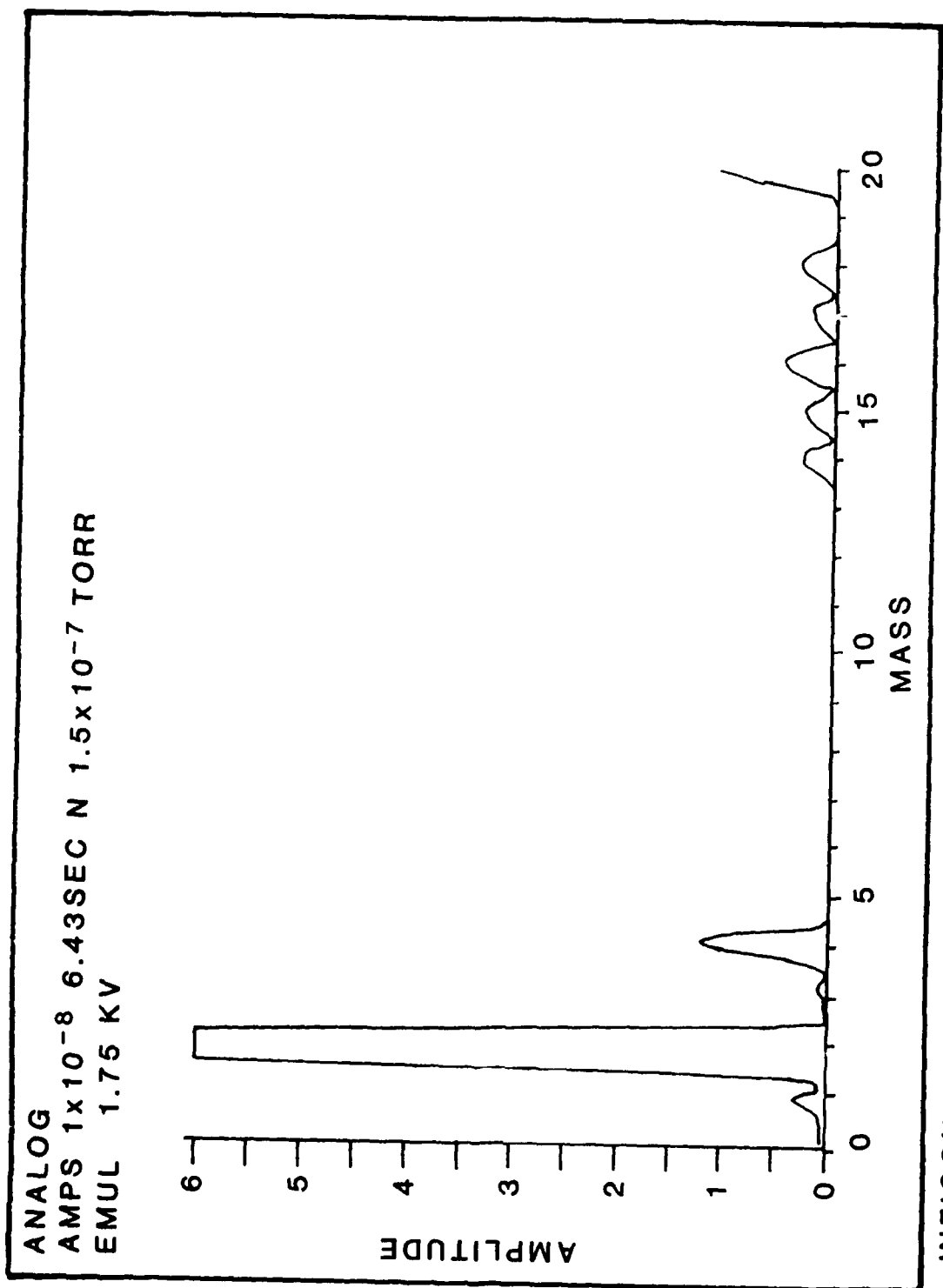
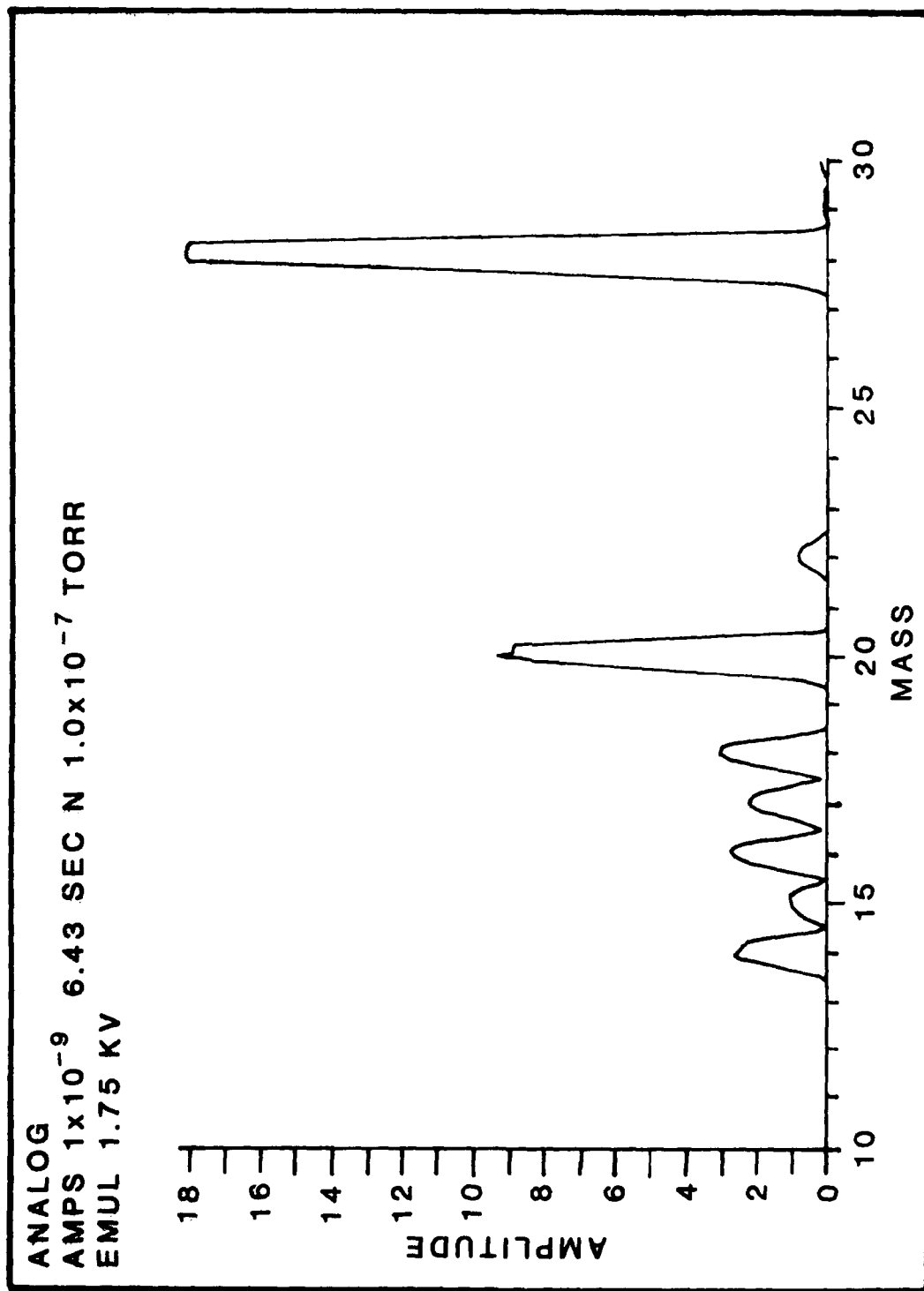


FIGURE 6 QUADREX 100



INFICON

QUADREX 100

FIGURE 7

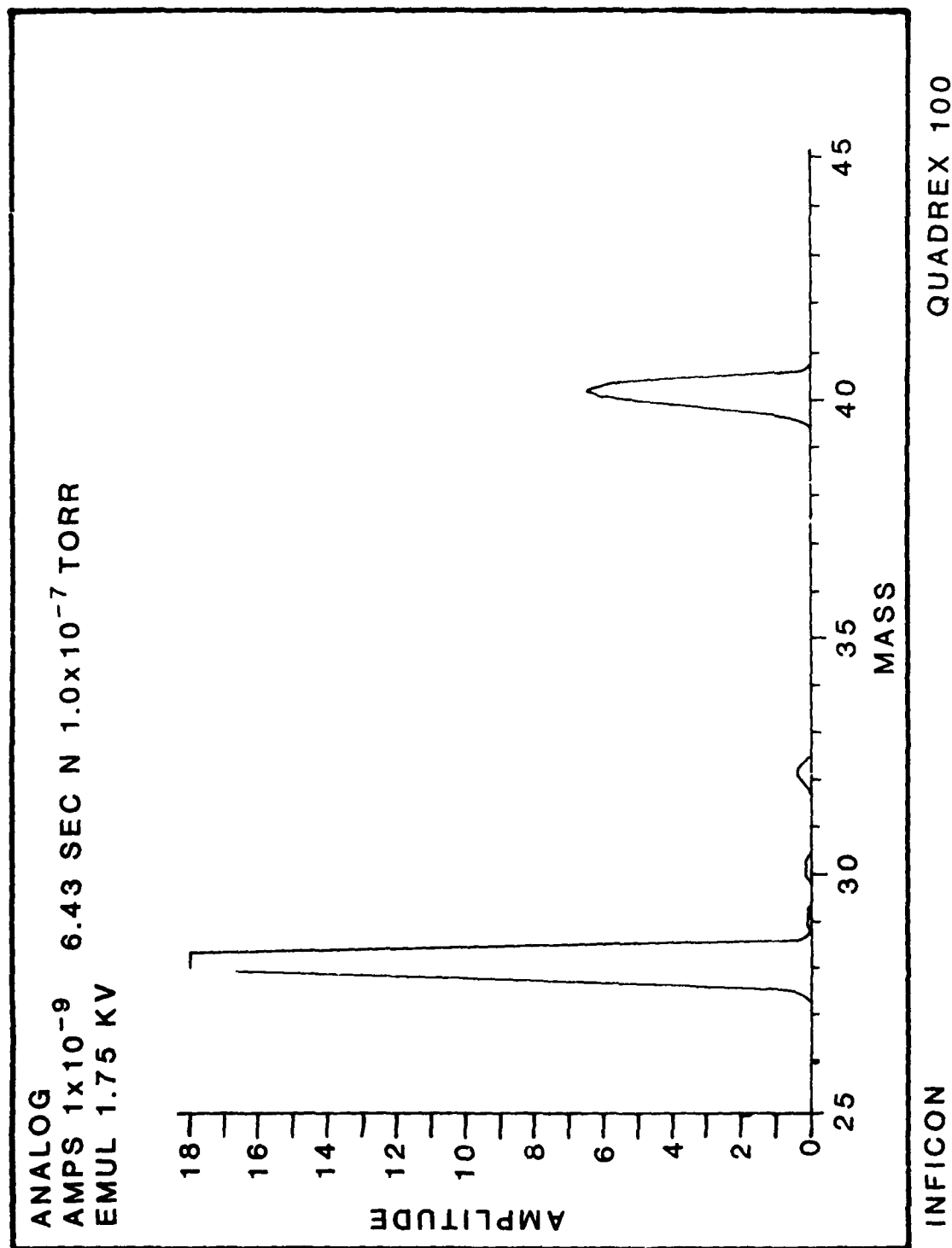


FIGURE 8

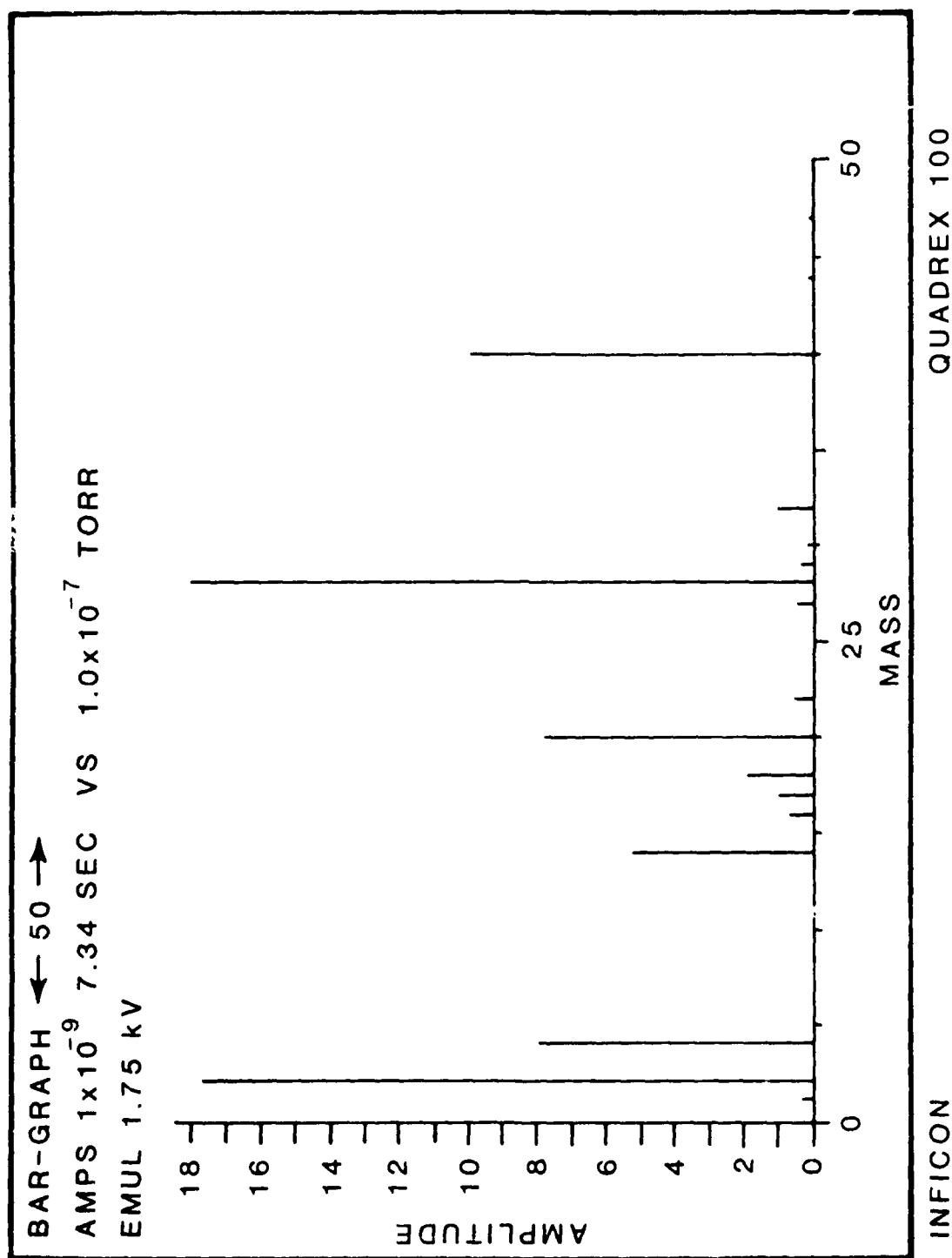


FIGURE 9

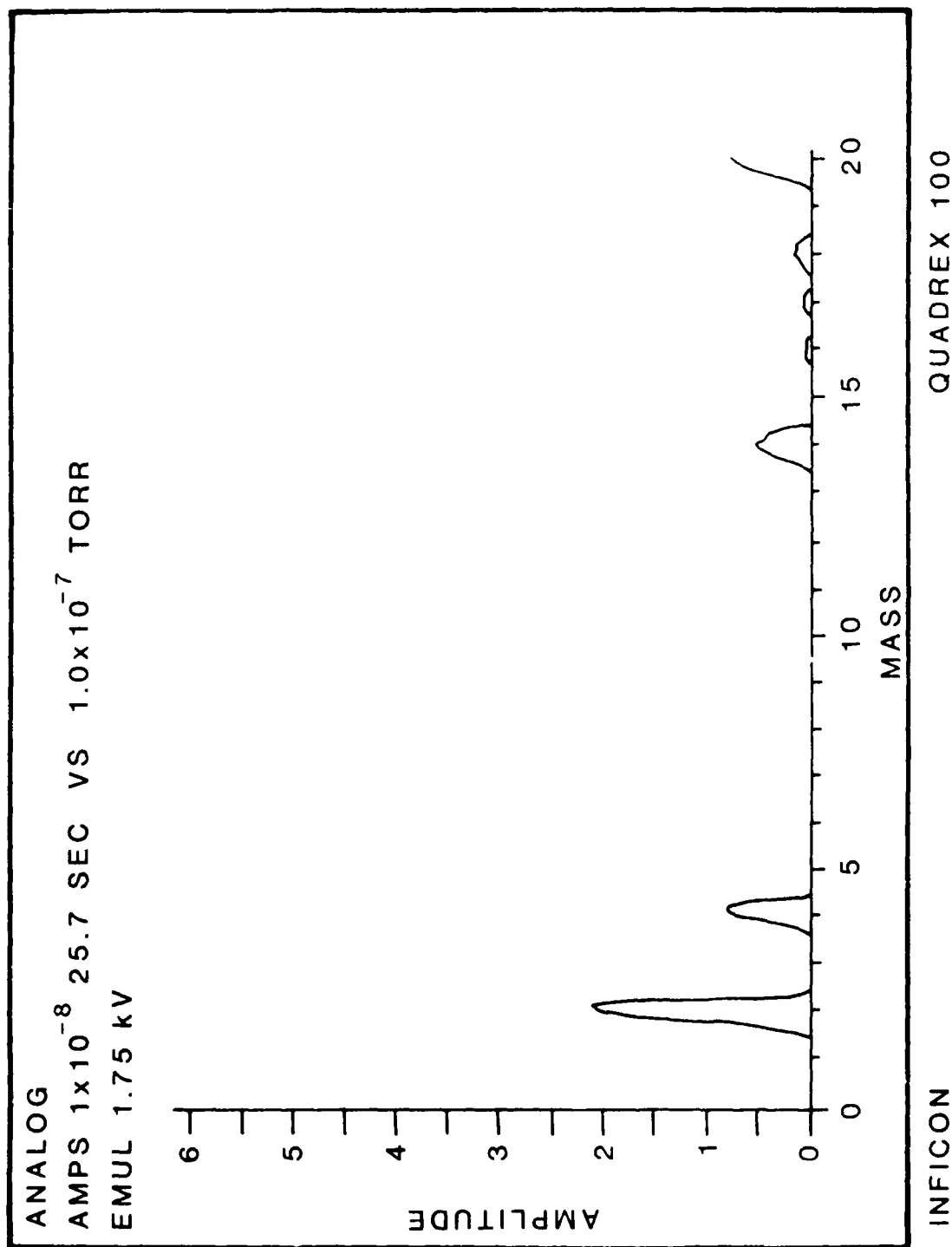


FIGURE 10



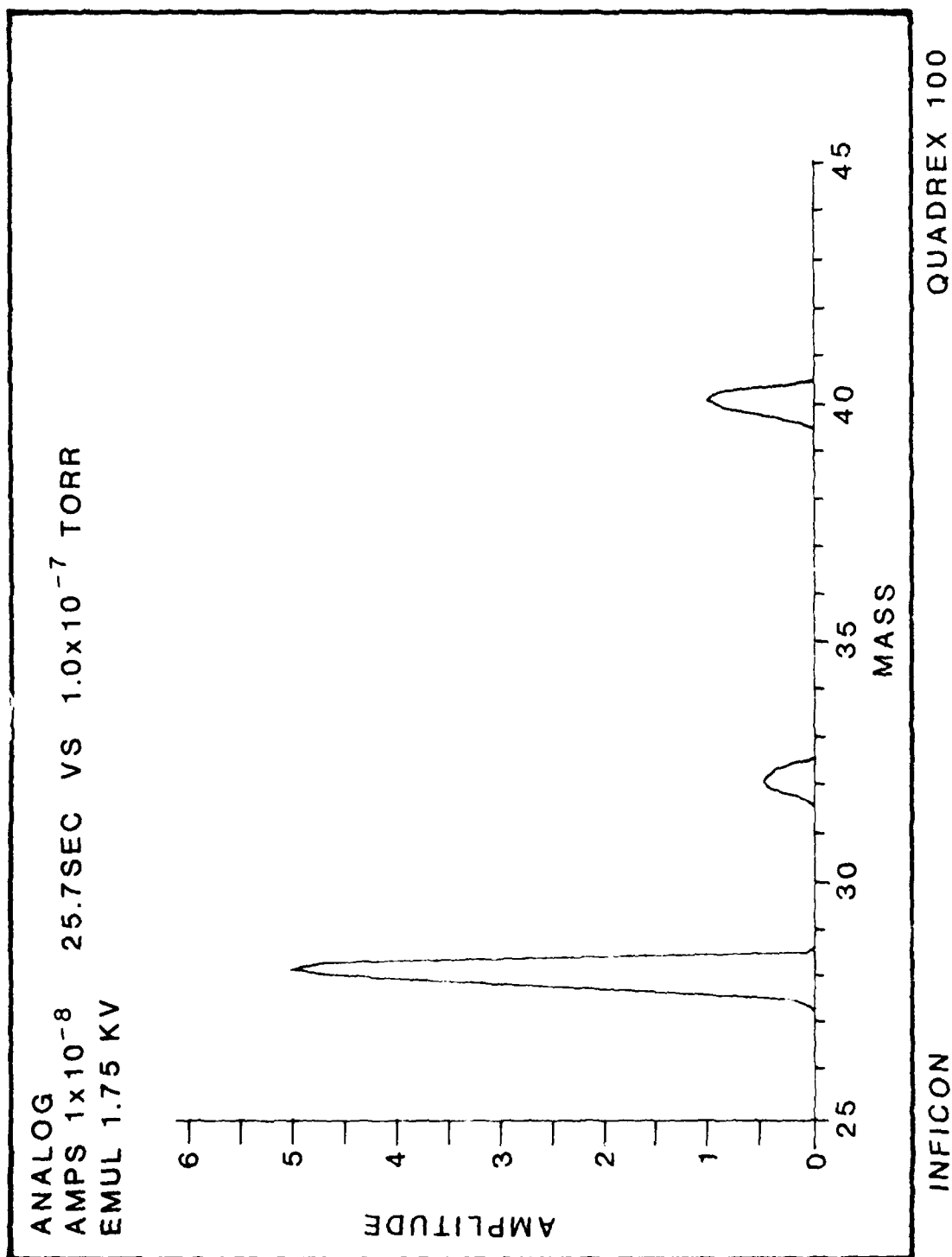


FIGURE 11

present. In a system with a sublimation pump a reactive gas such as oxygen in that quantity must be present due to an air leak. Upon leak checking in the leak check mode, a small leak in the pass-through box valve was detected. The pressure in the system at the time of the leak was  $3.0 \times 10^{-7}$  Torr, which is a good vacuum to achieve in a large bell jar system sealed by elastomers.

System 3 has a R.G.A. sensor head changed. Since the sensor head had been in air for a time, it was degassed by heating on the system. Figure 12 is a bar graph which shows the gases given off by the sensor head as it was heated. The manufacturer had obviously cleaned it in organic solvents. Examination of the spectra by use of charts shows that: mass 2 is hydrogen; mass 12 carbon; mass 14 nitrogen doubly-ionized; mass 15 daughter peak of methane; mass 16 methane; mass 17 due to water vapor; mass 18 water vapor; mass 26, 27 and 29 due to ethyl alcohol; mass 28 is nitrogen; mass 39 a fragment of DC705, a pump oil; mass 41 Isopropyl Alcohol; and mass 44 is carbon dioxide. Figures 13 and 14 are analog spectra of the vacuum system after bake out of the sensor head and the bell jar system. The main constituent is hydrogen at mass 2, next is water vapor at mass 18. Mass 17 is a daughter peak of 18 due to the OH radical. Mass 28 is due to nitrogen.

Main emphasis has been on establishing a guideline for a "normal" reference residual gas analysis for two ultra-high vacuum systems. These systems are used to make platinum silicide infrared detectors. Also included is spectra from an ultra-high vacuum system that is used to make iridium silicide infrared detectors.

The instrumentation used is a quadrupole mass analyzer. The instruments display spectra to mass 100. In our normal operation we check gasses to mass 50, as the systems, when processed and in normal use, have no organic residue that are detectable. When we receive the gas analyzer head we always bake them with the heater to eliminate the residual organic cleaning agents which are left on the head assembly.

AMPS 1E-11 N #1 2.0E<sup>-7</sup> TORR  
EMUL 1.75 KV

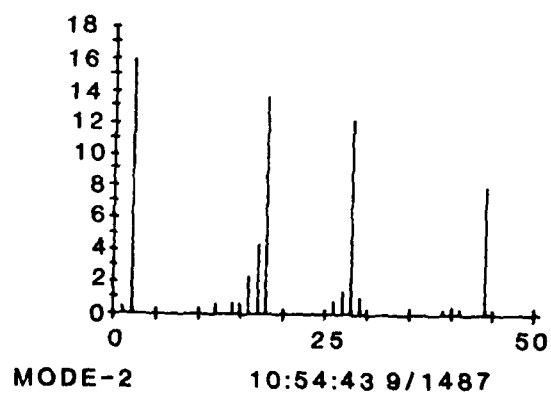


FIGURE 12

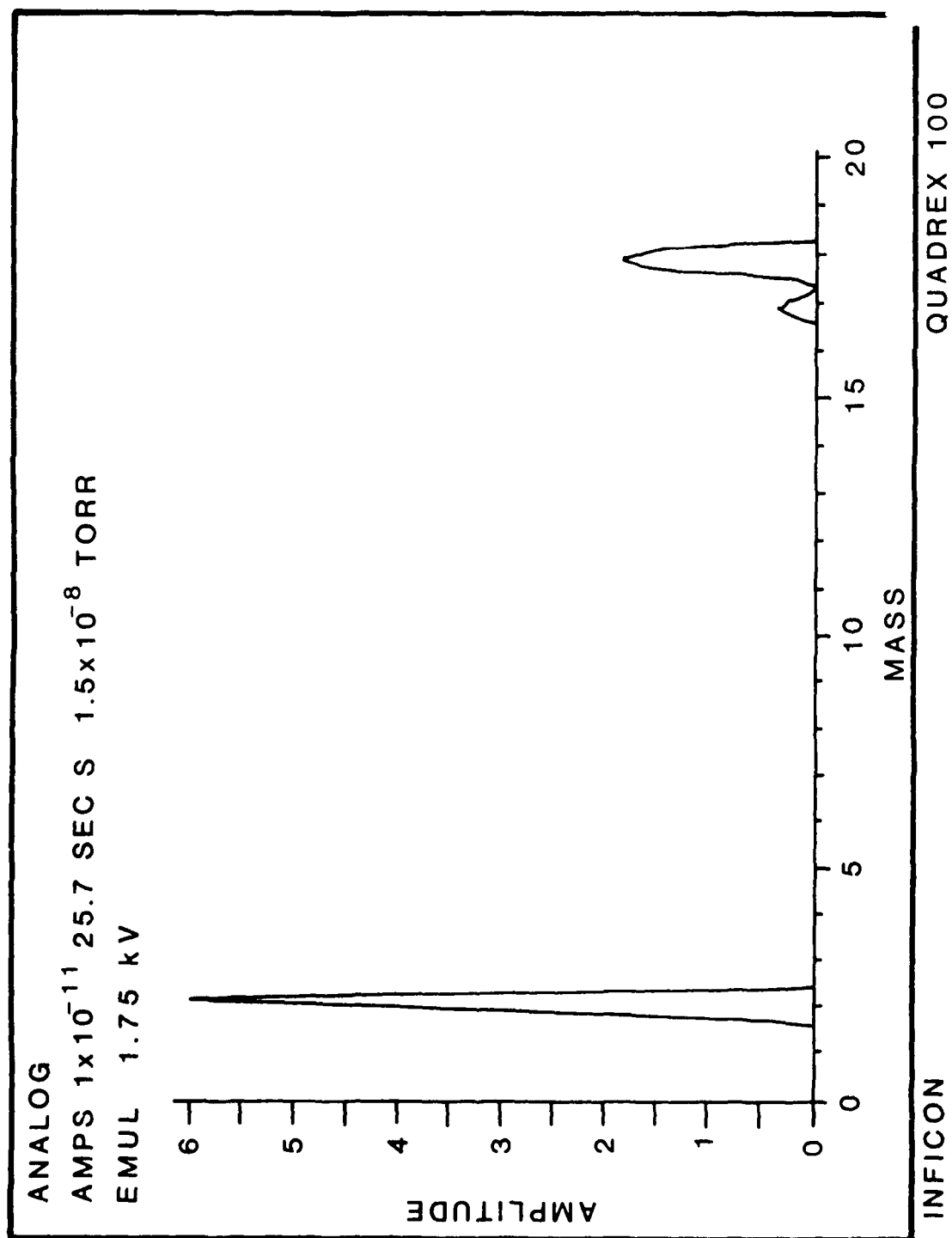


FIGURE 13

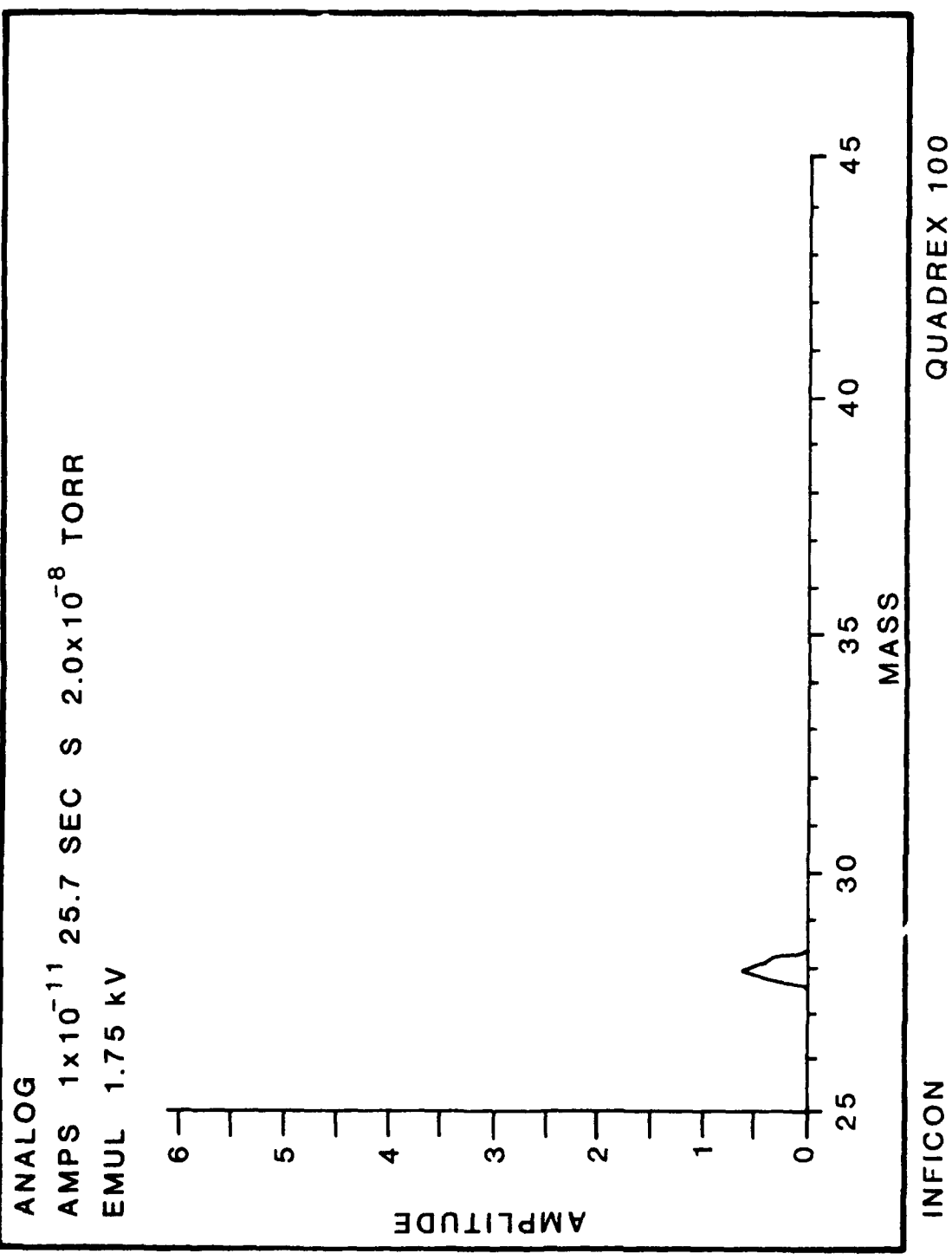


FIGURE 14

In the discussions that follow, reference will be made to three ultra-high vacuum systems. System 1 is a Varian system mainly used at this time to fabricate iridium silicide. System 2 is a G.E. system that has been modified to have a load lock. System 3 is also a G.E. system but without the modification of a load lock.

Figures 15-18 are spectra of the residual gas of system 1. System 1 has a large bell jar and is pumped by a Varian diode sputter ion pump. The sensor head is the old design which gives an extraneous peak at mass 16. Figure 1 is a bar graph of mass 1 to 50. A large reading on a specific mass can cause a spill-over to an adjacent mass number. The vacuum reading is not accurate so we always use the vacuum read by an ion gauge. The vacuum in the chamber is  $1.4 \times 10^{-9}$  Torr as read by a Varian ion gauge control using a nude tube inserted in the vacuum chamber.

Figure 2 is an analog spectra of masses up to mass 20. Examination of this Figure shows that spill-over from zero mass to mass 2 has occurred. The amplitude of the bar graph at mass 2 is close to the half peak seen at mass 2 on the analog picture.

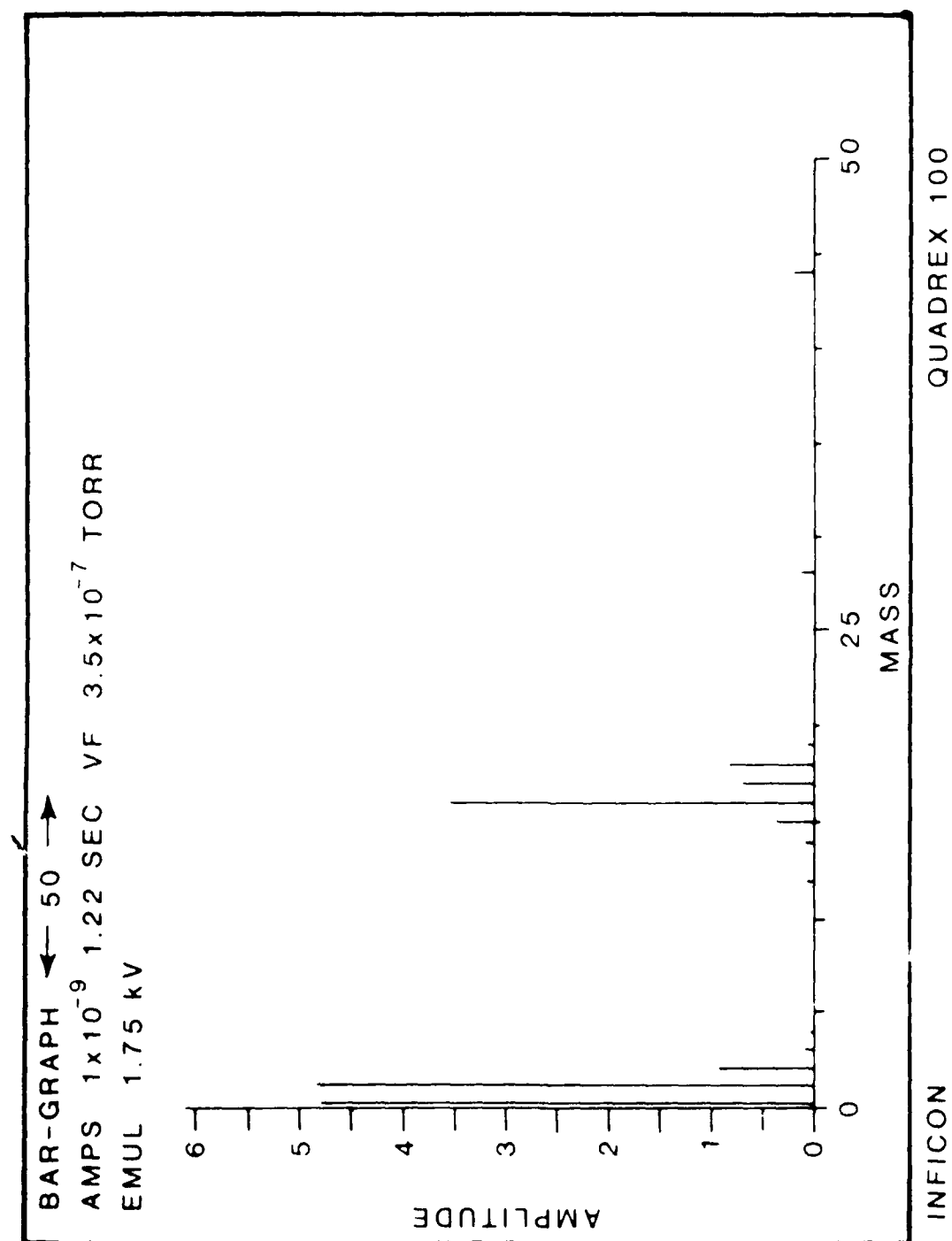


FIGURE 15

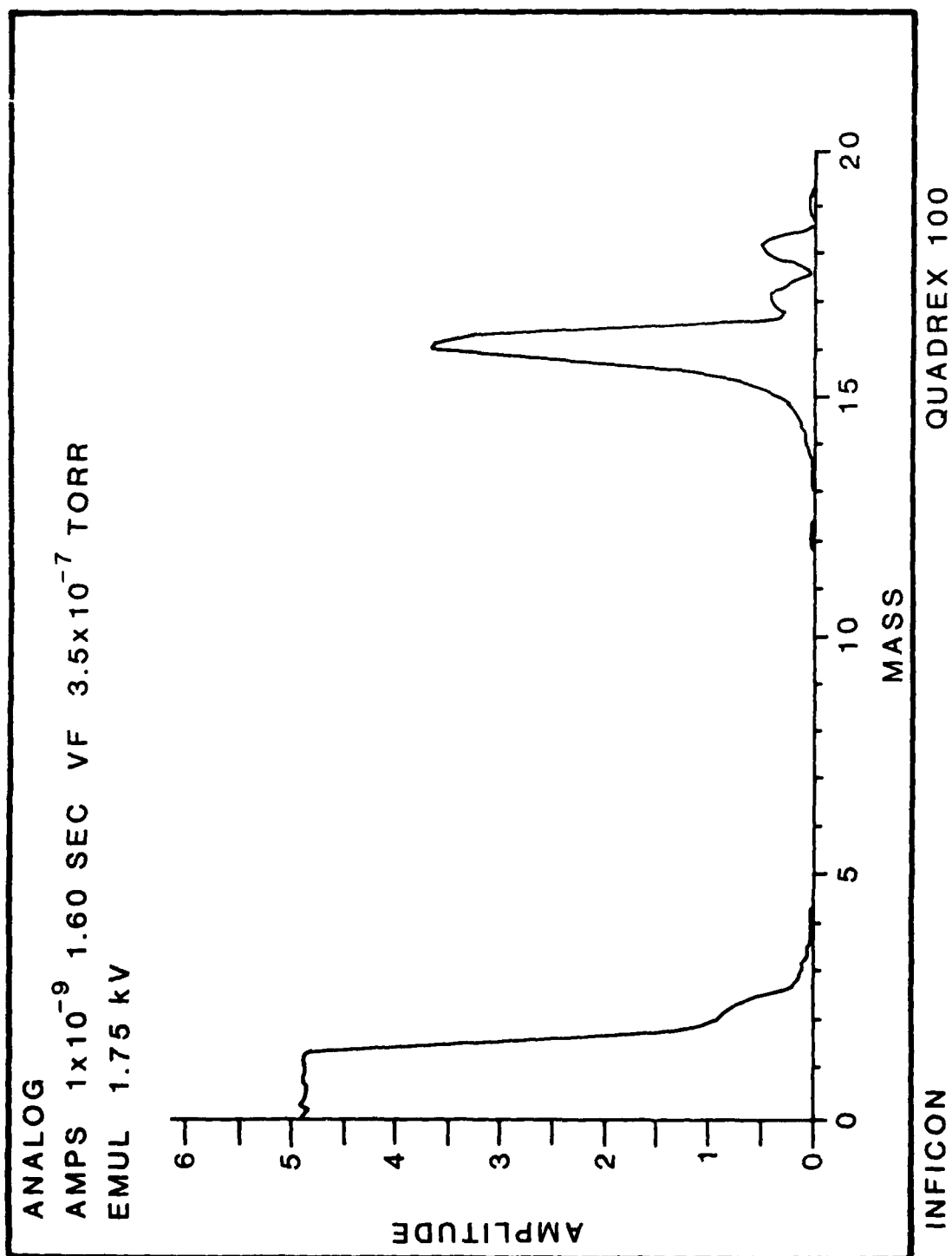


FIGURE 16



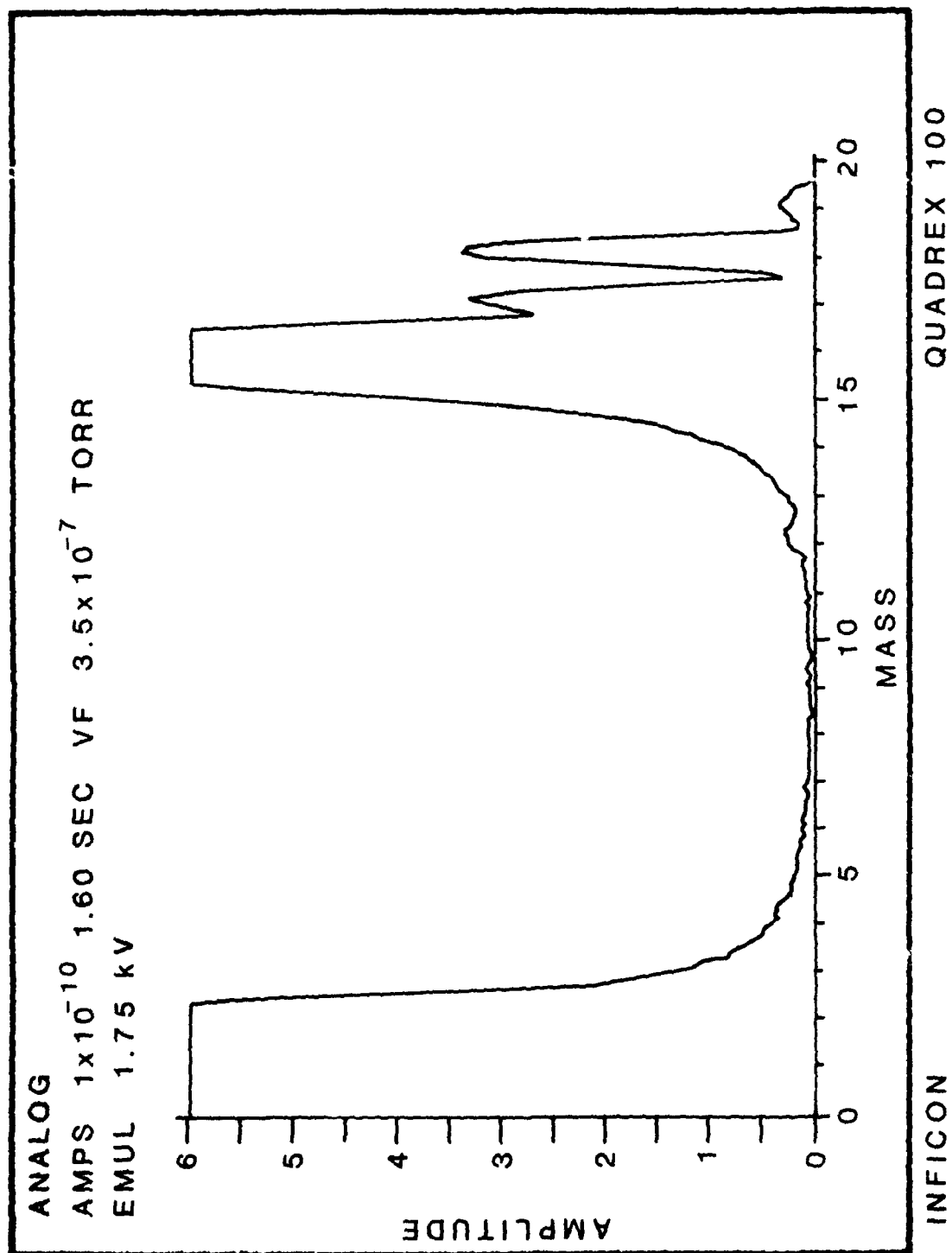


FIGURE 17

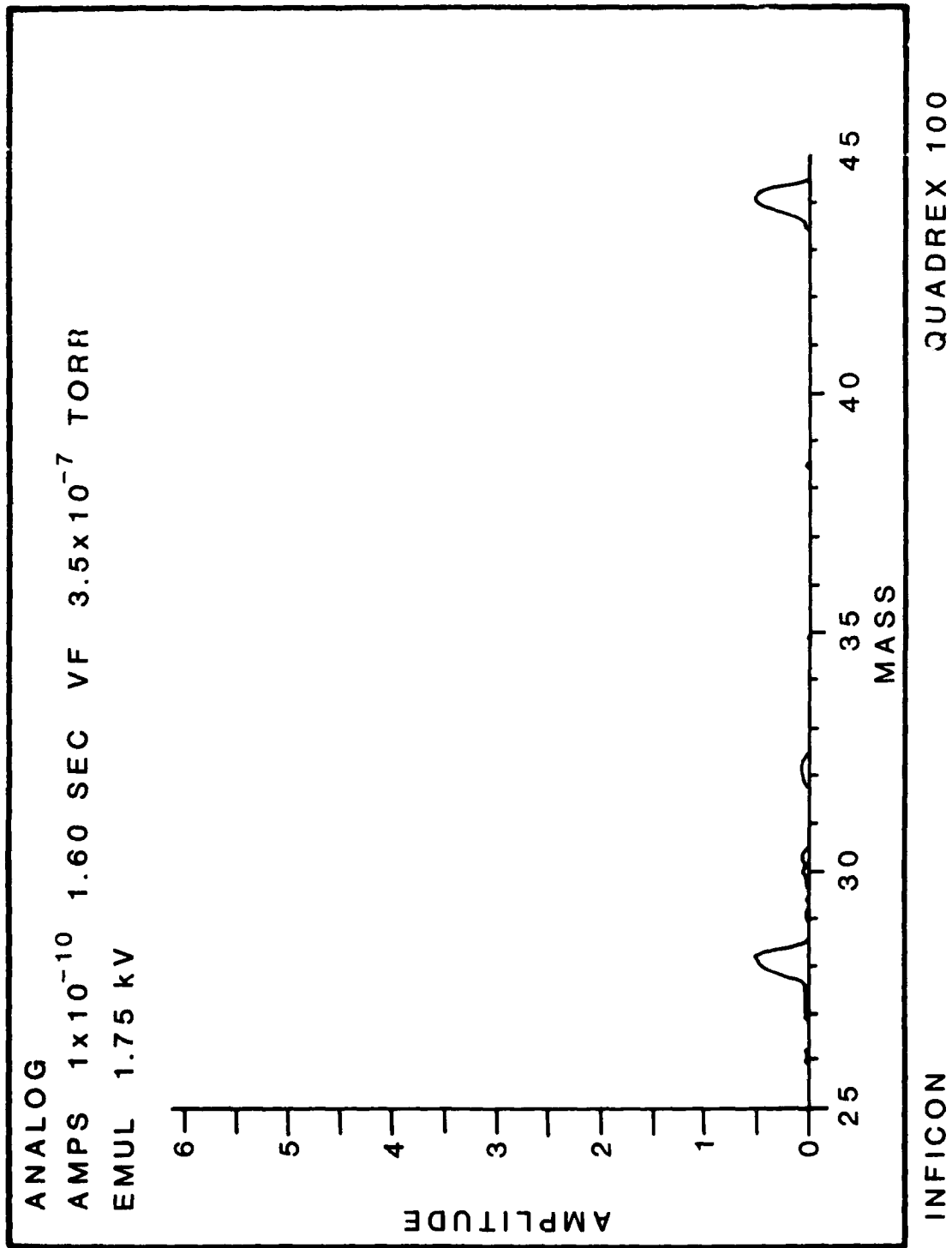


FIGURE 18

## SECTION 2

This section covers problems with system #2 and gives a discussion on a comparison of iridium silicide and platinum silicide photodiodes.

System #2 is a refurbished General Electric vacuum system that has been retrofitted with a load lock. The "O" ring on the high vacuum gate seal has a small residual leak. In order to replace the "O" ring the load lock has to be disassembled from the bell jar. Since the height adjustment is extremely critical personnel have been reluctant to remove the "O" ring. It has been cleaned several times by opening the gate manually and swabbing the seal with a Q-tip saturated with alcohol. This has decreased the leak but not eliminated it. When the load lock is under partial vacuum (i.e.,  $P \approx 10^{-4}$  Torr) the leak is reduced due to the differential pumping. The leak is now leaking at a much reduced rate from  $10^{-4}$  Torr into  $10^{-5}$  Torr instead of  $10^{-4}$  Torr into  $10^{-4}$  Torr. We gain at least one order of magnitude in the vacuum achieved. It is possible the "O" ring was damaged when the height adjustment was made as the scissors fork might have scraped the "O" ring.

The following is a discussion on a comparison of iridium silicide and platinum silicide photodiodes.

## METALLIC STRUCTURE OF SILICIDE

The formation of the different silicides of platinum is well understood for thick layers of platinum. Experiments with diffusion couples as well as with marker atoms have shown that the silicides of Pt form mainly by diffusion of metal into the silicon substrates. In this model, when a near noble metal such as Pt is deposited on a clean silicon surface in thick layers of over 1000Å and then raised to an elevated temperature to form a silicide, the following sequence occurs. The platinum diffuses into the silicon and forms the platinum rich Pt<sub>3</sub>Si compound until all of the platinum is consumed and silicon reaches the back surface of the metal. During this reaction, there is a multi-layer structure which consists of the silicon substrate in

contact with the forming Pt<sub>3</sub>Si, which is in turn in contact with unreacted Pt metal. During the next stage of formation, the Pt<sub>3</sub>Si at the interface begins to form PtSi with the Pt diffusing in from the Pt rich Pt<sub>3</sub>Si. This reaction continues until all of the Pt<sub>3</sub>Si is converted into PtSi and the structure is then stable. The importance of this type of reaction is that during formation of the metallic layer, any impurities which may initially have been at the interface are incorporated into the PtSi layer. This sweeping of the impurities from the interface may account for the high reproducibility and superior optical performance of silicide Schottky barrier photodetectors.

Large area staring arrays of diodes have been fabricated in several laboratories using this technique. The diodes are characterized by 1/f noise which is below 0.1 Hz over most of the array. Occasionally an array is found which may have 1 to 5 noisy detectors. The arrays have 39,000 detectors with measured responsivity uniformity of 99.75% rms. With a simple correction algorithm described by Ewing<sup>1</sup>, the array can be made uniform in responsivity to 99.976% rms.

The silicide formation sequence described above does not necessarily hold for the thin layers of PtSi used for advanced staring focal planes. In fact, when layers of 5A or less are used it has been shown that the phase sequence is metastable leading to the results shown in Figure 1. In that figure, we plot the quantum yield of the photodiode in a modified Fowler plot. Photoemission of a Schottky diode conserves perpendicular momentum as the carrier crosses the metal silicon interface resulting in a quantum yield, Y, expressed as:

$$Y = C_1 * (E - \Psi_{\text{min}})^2 / E \quad (1)$$

where  $C_1$  is the Fowler emission coefficient which depends on metallic parameters,  $\Psi_{\text{min}}$  is the height of the electronic barrier between the metal and the silicon substrate, and  $E = h\nu$  is the energy of an incident photon. The Fowler plot is obtained by linearizing the yield equation so that both  $C_1$  and  $\Psi_{\text{min}}$  can be obtained.

$$\sqrt{Y * E} = \sqrt{C_1} * (E - \Psi_{\text{min}}) \quad (2)$$

There are two distinct linear regions in the first curve of the figure. These two regions give two separate values for emission efficiency ( $C_{11} = 3.2$  and  $C_{12} = 9.9$ ) and barrier heights ( $\Phi_{11} = 0.202$  and  $\Phi_{12} = 0.270$ ). These values are obtained by fitting the two curves in a piece wise linear manner using a least mean squares fit to give the best fit to each straight line. This data was taken about two weeks after the diodes were fabricated. The same diode was measured about 1 year later to obtain a more accurate value for the low barrier portion of the curve. That data, plotted as single slope straight line, (also plotted) shows that a dramatic change has taken place during the year on the shelf at room temperature. To see if this were a pathological diode, we took data again, two years after fabrication, and found it to be unchanged with  $C_{11} = 17.3$  and  $\Phi_{11} = 0.224$ .

These data can be explained using results reported in 1985<sup>11</sup>. Most Fowler curves give a straight line with a single slope. There can be a curvature at both the high energy end caused by counting losses in the excited carrier population and near the intercept on the energy axis caused by hot carrier collisions with the lattice. Both of these phenomena have been described using the Mooney-Silverman<sup>12</sup> extension of Vickers<sup>13</sup> photoemission theory.

Very thin layers of Pt on silicon do not form in PtSi in the fashion outlined above for thick layers. Three different thickness regions have been identified as occurring in the system: a) less than 10Å or 1 to 2 atomic layers; b) between 10Å and 75Å or 3 to 15 layers; and c) greater than 75Å. The thickest layers, i.e. greater than 75Å, show growth characteristics similar to those of the extremely thick or 2000Å samples. The electron diffraction patterns show well defined spots of PtSi, indicating that the metal silicide lattice is well formed and stable. Internal photoemission measurements show that the optical barrier is  $\Phi_{11} = 0.230$  and  $C_{11} = 7$ . A very thin interface layer whose composition is Pt<sub>3</sub>Si with excess Pt was also observed, but the strength of these diffraction rings was small, and extraordinary methods were needed to see the layer. In the intermediate region

of 3 to 15 atomic layers, there was a mixture of all three components, i.e. PtSi with Pt<sub>3</sub>Si and Pt at the interface. The Fowler emission constant,  $C$ , increases with decreasing layer thickness as  $1/t$  down to 15Å. This is an indication that the metal silicide layer covers the silicon substrate with a continuous film.

The thinnest region of 1 to 2 monolayers does not follow the pattern set out above. In fact, the emission constant actually gets smaller, indicating that the surface of the metal is not covering the silicon substrate completely. The material appears to form clusters rather than continuous layers. It is thought that this cluster formation, which is metastable, causes the change in the photoemission characteristics with time. If the clusters were Pt-rich, then lateral diffusion forces could cause the Pt to move out over the unreacted portion of the surface in time to create a continuous film which has emission characteristics similar to thicker films.

Pt films thicker than 3 layers do not show this metastable behavior. They form a structure which does not change with time and have a single emission coefficient. This indicates that there is complete surface coverage at just 3 layers and this coverage will passivate the structure so that there are no changes with time. For the thin, metastable structure it is suggested that the initial phases which form are Pt<sub>3</sub>Si with excess Pt. These two phases lead to a photoemission characteristic shown with the dual slope curve in Figure 1. After a suitable stabilization time, the structure converts to PtSi which has a photoemission characteristic shown in the single slope curve. These results are in line with those reported in 1984<sup>1</sup>, where three different thickness regimes are identified from metallurgical examination of Pt on n-type silicon substrates.

These results allow for a new explanation of the initial growth of Pt deposited on silicon. The first one or two layers deposit in non-equilibrium, platinum-rich clusters which are metastable. Lateral diffusion forces cause the excess platinum in these clusters to become planar with time and convert to PtSi.

For structures having between 3 and 15 layers, the Pt-Si and Pt are in equilibrium with PtSi at varying ratios. Over 15 layers the equilibrium PtSi structure is formed and is unconditionally stable. Fowler plots of PtSi diodes with more than 4 monolayers of metal do not change with time.

#### IRIDIUM SILICIDE FORMATION

The structure and phase formation sequence for iridium on silicon is much more complex than for Pt. The metallurgical Ir-Si system may contain more than 8 intermediate phases as described by Nicolet and Lau<sup>4</sup>. Even though the exact phase diagram is not known, there is general consensus that only three of them form in detectable quantities on silicon substrates<sup>1</sup>. These are IrSi, IrSi<sub>2</sub>, and IrSi<sub>x</sub>. There is considerable disagreement over the value of x in the IrSi<sub>x</sub> structure, but it is known to be between 1.5 and 1.75. Both the x-ray and electron diffraction spectra have been identified for the phase.

The diffusing species is the main difference between Pt and Ir in their formation of silicides. Marker atom experiments in thick Ir layers deposited on silicon show that silicon is the major diffusing species. This would tend to make the final metal-silicon interface much different from that in Pt where a new atomically clean interface is formed at some distance down into the silicon. For Ir, any impurities which are at the interface when the metal is deposited will still exist when the silicide sintering process is finished.

The phase growth sequence can not proceed in a manner similar to Pt since no metal rich iridium silicon phase exists. The temperature of formation of the iridium silicides is higher than in Pt because Si is the main diffusing species. We have noted excellent PtSi formation at temperatures below 200°C, but IrSi requires temperatures in excess of 400-500°C. Furthermore, electron diffraction patterns of diodes with layers between 10Å and 100Å indicate that several different metallurgical phases can coexist in a stable Ir-Si interface. Phase identification shows that there can be up to three different compositions in the metal

layer: namely IrSi, IrSi<sub>2</sub>, and unreacted Ir. The relative compositions change with different processing, but we have yet to find a single phase iridium silicon compound in equilibrium with the silicon substrate.

This leads to considerable variation in our internal photoemission measurements, as well as in electrical and activation energy data. Figure 2 shows a Fowler emission plot for a thin IrSi photodiode having an optical barrier of 0.126 and a long wavelength cutoff of nearly 10 micrometers. The emission constant of  $C_1 = 5.54/\text{eV}$  is a factor of 3 to 4 less than that of PtSi devices and may be a function of the particular phase formed in this diode. The barrier height for this device is corroborated by performing an activation energy analysis as shown in Figure 3. This curve is obtained by measuring the dc current in the diode at 1 volt reverse bias and varying the diode temperature. The results can be analyzed using the Richardson relationship in Equation 3 below, which describes the saturation current in a reverse biased Schottky diode. In this equation  $A_1$  is the Richardson emission coefficient,  $T$  is the temperature in degrees K, and  $k$  is the Boltzman constant. The slope of the line in

$$\ln J_{sat} = \ln A_1 T^2 \exp(-\psi_{barrier}/kT) \quad (3)$$

Figure 3 is related to the electrical height of the Schottky barrier, and for this device the barrier is 0.127eV. Hence, for this device both optical and electrical measurements yield the same barrier. This measurement is made in the dark with cold shields surrounding the device to assure that there is no stray light leakage or infrared photons affecting the current measurement.

In order to show the variability which occurs in the Ir-Si metallurgical system, Figure 4 is included. This is a Fowler emission curve for a diode which was processed nearly identically to that of Figure 2. This figure indicates that two stable phases are present, similar to the results in extremely thin PtSi. The barrier height is about 0.025eV higher than in Figure 2 and the emission constant is about half of that for the device in Figure 2. In terms of its use as a photo detector, this device



cuts off at 8 microns and has only half the responsivity.

PtSi Schottky barrier photodiodes are very well behaved infrared detectors. They can be formed over a sintering range from 200°C to over 400°C and give uniform devices. As long as the thickness of the diode is more than 3 or 4 atomic layers, the structure is stable. There is no indication of a change in these devices with time, even though the metal layers are not passivated in any way.

IrSi offers the potential of making Schottky infrared detectors with response out to beyond 10 microns, or well into the long wave infrared. Some of our measurements which are not reported here have indicated response beyond 12 microns. However, this must still be reconfirmed. The major problem with the IrSi metallurgical system is its tendency to form several different metallic phases in equilibrium with silicon. Each metallurgical phase tends to have its own electrical and optical barrier height, and with several phases present at any one time, it is not clear which one will dominate the photoresponse. Secondly, the major diffusing species in IrSi devices during the formation is silicon. This leads to metal silicon interfaces which are not as atomically clean as they are in PtSi where the diffusion of Pt into silicon causes a fresh metal semiconductor surface to be formed after device sintering. These interfacial inclusions can have an effect on the emission of hot carriers by acting as energy loss scatterers.

#### References:

1. Ewing, W., "Silicide Mosaic Array Compensation," Proceedings of SPIE, Vol. 409, pp. 102-106, April 1983.
2. Silverman, J., et. al., "Characterization of Thin PtSi p-Si Schottky Diodes," Proceedings of the Materials Research Society, Dec. 1985.
3. Mooney, J., and Silverman, J., "The Theory of Hot Electron Photoremission in Schottky-Barrier IR Diodes," IEEE Transactions on Electron Devices, ED-32, No. 1, pp. 32-39, Jan. 1985.

4. Vickers, W., "Model of Schottky Barrier Hot-Electron-Mode Photodetection," *Applied Optics*, Vol. 10, No. 9, pp. 2190-2192, Sept. 1971.
5. Matz, R., et. al., "Chemical Reaction and Silicide Formation of the Pt/Si Interfact," *J. Va. Sci. Technol.*, A2, pp. 253-258, June 1984.
6. Nicolet, M.A., and Lau, S., in VLSI Electronics: Microstructure Sciences, Vol. 6, Chapt. 6, Academic Press, NY, pp. 410-411.
7. Wittmer, M., et.al., "Electronic Structure of Iridium Silicides," *Phys. Rev. B*, Vol. 33, No. 8, pp. 5391-5400, April 1986.

# FOWLER PHOTOEMISSION FOR THIN PtSi LAYER

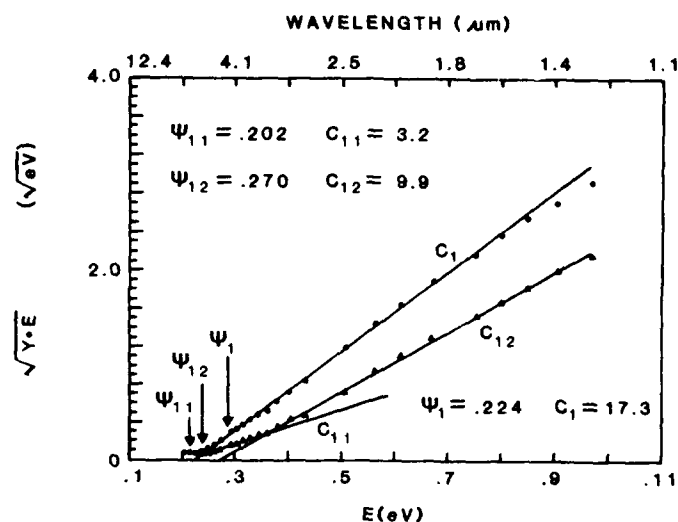


Figure 1

Modified Fowler plot for thin PtSi diode showing metastable conversion of Schottky photoemission with time.

# FOWLER PHOTOEMISSION OF IrSi SCHOTTKY DIODE

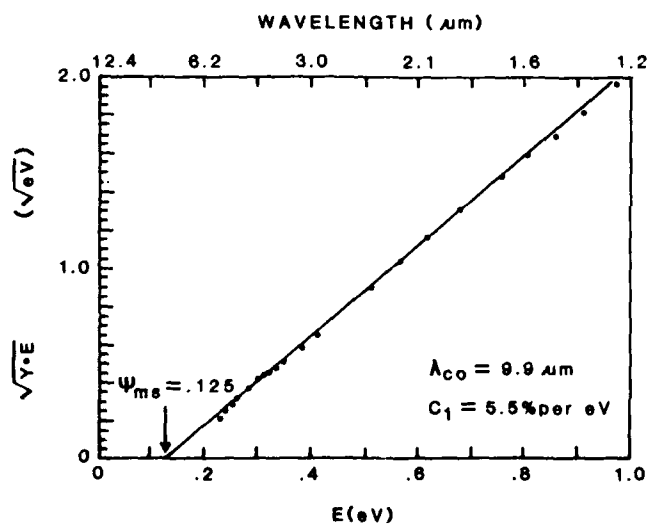


Figure 2

Modified Fowler photoemission plot showing spectral responsivity in the long wave band.

# THERMAL EMISSION OF IrSi SCHOTTKY DIODE

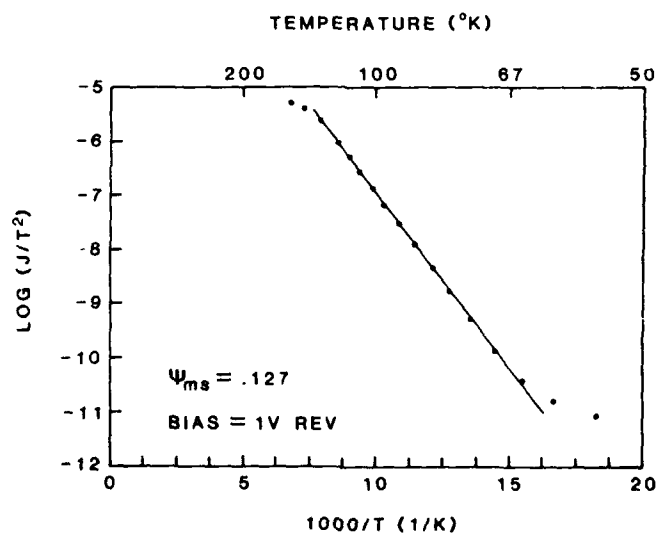


Figure 3

Richardson plot of same IrSi diode as in Figure 2 at 1 volt reverse bias. Measured barrier height is the same using both thermal emission and photoemission.

# IrSi PHOTOEMISSION CHARACTERISTIC

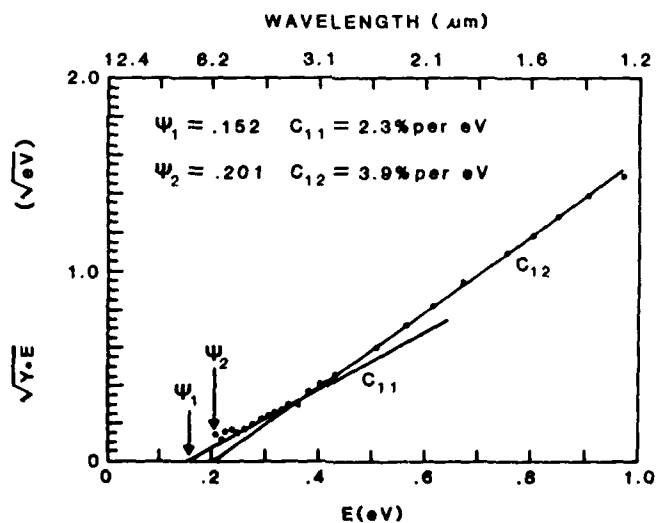


Figure 4

Modified Fowler spectral emission for an IrSi diode showing at least 2 stable phases.

H. John Caulfield

ABSTRACT

The traditional two-hidden-layer neural network is often supposed to offer the best possible classification among input classes. Connecting two such neural networks through an intermediate multiplicative layer can yield full or partial disambiguation of results from a single "traditional" neural network.

## I. INTRODUCTION

Very simple neural networks based on Perceptron-like mechanisms have proved extremely powerful in pattern classification. The key element is a "neuron" such as shown in Fig. 1.

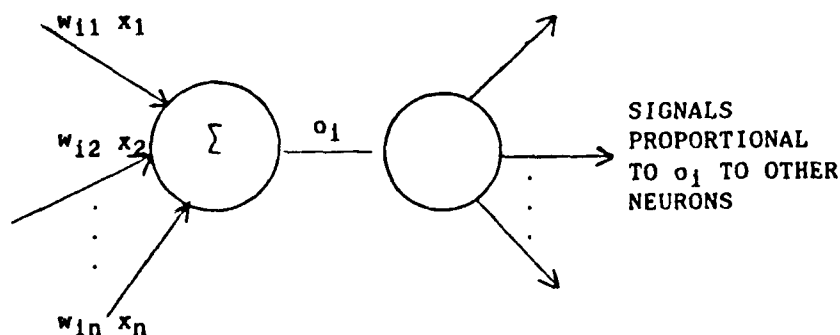


Fig. 1. A Symbolic Representation of a Neuron

The  $i$ th output is

$$o_i = f(s_i)$$

where  $f(\cdot)$  is a nonlinear function and

$$s_i = \sum_j w_{ij} x_j.$$

where  $\vec{x}^T = (x_1, x_2, \dots, x_n)$  is the input vector. We can also write

$\vec{s}^T = (s_1, s_2, \dots, s_m)$  and  $W = \{w_{ij}\}$ . Then

$$\vec{s} = W\vec{x}.$$

These operations are readily interpretable in terms of dividing the decision hyperspace into polygonal regions. The first layer erects planes in the  $\vec{x}$  hyperspace which make decisions (class A on one side; all other classes on the other side). The second layer ANDs such planes to form hyperspace polygons (A inside, not A outside). Since this is the best we

can do in partitioning space, it is widely believed that two hidden layers is the most we ever need.

We show below that additional hidden layers can improve performance and, therefore, the "folk theorem" just stated is highly misleading although technically still correct, if we limit the definition of neural networks sufficiently.

## II. DIDACTIC DEVICE

We will illustrate the arguments with the simplest possible case which illustrates this problem. The input vector will be

$$\vec{x} = (x_1, x_2, \dots, x_n)^T,$$

since we cannot draw  $\vec{x}$  space, we draw a space  $\vec{y} = (y_1, y_2)^T$  chosen to preserve A-B separation to some extent. There will be only two classes: A and B. In  $\vec{y}$  space, we suppose they are distributed as shown in Fig. 2. Classes A and B are not fully separable in  $\vec{x}$  or  $\vec{y}$ . Traditionally, what we do is either (a) partition all of  $\vec{x}$  space anyway knowing this will lead to occasional errors or (b) create a third class, C, which corresponds to "A-B AMBIGUOUS." In either case, we have done all we can and we can do it with only two hidden layers. Or so goes the argument.

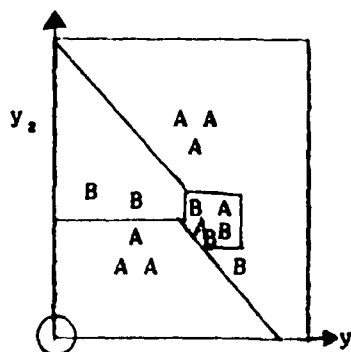


Fig. 2 We show A and B largely separable in  $\vec{y}$  (or  $\vec{x}$ ) space, with a small (hatched) region of ambiguity.

### III. IMPROVING THE SYSTEM

Let us start with the three output (A, B, and C) case. The network is shown symbolically in Fig. 3.

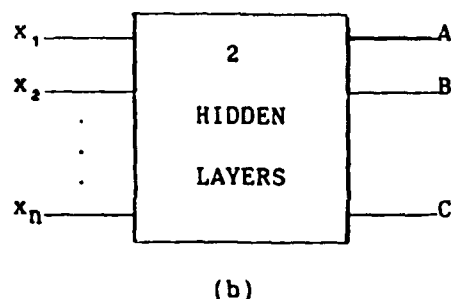
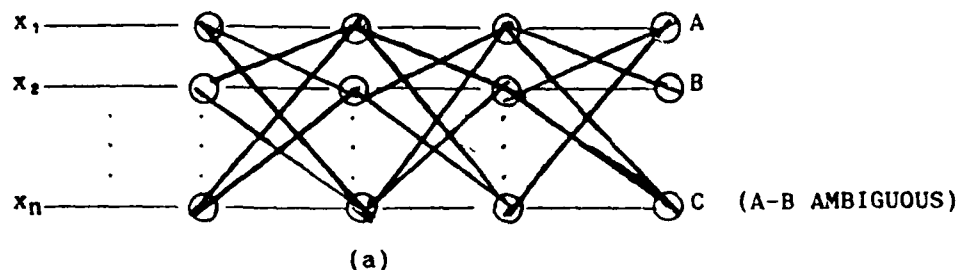


Fig. 3. A two hidden layer neural network generating A, B, and C from  $\vec{x}$  shown in two levels of abstract symbology.

Let us now construct a new neural network with inputs  $c\vec{x}$ . Here the multiplier  $c$  has the effect of making the inputs to this network all zero unless the observed  $\vec{x}$  is A-B AMBIGUOUS. Therefore, we only need to train this neural network on samples from this "ambiguous region. Unlike the first neural network, this one need not trouble to separate A and B samples which were separated in the first neural network. Relieved of this duty, the second neural network can often fully or largely separate events in the "ambiguous" region (1,2). Let us call the first and second two-hidden-layer neural networks NN1 and NN2. We symbolize them as shown in Fig. 4.



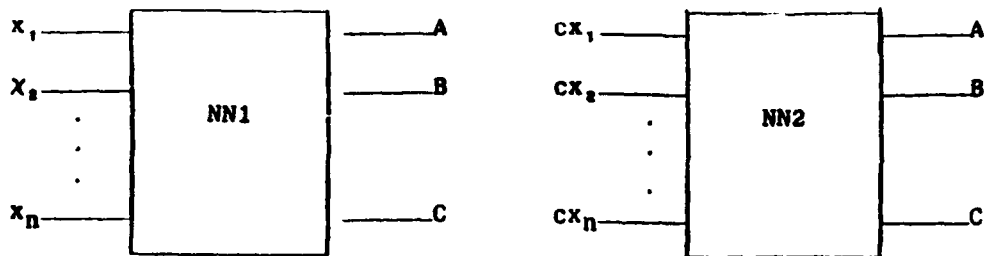


Fig. 4. Symbolic representation of the two networks so far described.

Now we are in position to combine these two neural networks as shown in Fig. 5. Only if the input is ambiguous does C exceed zero and NN2 come into play.

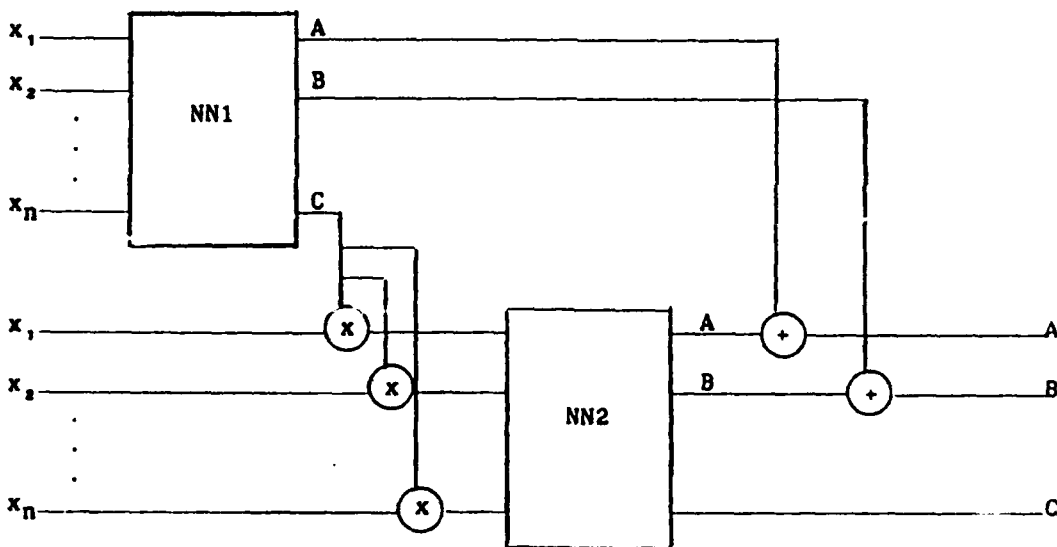


Fig. 5. A combined four-hidden-layer neural network with zero or reduced A-B ambiguity

#### IV. ANALYSIS

Clearly this combined system reduces or eliminates the A-B ambiguity. Furthermore, it is conceivable that more layers would reduce the ambiguity even more.

Clearly two hidden layers do not give all of the separation the data are capable of yielding. The combined neural networks are "untraditional" in the sense that multiplications ( $cx_i$ ) occur in the center layer. There is, however, biological support for multiplicative operations of this type.

Thus, whether or not this multilayer neural network is traditional, it is simple and superior to the traditional neural network in resolving ambiguities.

#### V. REFERENCES

- (1) H. J. Caulfield, R. Haimes, and J. Horner, "Composite Matched Filters," Gabor Memorial Issue, Israel J. of Technol. 18, 263 (1980).
- (2) H. J. Caulfield and R. Haimes, "Optimum Use of Data in Space-Variant Optical Pattern Recognition," Optics and Laser Technology, 310, December (1980).

#### VI. ACKNOWLEDGEMENT

This work was performed for Dove Electronics, Inc. under RADC Contract No. F19628-87-C-0155.

J. Comer

## INTRODUCTION

During the past year there has been a decrease in the amount of time applied to electron microscope studies of PtSi on silicon. In the period the possibility of doing convergent beam electron diffraction with our JEM100CX electron microscope was explored. This technique could be of significant importance in obtaining more detailed information on crystalline materials than can be obtained by the technique of selected area diffraction. Other techniques being used for the first time include ion beam milling of the specimens for transmission electron microscopy and direct lattice imaging applied to superconducting materials with  $c$  spacings of 11.8Å or larger. A new technique for evaluating multilayered structures on GaAs is being used to determine layer thickness and composition of the layers on specimens prepared in the laboratory.

## PtSi ON SILICON

In trying to correlate electrical properties of PtSi on silicon with structures as observed by transmission electron microscopy and electron diffraction, two specimens which had exhibited different electrical properties were compared. These had been prepared by evaporating platinum onto (111) oriented silicon and annealing at 350°C to form PtSi by this solid state reaction between the deposited metal and the silicon substrates. The only difference in the two preparations was in the thickness of the platinum films; one was 50Å thick and the other 100Å. On annealing, PtSi films of 100Å and 200Å respectively were formed.

The results of the investigations, made on specimens thinned chemically from the uncoated surface of the silicon to the PtSi film, showed differences in the orientation of the PtSi on the silicon. Usually the PtSi films show a strong preferred orientation with respect to the silicon in the following epitaxial relationship:

- (1)            (010)PtSi // (111)Si  
              (002)PtSi // <220>Si

The three equivalent  $\langle 220 \rangle$  directions in (111) silicon are responsible for triple positioning of this PtSi. Figure 1a shows the above epitaxial relationship for the 200A PtSi film. Triple positioning cannot be observed here because only a segment of the whole pattern has been selected for comparison. The 100A-thick PtSi film, seen in Figure 1b, shows a second epitaxial relationship:

$$(2) \quad \begin{array}{l} (001)\text{PtSi} // (111)\text{Si} \\ [310]\text{PtSi} // \langle 220 \rangle \text{Si} \end{array}$$

It is known from work on other samples that differences in thickness of the platinum by itself cannot explain these results. Other factors which may affect the orientation are rate of deposition of the platinum and variations in the annealing temperature.

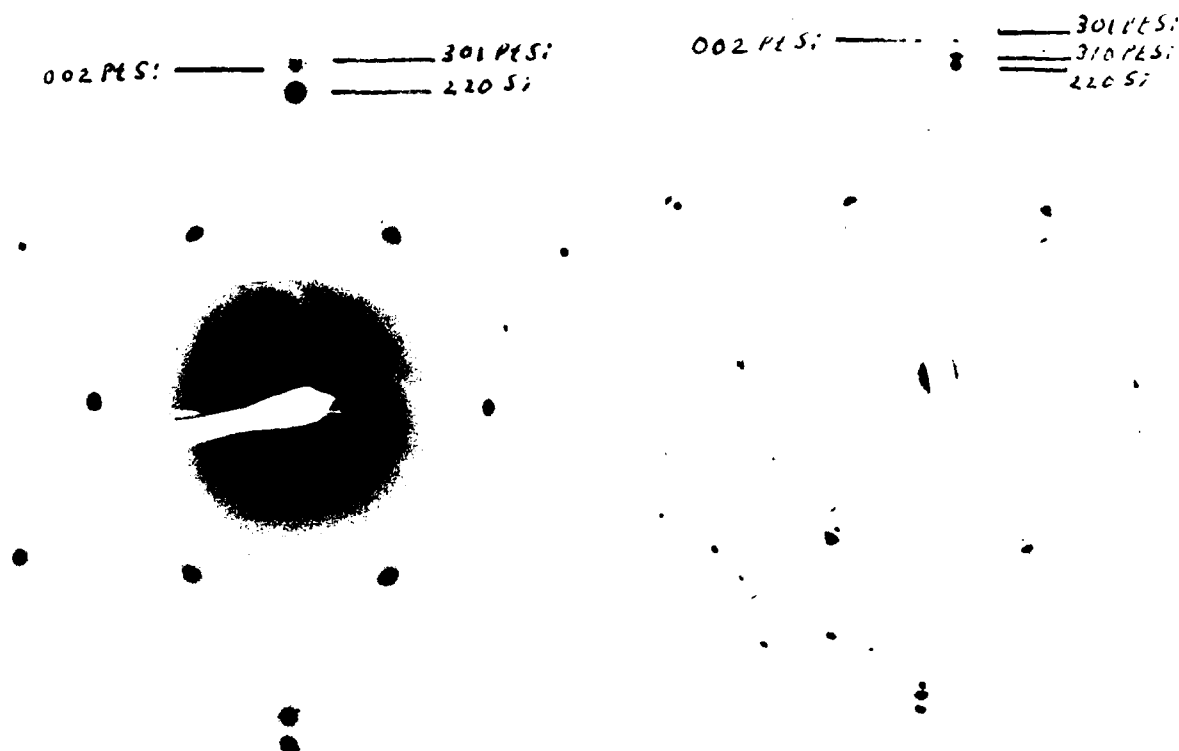


Figure 1: Selected area diffraction patterns of (a) 200A-thick and (b) 100A-thick PtSi on silicon showing different epitaxial relationships to silicon.

#### PHASE SEPARATION IN FLUORIDE GLASSES

Phase separation on freshly-fractured surfaces of glass can often be detected by scanning electron microscopy with a minimum of specimen preparation. However, when there is insufficient contrast because of the very small size and/or low electron scattering power of the precipitate phase a replica technique must be used. The use of a preshadowed carbon replica increases contrast and adds shadows of the precipitate particles that can be used to measure their heights. Micrographs of the replicas were obtained by both transmission electron microscopy and scanning electron microscopy. The latter method was sometimes necessary to separate the background structure of the platinum shadowing metal from that of the separated phase. On the scanning electron micrographs the resolution was sufficient to show the precipitate particles but not the finer grain structure of the platinum. Figure 2 shows a transmission electron micrograph of a replica showing phase separation.

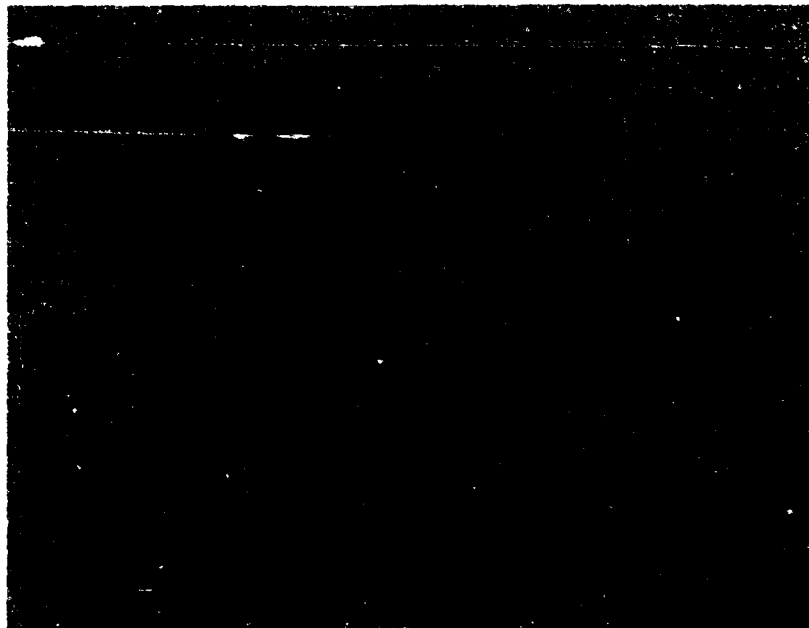


Figure 2: Preshadowed carbon replica of fresh fracture surface of CLAP glass CAΦ. Small particles of the separated phase are seen. The shadow : light ratio is 3:1.

#### DETECTION OF ASBESTOS FIBERS ON MILLIPORE FILTERS

In a continuing investigation of contamination of asbestos fibers, P. Drevinsky submitted specimens collected by air flow on millipore filters. The particles were separated from the filters by evaporating a thin layer of carbon onto the filter surface, scoring the filter into 3mm squares using a scalpel, and dissolving the filter material in acetone. The carbon films containing dust particles extracted from the filter surface were mounted on 200-mesh specimen grids for examination. Chrysotile asbestos fibers, identified by morphology and electron diffraction, were found on sample N 265-4. A report of the findings was submitted to Drevinsky.

#### TEXTURE IN ETCHED SILICON WAFERS

Using preshadowed carbon replicas, specimens of silicon etched in a solution of ROH for 15, 30 or 45 seconds were compared. The sample, submitted by C. Ludington, represent some of the work done in the Electronics Device Technology Branch to determine the effect of surface texture on the electrical properties of their devices. The replicas were separated by lowering sections of the silicon in 7:1  $\text{HNO}_3$ -HF. Change in texture with duration of etch is seen in Figure 3.

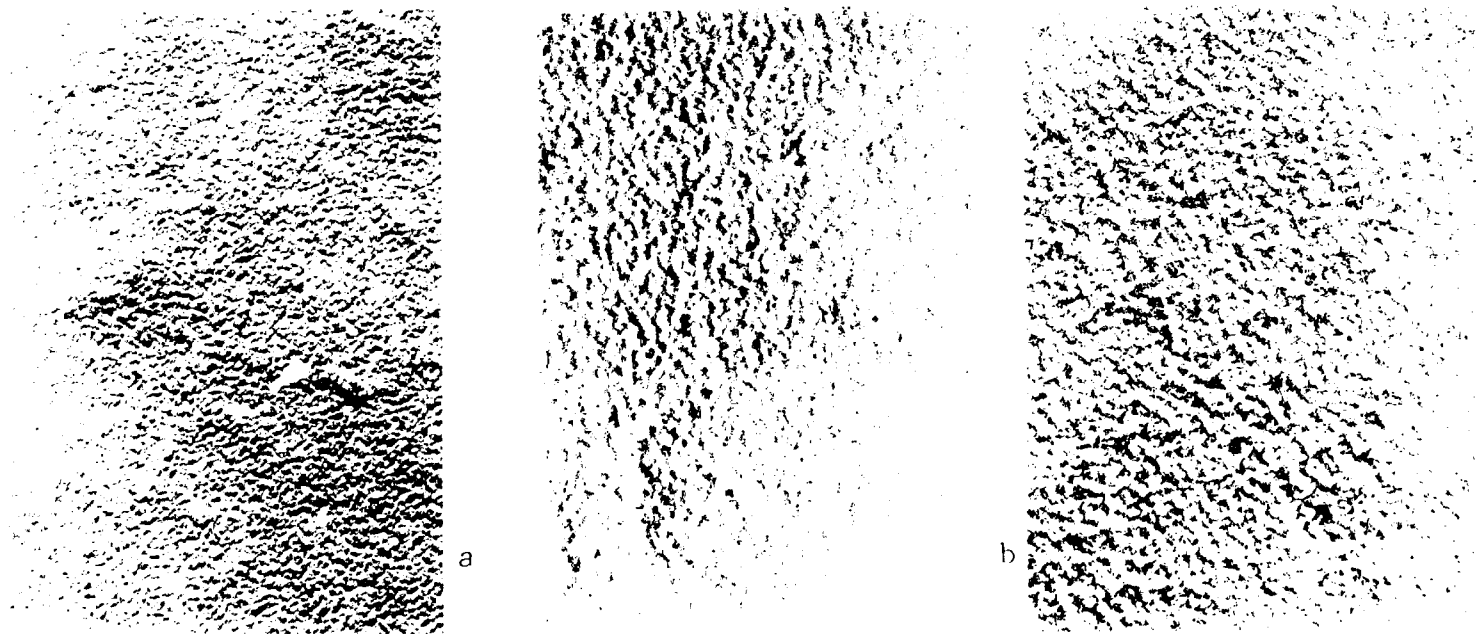


Figure 3: Texture developed on a polished silicon substrate after etching in ROH for (a) 15, (b) 30 and (c) 45 seconds.

### CONVERGENT BEAM ELECTRON DIFFRACTION

Although the present JEM-100CX electron microscope was not designed for convergent beam electron diffraction (CBED) details on adjusting lens currents in the microscope to obtain these diffraction images were obtained from a colleague at the Army Materials and Mechanics Laboratory in Watertown. A series of patterns were obtained for (111) and (100) silicon to determine the effect of altering camera length, beam spot size and condenser lens aperture size. Knowing the proper settings to obtain different kinds of information will be important if the technique is to be used in the analysis of crystalline materials. Details of the method will not be given in this report. It will be sufficient to show the types of patterns which can be obtained and indicate what information they can give beyond that obtained by selected area diffraction (SAD). In the CBED mode the electron beam spot size is less than 400Å as compared with 0.5µm for the SAD mode. This makes it valuable for identifying small particles of an impurity in a second phase. The diffraction spots (hkl reflections) seen by SAD become discs when imaged by CBED. Within these discs there is important information which can be used to determine the crystal structure. Slight changes in lattice parameters, as may be caused by strain, can also be determined from the fine structure within the discs. The patterns can be made to display an outer bright ring which is formed by first order Laue reflections. From the diameters of these rings, interplanar spacings parallel to the electron beam are obtained. The following Figures show how the patterns necessary to obtain the above information can be formed with proper adjustment of spot size, camera length (CL) and condenser lens aperture (C<sub>o</sub>). In all cases the accelerating voltage is 100KV. In Figure 4 reflections from the planes of the crystal are imaged as discs.

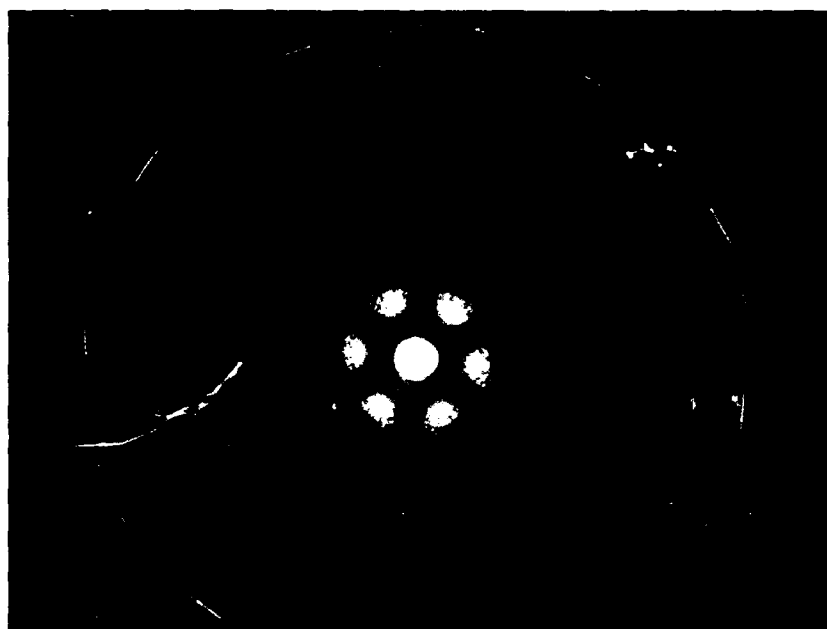


Figure 4: CBED pattern of (111) silicon.  
CL = 46cm, Spot 4,  $C_{\text{ap}} = 300\mu\text{m}$

The bright outer ring is the first order Laue zone (FOLZ) from which the crystal dimension parallel to the incident beam can be determined. When the size of the condenser aperture ( $C_{\text{ap}}$ ) is increased, as in Figure 5 and 6, the discs overlap. The zero order reflection at the center contains lines representing high order Laue zones (HOLZ). When compared with computer-simulated patterns slight changes in lattice parameters can be determined from the spacings of these lines. This pattern also reflects the symmetry of the crystal from which crystal structures can be determined. An atlas of CBED patterns for crystals of various symmetries will be available for rapid identification of crystal class and symmetry'.



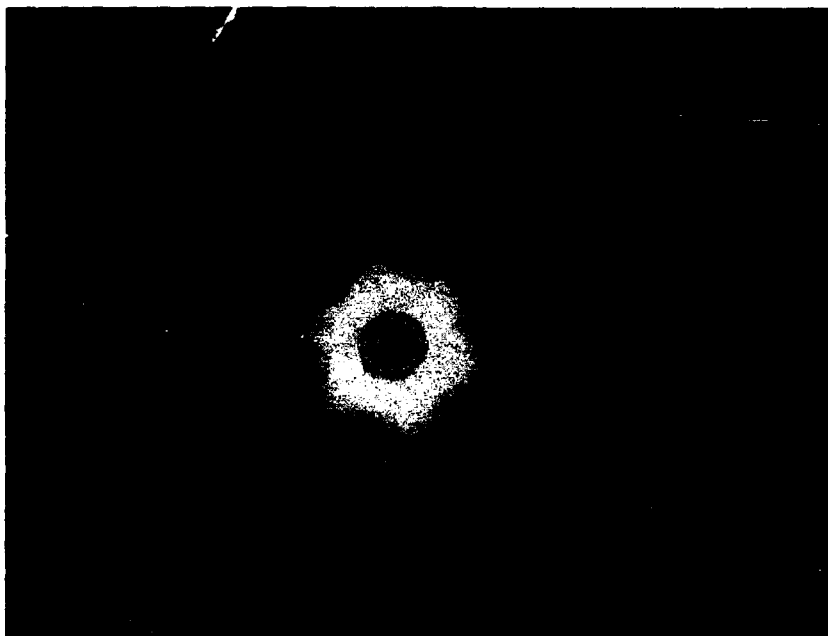


Figure 5: CBED pattern of (111) silicon.  
CL = 76cm, Spot 4,  $C_c = 400\mu\text{m}$



Figure 6: CBED pattern of (111) silicon enlarged to show detail in zero order disc. Same conditions as for image in Figure 5.

Patterns meeting two-beam conditions are made by tilting the specimen to obtain the zero order reflection and a single strong reflection. In Figure 7 this reflection is the 220 of silicon. This type of pattern obtained under CBED conditions shows fringes whose spacings can be used to determine thickness of the specimen.



Figure 7: Kossel-Mollenstadt pattern obtained with 220 reflections of silicon.

#### ION MILLING OF SPECIMENS FOR TEM

In earlier reports of platinum silicide formation on single crystal silicon, electron diffraction showed the existence of a film of platinum at the PtSi/Si interface. Other workers suggested that this film was caused by a chemical reaction between PtSi and the 7:1 HNO<sub>3</sub>-HF used to thin the specimen. In order to determine whether this is what occurred, a specimen of silicon containing 200Å PtSi was thinned using the newly-acquired ion milling unit. Thinning occurs by the bombardment of argon ions at about 6kV. When the thin residual film of PtSi over the hole in the silicon was examined by electron diffraction, there was no platinum. A diffuse ring pattern was identified as coming from amorphous silicon formed by ion damage. This experiment,

along with some earlier evidence, did establish the fact that the interfacial platinum film was an artifact introduced by the chemical method of thinning. The diffraction pattern and the region where it was obtained is shown in Figure 8.

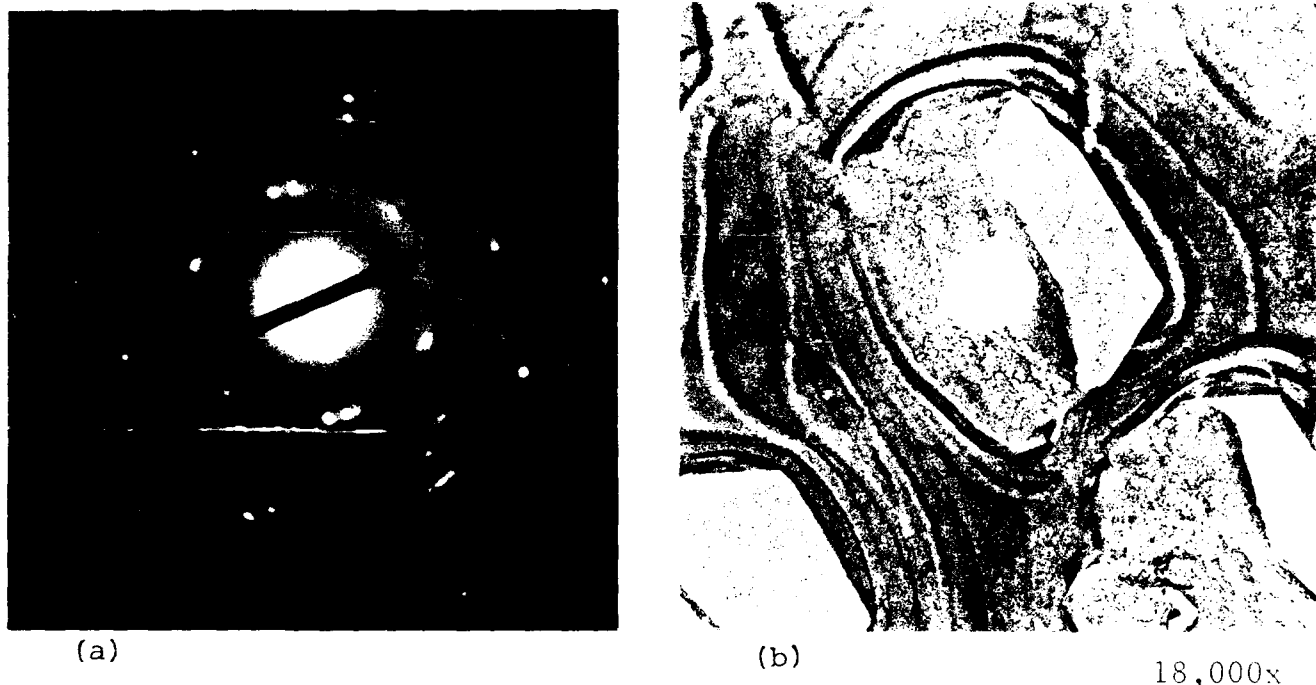


Figure 8: (a) Electron diffraction pattern showing reflections from silicon and PtSi and a diffuse ring pattern from amorphous silicon. (b) Micrograph showing the circular region (light) where the pattern was obtained.

#### TEM OF SUPERCONDUCTING MATERIALS

An investigation of a specimen of orthorhombic  $\text{Ba}_2\text{YCu}_3\text{O}_7$  was started to determine what information could be obtained by transmission electron microscopy of superconducting materials. A powdered specimen made by the sol-gel method was obtained from M. Suscavage. The material was placed in propanol and ground with a mortar and pestle. It was then dispensed by ultrasonic vibration. Large particles were allowed to settle out and a small volume of the supernatant liquid was placed in a specimen grid containing a holey carbon film. Identification was made by selected area diffraction. A lattice image of a crystal with the beam parallel to the  $a$  or  $b$  axis is shown in Figure 9. The (001) planes with spacing of 11.8Å are seen.

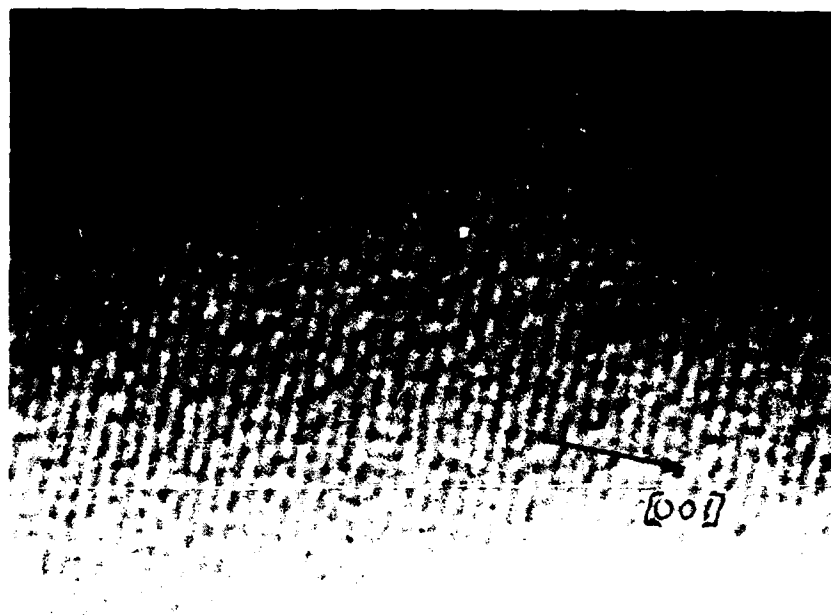
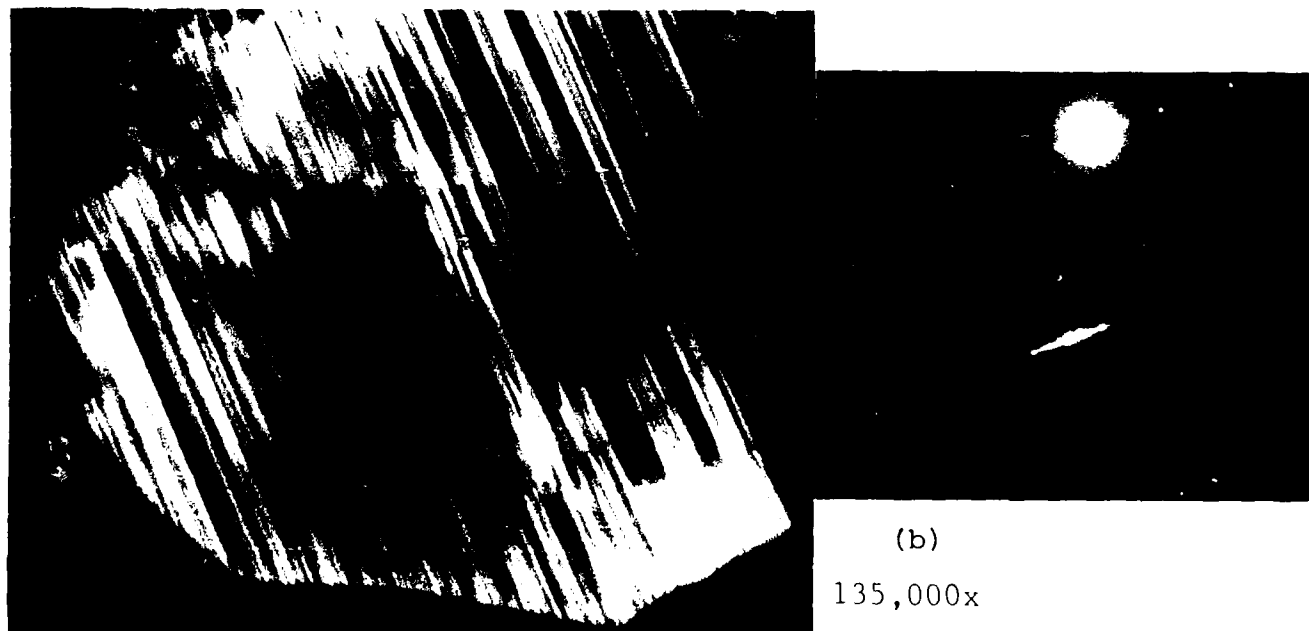


Figure 9: Lattice image of  $\text{Ba}_2\text{YCu}_3\text{O}_7$  showing the (001) planes.

In Figure 10a a dark field image of another crystal is shown. The bright bands are caused by stacking faults normal to the



(a) Figure 10: (a) Dark field image of  $\text{Bu}_2\text{YCu}_3\text{O}_7$ . The bright bands are stacking faults normal to the c-direction. (b) Diffraction patterns showing streaked reflections (within circle) used to form the image.

c-direction. These faults caused streaking of the reflections along the [001] direction as shown in Figure 10b. Faults of this type have been seen by other workers<sup>2,3</sup> but the cause in this particular case has not been established.

#### EQUAL THICKNESS FRINGES IN LAYERED GaAs/Al<sub>x</sub>G<sub>1-x</sub>As

A method for obtaining equal thickness fringes at the intersection of freshly-cleaned (110) and (110) planes in GaAs containing alternating layers of Al<sub>x</sub>G<sub>1-x</sub>As has been described by Kakibayashi and Nagata<sup>4,5</sup>. We are currently attempting to use this technique to examine specimens prepared within the laboratories for the purpose of determining layer thickness and composition from the change in fringe spacing.

#### REFERENCES

1. Tanaka, M. and Terauchi, M., "Convergent-Beam Electron Diffraction," JEOL Ltd., Tokyo, Japan, 1986.
2. Roth, G. et al, A. Phys. B (Condensed Matter), 69, 5359 (1987).
3. Taftø, J. et al, Appl. Phys. Letter, 52 (8), 667 (1988).
4. Kakibayashi, Hiroshi and Nagata, Fumio, Jpn. J. Appl. Phys., 24, L905 (1985).
5. Kakibayashi, Hiroshi and Nagata, Fumio, Surface Science, 174, 84 (1986).

R. Kennedy

## 1. INTRODUCTION

Communication security has been achieved in fiber optic communication systems (IROCS) by ensuring that any undetected intrusion will deliver so little power to a potential intruder that he will not be able to extract any useful information from it. Of course, the system users must receive enough power to extract all of the information that is intended for them. Thus the modulation/coding method that is employed should exhibit a sharp power threshold above which satisfactory performance exists and below which no useful information can be extracted from the signal. The existence of such a threshold reduces the sensitivity that is required of the intrusion detection part of the IROC system.

To date, digital signaling methods have been used to provide the desired threshold. This has been warranted for several reasons. First, at the information rates that have been of interest, the appropriate digital and optical devices have been readily available. Second, digital signaling systems do exhibit a sharp power threshold. Third, the performance of digital receivers is well understood for all received power levels. Consequently, definitive statements concerning the performance achievable by an intruder can be made--at least when the information to be transmitted consists of a sequence of statistically independent symbols.

On the other hand, the use of digital signals limits the feasibility of using IROC systems to transmit wide band analog information. For example, a data rate exceeding 100 Mbps may be required to digitally transmit a 5 to 10 MHz analog video signal. Not only does this exceed the capacity of existing IROC systems, it also entails the use of very wide band and fast analog to digital and digital to analog converters.

Moreover, the fact that the sampled and digitized data stream is highly redundant, i.e. the digital symbols are not statistically independent, means that the arguments concerning

the inability of an intruder to extract any useful "information" are no longer valid. For them to be valid it would be necessary to source encode the data stream so as to eliminate any redundant information and statistical dependencies. This would have the further virtue of reducing the required data rate. However, such source encoding is not now a practical possibility.

Frequency modulation, or more generally angle modulation, may be a useful alternative to digital signaling when analog information is to be transmitted since it too exhibits a sharp performance threshold'. Our work during the past year has been concerned with determining the user performance and intrusion resistance that can be achieved with such modulation.

The determination is complicated by two factors. One is that little theoretical knowledge exists concerning the performance of an FM (or angle modulated) system below the threshold. Second, since the performance is typically measured by a mean square error, or an equivalent signal to noise ratio, the question arises as to how much "information" an intruder may be able to extract from a signal for which the signal to noise ratio is small.

Both of these questions will be dealt with in a fundamental way by upper bounding the performance that an intruder can achieve. In particular, the performance he could achieve if he were allowed to partially specify the modulation format will be determined. To that end we have drawn upon the existing analyses of angle modulation systems to determine the performance for the system user and upon information and rate distortion theory to determine fundamental bounds upon the performance that can be achieved by an intruder.

In the coming months, those results will be combined to determine: 1) the choice of the system parameters that maximizes the guaranteed intrusion resistance, and 2) the resulting intrusion resistance. In the sections that follow, the performance expressions for the intended system user are presented.

We note in passing that some of the results to be obtained in the coming months will be in terms of an achievable mean

square error. To some degree such results will leave open the question of how much "information" an intruder can extract from a very noisy signal. However, as mentioned above, the same issue arises when analog information is transmitted over a digital IROC system by sampling and quantizing without compressing the data to eliminate all redundant information. Moreover some of the results will be expressed directly in terms of information content rather than mean square error.

## 2.1 DEVELOPMENT OF SYSTEM MODEL

The communication system of interest is shown in Figure 2.1. In this section that system will be reduced to suppress the optical subsystem, the performance equations that result from a linearized analysis of the remaining angle modulation system used with a phase locked loop receiver will be presented, and the threshold condition that must be satisfied for the linearized analysis to be valid will be introduced.

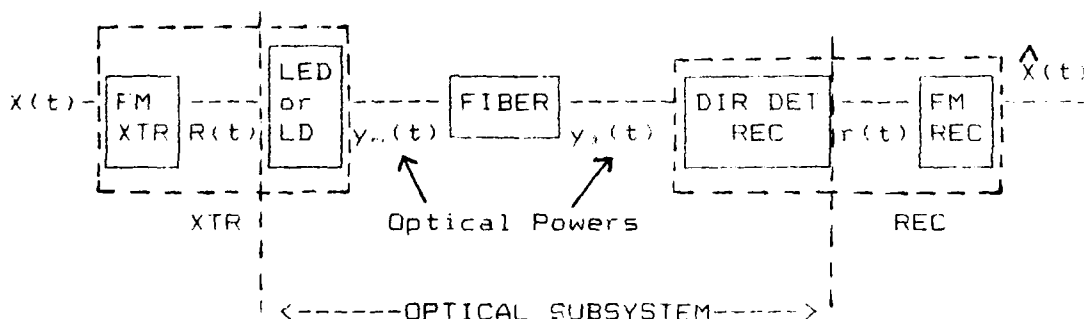


FIGURE 2.1: SYSTEM STRUCTURE

## 2.2 REDUCTION OF SYSTEM

In Figure 2.1  $x(t)$  is the information signal to be transmitted. We take it to be a zero mean wide sense stationary random process with a power spectral density  $S_{xx}(\omega)$ . For convenience,  $x(t)$  will be normalized so that

$$\int_{-\infty}^{\infty} \frac{S_{xx}(\omega) d\omega}{2\pi} = \overline{x^2(t)} = 1 \quad (2.1)$$



In much of the subsequent analysis it also will be assumed that  $x(t)$  is a Gaussian random process.

Referring again to Figure 2.1,  $s(t)$  is a frequency modulated signal produced from  $x(t)$ . Since pre-emphasis will be allowed,  $s(t)$  is given by

$$s(t) = \sqrt{2} \cos(2\pi f_c t + h(t) * u(t) * s(t)) \quad 2.2$$

where  $f_c$  is the subcarrier frequency of the modulated signal,  $h(t)$  is the impulse response of the pre-emphasis filter,  $u(t)$  is the unit step function and  $*$  denotes the operation of convolution.

In Section 3,  $h(t)$  will be chosen either to optimize the system's performance, i.e. to produce what is called Optimum Angle Modulation, or to produce conventional FM. In the latter case  $h(t)$  is

$$h(t) = d_r \delta(t) \quad 2.3$$

where  $\delta(t)$  is the unit impulse function. The significance of  $d_r$  is described below.

Given the normalization implied by Equation 2.1,  $d_r$  can be shown to equal one half the RMS bandwidth of the bandpass signal  $s(t)$ . Stated alternatively,

$$\text{RMS bandwidth of } s(t) = \frac{1}{\pi} d_r \text{ Hz} \quad 2.4a$$

More generally, the RMS bandwidth with pre-emphasis is given by

$$\text{RMS bandwidth of } s(t) = \frac{1}{\pi} \left\{ \int_{-\infty}^{\infty} \frac{d\omega}{2\pi} S_x(\omega) |H(\omega)|^2 \right\}^{1/2} \text{ Hz} \quad 2.4b$$

The modulated signal,  $s(t)$ , is used to amplitude modulate the power output,  $y_e(t)$ , of an LED or LD. More precisely, the short time average of the LED or LD output power is given by

$$y_e(t) = (1 + k s(t)) P_e \quad 2.5a$$

where

$$|k| |P_e| \leq 1 \quad 2.5b$$

and  $P_e$  is the average power that exists when  $s(t)$  is zero.

We assume, realistically, that the power signal  $y_e(t)$  is not distorted by the fiber so that the input,  $y_i(t)$ , to the user's receiver is proportional to  $y_e(t)$ . Specifically,

$$y_r(t) = (1 + k s(t)) P_r L \quad 2.6$$

where L accounts for the attenuation present between the transmitter and the receiver.

The receiver of the intended system user first directly detects  $y_r(t)$  with a photo detector of quantum efficiency  $\eta$ , filters out the DC component of the resulting electronic signal and scales it to produce an output  $r(t)$  that can be represented in the form

$$r(t) = \sqrt{P_r} s(t) + n(t) \quad 2.7$$

In this equation

$$P_r = P_t L \quad 2.8$$

which is the average received optical power in the absence of modulation, i.e. it is the power when  $s(t)$  equals zero.

The quantity  $n(t)$  represents the (scaled) sum of the signal shot noise, the dark current noise, the excess noise associated with detector gain and the noise of subsequent electronics. The mean value of  $n(t)$  will be zero and all but one of its components can be realistically modeled as stationary white noises.

The exception is the shot noise generated by  $y_r(t)$  which, in general, will be time varying with a correlation function

$$R_{r_s}(t, t') = \frac{1}{k^2} \left( \frac{h\nu}{\eta} \right) (1 + k s(t)) \delta(t - t') \quad 2.9$$

where  $h\nu$  is the energy of a photon at the optical wavelength of operation. This noise can be thought of as a non-stationary white noise. However, if  $k$  is small, as it should be to insure that the system remains quantum limited, the correlation function of Equation 2.9 reduces to the correlation function of a stationary white noise with a bilateral power spectral density of

$$\frac{1}{k^2} \left( \frac{\eta}{h\nu} \right).$$

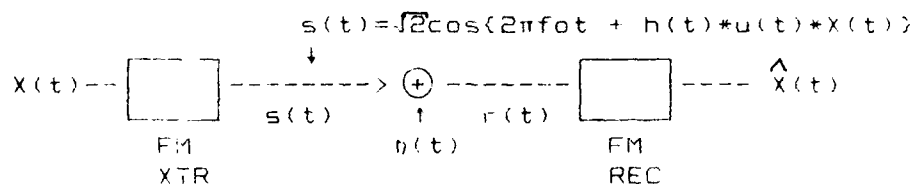
We will assume that  $k$  is small enough for the above reduction to be valid. Then  $n(t)$  is a stationary white noise with a (bilateral) power spectral density of

$$\frac{N_{r_s}}{2} = \frac{1}{k^2} \left\{ \frac{h\nu}{\eta} + \frac{N_e}{2P_r} \right\} \quad 2.10$$

where  $N_e$  denotes the power spectral density contributed by all of

the noises other than the signal generated shot noise.

Equations 2.2, 2.7 and 2.10 allow us to model the system of Figure 2.1 by the reduced system shown in Figure 2.2. This model will be used to determine the performance that can be achieved by the system for an intended user.



$$\overline{x(t)} = 0$$

$$\overline{x^2(t)} = 1$$

$$\text{PSD } x(t): S_x(\omega)$$

$$\overline{n(t)} = 0$$

$$\text{PSD } n(t): \frac{N_w}{2} = \left\{ \frac{1}{4} \frac{h\nu}{\eta} + \frac{4\eta}{2P_r} \right\}$$

$P_r$ : Optical Power Received when  $s(t) = 0$

FIGURE 2.2: REDUCED MODEL FOR SYSTEM USER.  
 ALSO APPLIES TO INTRUDER WHEN  $P_r$  IS REPLACED BY  $\gamma P_r$

For an intruder the system model differs from Figure 2.2 only in that the amount of power received will be smaller than that received by the intended user, i.e. rather than  $P_r$  it will be  $\gamma P_r$  where  $\gamma$  is less than one. Taking that change into account, Figure 2.2 also can be used as a system model for an intruder.

The FM, or more generally angle modulation, system described by Figure 2.2 has been the subject of innumerable investigations. We will draw heavily upon the results of those investigations to determine the performance that the intended user can achieve with the system of Figure 2.1 from which Figure 2.2 was derived. However, first we must specify the receiver that is to be employed in Figure 2.2

### 2.3 RECEIVER STRUCTURE

The receiver can be implemented with either a conventional frequency discriminator or a phase locked loop (PLL) combined with appropriate filtering. The performance of these two implementations is identical when the receiver signal to noise ratio is large enough. However, for smaller signal to noise ratios, the receiver employing a PLL performs better than does one employing a conventional discriminator. Thus the PLL receiver is the better of the two and we will concentrate upon it. However, for purposes of comparison, some results for the discriminator based receiver will be presented in Section 3.

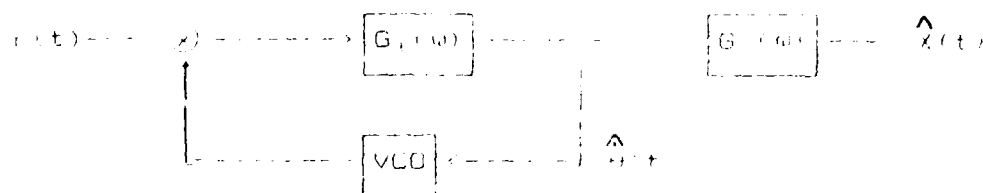


Figure 2.3: LINEARIZED RECEIVER MODEL

The PLL structure to be considered is shown in Figure 2.3. When the signal to noise ratio is large enough for the receiver to work well—as it must for the intended user—its operation is described by a linearized model. Then the receiver filters are properly chosen the output signal to noise ratio, which is the reciprocal of the normalized mean square error in the receiver's output then becomes"

$$(SNR)_u = \left\{ \int_{-\infty}^{\infty} \frac{d\omega}{2\pi} \frac{1}{1 + \frac{2P_s}{N} \frac{S_{xx}(\omega)}{\omega^2} |H(\omega)|^2} \right\}^{-1} \quad (2.11)$$

In writing this expression, the receiver filters have been allowed implicitly to be non-causal. The performance given by the equation can be approached as closely as desired by employing causal filters with a delay to approximate the behavior achieved with the non-causal filter.

To a first approximation the linearized model, and hence equation (2.11) will be valid when  $\theta(t)$  is approximately equal to

$h(t)*u(t)*s(t)$  where  $\hat{\theta}(t)$  is the integral of the quantity  $\dot{\theta}(t)$  which drives the VCO in Figure 2.3. More precisely, the model will be valid if the mean squared value of the difference between these quantities is less than a critical threshold, i.e.

$$[\hat{\theta}(t) - h(t)*u(t)*s(t)]^2 \leq \sigma_c^2 \quad 2.12$$

When this condition is not satisfied, the PLL cannot maintain lock. The value of  $\sigma_c^2$  is subject to debate but a value of 0.25 is often used.

The left-hand member of Equation 2.12 can be expressed in terms of the system parameters. When this is done the threshold condition that must be satisfied for Equation 2.11 to be valid becomes

$$\frac{N_{\text{eq}}}{2P_r} \int_{-\infty}^{\infty} \frac{d\omega}{2\pi} \left[ \ln 1 + \frac{2P_r}{N_{\text{eq}}} \frac{S_{\text{xx}}(\omega) |H(\omega)|^2}{\omega^2} \right] \leq \sigma_c^2 \quad 2.13$$

Little theoretical knowledge concerning the receiver's performance is available when this threshold condition is not satisfied.

Equations 2.11 and 2.13 will be used in Section 3 to determine the system performance. Two choices of the pre-emphasis filter,  $H(\omega)$ , will be of interest there. The first is that which yields straight FM, i.e.

$$H(\omega) = \frac{d_r}{j\omega} \quad 2.14$$

The second is that which yields optimum angle modulation (OAM) in that it maximizes the user output signal to noise ratio subject to a constraint on the RMS bandwidth of the modulated signal  $s(t)$ . In this instance  $H(\omega)$  is chosen to maximize Equation 2.11 subject to a constraint on the value of Equation 2.4b. To facilitate comparison of the FM and OAM results, the value of the bandwidth constraint will be denoted by  $d_r/m$ . Thus the constrained optimization problem becomes

$$\text{maximize} \left\{ \int_{-\infty}^{\infty} \frac{d\omega}{2\pi} \left[ \ln 1 + \frac{2P_r}{N_{\text{eq}}} \frac{S_{\text{xx}}(\omega) |H(\omega)|^2}{\omega^2} \right] \right\} \quad 2.15$$

subject to the constraint

$$\left\{ \int_{-\infty}^{\infty} \frac{d\omega}{2\pi} S_x(\omega) |H(\omega)|^2 \right\}^{1/2} \leq d, \quad 2.16$$

Of course the solution to this problem is significant only when the maximizing  $H(\omega)$  satisfies the threshold condition of Equation 2.13. When it does not, the bandwidth constraint is unimportant and Equation 2.15 should be maximized on the subject to the requirement that the threshold condition of Equation 2.13 be satisfied.

We note in passing that many (although not all) of the results to be presented in the next section are contained in Chapters 4 and 5 of reference 4. Unfortunately, those chapters contain a number of typographical errors that make them difficult for the uninitiated to follow. Therefore, some of the analysis contained there will be presented here for completeness.

### 3. ANALYSIS OF USER PERFORMANCE

The general performance expressions of Section 2 will now be evaluated for some representative message power spectral densities. Since the results vary appreciably with the high frequency roll-off rate of the spectrum, three different families of spectra with significantly different roll-off rates have been chosen. They are described in Section 3.1. All of them have been normalized to have unit power and hence satisfy Equation 2.1.

In the subsequent three sections the signal to noise ratios of the QAM system will be determined for each of these three families. For two of them the performance of the straight FM also will be determined.

#### 3.1 THE REPRESENTATIVE MESSAGE SPECTRA

The first message spectrum to be considered is the bandlimited white one defined as

$$S_x(\omega) = \begin{cases} \frac{1}{2W} & |\omega| \leq W \\ 0 & |\omega| > W \end{cases} \quad 3.1$$

where here, and in the sequel,

$$\Omega = 2\pi W \quad 3.2$$

This spectra represents an extreme in that the frequency roll-off is abrupt.

A second power spectral density of interest is the Gaussian shaped one defined as

$$S_{\omega}(\omega) = \frac{1}{W\sqrt{2\pi}} \exp -1/2 \left( \frac{\omega}{\Omega} \right)^2 \quad 3.3$$

Although its roll-off is not as rapid as is that of Equation 3.1, it is still far faster than that of many spectra.

The Butterworth spectrum

$$S_{\omega}(\omega) = \frac{2n}{\Omega} \frac{\sin(n/2n)}{1 + (\omega/\Omega)^{2n}} \quad 3.4$$

has been chosen to represent the slower roll-off that is sometimes encountered. In fact, it can be used to represent a broad variety of roll-off rates by varying the parameter  $n$ . The fastest roll-off rate is obtained by letting  $n$  approach infinity. Then the Butterworth spectrum approaches the bandlimited spectrum of Equation 3.1. The slowest roll-off rate is obtained by setting  $n$  equal to one which yields the first order Butterworth spectrum. In this report only the first order Butterworth spectrum will be considered.

### 3.2 BAND-LIMITED WHITE MESSAGE SPECTRA

For straight FM

$$H(\omega) = d, \quad 3.5$$

Introducing Equation 3.1 and 3.5 into Equation 2.11 and evaluating the integral yields the following expression for the intended user's output signal to noise ratio when the FM threshold is exceeded.

$$(SNR)_u = \begin{cases} 1 & \text{if } \left( \frac{\Omega}{d_r} \right) \sqrt{\frac{N_0 W}{P}} \geq \tan^{-1} \left( \frac{\Omega}{d_r} \right) \sqrt{\frac{N_0 W}{P}} \\ \left( \frac{\Omega}{d_r} \right) \sqrt{\frac{N_0 W}{P}} & \text{if } \left( \frac{\Omega}{d_r} \right) \sqrt{\frac{N_0 W}{P}} < \tan^{-1} \left( \frac{\Omega}{d_r} \right) \sqrt{\frac{N_0 W}{P}} \end{cases} \quad 3.6$$

For the performance to be satisfactory this signal to noise ratio must be large. Then Equation 3.6 becomes approximately

$$(\text{SNR})_u = 3 \frac{P_s}{N_o W} \left( \frac{d_r}{\Omega} \right)^2 \quad 3.7$$

Equation 3.7 is valid only when the system is above the FM threshold. For the system at hand, that threshold is given by Equation 2.13, in combination with Equations 3.1 and 3.5. The result is

$$\frac{N_o W}{P_s} \left\{ \ln \left[ 1 + \left( \frac{d_r}{\Omega} \right)^2 \frac{P_s}{N_o W} \right] + 2 \frac{d_r}{\Omega} \sqrt{\frac{P_s}{N_o W}} \tan^{-1} \left( \frac{\Omega}{d_r} \sqrt{\frac{N_o W}{P_s}} \right) \right\} \leq \sigma_r^2 \quad 3.8$$

The argument that allowed Equation 3.5 to be approximated by Equation 3.7 implies that Equation 3.8 is given approximately by

$$\frac{N_o W}{P_s} \left\{ 2 + \ln \left( \frac{d_r}{\Omega} \right)^2 \frac{P_s}{N_o W} \right\} \leq \sigma_r^2 \quad 3.9$$

which can also be written as

$$\frac{d_r}{\Omega} \leq \frac{1}{\sqrt{P_s / (N_o W)}} \exp 1/2 \left[ \frac{\sigma_r^2 P_s}{N_o W} - 2 \right] \quad 3.10$$

When the system is operated at the FM threshold, so that Equation 3.10 is satisfied with equality, the output signal to noise ratio of Equation 3.7 is

$$(\text{SNR})_u = 3 \exp \left[ \frac{\sigma_r^2 P_s}{N_o W} - 2 \right] \quad 3.11$$

To determine the performance improvement that can be achieved through pre-emphasis the constrained maximization problem described by Equation 2.15 and 2.16 must be solved for the message spectrum of Equation 3.1. For that spectrum those equations become

$$\max_{H(f)} \left\{ \int_0^{\Omega} \frac{d\omega}{\Omega} \frac{1}{1 + \frac{P_s}{N_o W} \frac{|H(\omega)|^2}{\omega}} \right\} \quad 3.12$$

and

$$\int_0^{\Omega} d\omega |H(\omega)|^2 \leq \Omega d_r^2 \quad 3.13$$

For the signal to noise ratios of interest here, Equation 3.12 is maximized when



$$|H(\omega)|^2 = \begin{cases} \frac{N_c W}{P_s} (Q - \omega) \omega & ; \quad |\omega| \leq \Omega \\ 0 & ; \quad |\omega| > \Omega \end{cases} \quad 3.14$$

where

$$Q = \frac{2\Omega}{3} \left[ 1 + \frac{3P_s}{N_c W} \left( \frac{d_r}{\Omega} \right)^2 \right] > \Omega \quad 3.15$$

As suggested by equation 3.15, the solution is only valid when  $Q$  exceeds  $\Omega$ --a requirement that is consistent with our interest in large signal to noise ratios.

Upon combining Equations 3.12, 3.14 and 3.15 and evaluating the integrals one obtains the following expression for the output signal to noise ratio of the DAM system

$$(SNR)_u = \frac{4}{3} + \frac{4P_s}{N_c W} \left( \frac{d_r}{\Omega} \right)^2 \approx \frac{4P_s}{N_c W} \left( \frac{d_r}{\Omega} \right)^2 \quad 3.16$$

Of course, Equation 3.16 is only valid when the signal to noise ratio is large enough to maintain loop lock, i.e. large enough to satisfy the constraint condition of Equation 2.13. For the message spectra and pre-emphasis filter being considered here that condition becomes

$$\frac{N_c W}{P_s} \left\{ 1 + \ln \left( \frac{4}{3} \right) \left[ 1 + \frac{3P_s}{N_c W} \left( \frac{d_r}{\Omega} \right)^2 \right] \right\} \leq \sigma_s^2 \quad 3.17$$

For large signal to noise ratios the condition is given approximately by

$$\frac{N_c W}{P_s} \left[ \ln \frac{4P_s}{N_c W} \left( \frac{d_r}{\Omega} \right)^2 \right] \leq \sigma_s^2 \quad 3.18$$

Equation 3.18 determines the largest value of  $d_r$  that is useful, i.e. the value such that the system is operating at the threshold. When that threshold value of bandwidth is used the signal to noise ratio of the DAM system becomes

$$(SNR)_u \approx \exp \left( \frac{\sigma_s^2 P_s}{N_c W} \right) \quad 3.19$$

### 3.3 GAUSSIAN SHAPED MESSAGE SPECTRA

For the Gaussian shaped message spectra given by Equation 3.3 only the performance of the DAM system will be determined. The fact that this spectral density is strictly monotonically

decreasing for positive frequencies can be used to significantly simplify the maximization problem defined by Equation 2.15 and 2.16. In particular, when the bandwidth constraint  $d_r$  is not too large<sup>22</sup>,

$$(SNR)_u = \left\{ \frac{2\sqrt{S_{xx}(\omega^*)}}{\omega^*} \int_0^{\omega^*} [\omega^2 S_{xx}(\omega)]^{1/2} \frac{d\omega}{2\pi} + 2 \int_{\omega^*}^{\infty} \frac{S_{xx}(\omega) d\omega}{2\pi} \right\}^{-1} \quad 3.20$$

where the value of the parameter  $\omega^*$  is determined from the expression

$$\int_0^{\omega^*} \left[ \frac{\omega^* \sqrt{S_{xx}(\omega)}}{S_{xx}(\omega^*)} - \omega \right] \frac{\omega d\omega}{2\pi} = \frac{P_r}{N_{LW}} d_r^2 \quad 3.21$$

As  $d_r$  increases the point will be reached where the pre-emphasis filter that maximizes Equation 2.15 subject to the bandwidth constraint of Equation 2.16 will not satisfy the threshold condition given by Equation 2.13. Then the filter should be chosen to maximize Equation 2.15 subject to the constraint that Equation 2.13 be satisfied. The solution to that problem can be cast in the following form when  $S_{xx}(\omega)$  is monotonically decreasing for positive frequencies.<sup>23</sup>

$$(SNR)_u = \left\{ \frac{\omega^* S_{xx}(\omega^*)}{\pi} + 2 \int_{\omega^*}^{\infty} \frac{S_{xx}(\omega) d\omega}{2\pi} \right\}^{-1} \quad 3.22$$

where  $\omega^*$  is determined from the equation

$$\sigma_e^2 = \frac{N_{LW}}{P_r} \int_0^{\omega^*} \frac{d\omega}{2\pi} \ln \left[ \frac{S_{xx}(\omega)}{S_{xx}(\omega^*)} \right] \quad 3.23$$

We first consider the situation governed by Equations 3.20 and 3.21. Introducing Equation 3.3 into them and evaluating the integrals yields

$$(SNR)_u = \left\{ 2\sqrt{\frac{2}{\pi}} \frac{\Omega}{\omega^*} \left[ e^{-1/4(\omega^*/\Omega)^2} - e^{-1/2(\omega^*/\Omega)^2} \right] + 20\left(\frac{\omega^*}{\Omega}\right) \right\}^{-1} \quad 3.24$$

and

$$2 \frac{\omega^*}{\Omega} \left\{ -1 - \frac{1}{6}\left(\frac{\omega^*}{\Omega}\right)^2 + \exp 1/4\left(\frac{\omega^*}{\Omega}\right)^2 \right\} = \frac{P_r}{N_{LW}(\Omega)} d_r^2 \quad 3.25$$

where

$$U(y) \triangleq \int_y^{\infty} \frac{dX}{\sqrt{2\pi}} \exp -\frac{1}{2}X^2 \quad 3.26$$

For the situations of interest here, the signal to noise ratio is large which implies that  $\omega^*$  is large. Then Equations 3.24 and 3.25 become approximately

$$(SNR)u = \sqrt{\frac{\pi}{2}} \left( \frac{\omega^*}{2\Omega} \right) \exp \left( \frac{\omega^*}{2\Omega} \right)^2 \quad 3.27$$

and

$$\left( \frac{\omega^*}{2\Omega} \right) \exp \left( \frac{\omega^*}{2\Omega} \right)^2 = \frac{P_r}{N_s W} \left( \frac{d_r}{\Omega} \right)^2 \quad 3.28$$

Combining these two equations yields

$$(SNR)u = \sqrt{\frac{\pi}{2}} \frac{P_r}{N_s W} \left( \frac{d_r}{\Omega} \right)^2 \quad 3.29$$

For large values of the bandwidth constraint,  $d_r$ , the output signal to noise ratio is determined from Equations 3.22 and 3.23. When the expression of Equation 3.3 for the message spectra is introduced into Equation 3.22 one obtains

$$(SNR)u = \left\{ \sqrt{\frac{P_r}{\pi}} \frac{\omega^*}{\Omega} e^{-\frac{1}{2} \left( \frac{\omega^*}{\Omega} \right)^2} + 2Q \left( \frac{\omega^*}{\Omega} \right) \right\} \quad 3.30$$

which can be approximated by

$$(SNR)u = \sqrt{\frac{\pi}{2}} \frac{\exp \frac{1}{2} \left( \frac{\omega^*}{\Omega} \right)^2}{\left( \frac{\omega^*}{\Omega} \right) + \left( \frac{\Omega}{\omega^*} \right)} \quad 3.31$$

Introducing Equation 3.3 into Equation 3.23 yields the following expression which determines the value of  $\Omega^*$ .

$$\sigma_r^2 = \frac{1}{3} \frac{N_s W}{P_r} \left( \frac{\omega^*}{\Omega} \right)^2 \quad 3.32$$

These last two equations can be combined to obtain

$$(SNR)u = \sqrt{\frac{\pi}{2}} \frac{\exp \left( \frac{1}{2} Z^2 \right)}{Z + Z^{-1}} \quad 3.33a$$

where

$$Z = \left[ 3\sigma_r^2 \frac{P_r}{N_s W} \right]^{1/2} \quad 3.33b$$

The value of the constraint  $d_r$  for which the signal to noise

ratio changes from Equation 3.29 to 3.33 is determined by equating the two expressions and solving for  $d_r$ . The result is

$$\frac{d_r}{\sigma_c^2} = \left\{ \frac{3\sigma_c^2 \exp(1/2 Z^2)}{(Z^2 + 1)Z^2} \right\}^{1/2} \quad 3.34$$

#### 3.4 FIRST ORDER BUTTERWORTH SPECTRUM

The performance of FM, as well as OAM, will be determined for the first order Butterworth spectrum that is given by Equation 3.4 when  $n$  is set to one.

For that spectrum the signal to noise ratio of an FM system operation above threshold is, from Equations 2.11 and 2.14',

$$(\text{SNR})_u = \left\{ 1 + \frac{4}{\sqrt{2\pi}} \left( \frac{d_r}{\Omega} \right) \sqrt{\frac{P_r}{N_c W}} \right\}^{1/2} \approx \frac{8}{\pi} \frac{d_r^2}{\Omega} \frac{P_r}{N_c W} \quad 3.35$$

The right-most approximation in this expression is valid for the large signal to noise ratios that are of interest in this work.

Equation 3.35 is valid when the threshold condition of Equation 2.13 is satisfied. For the problem at hand that condition can be shown to be

$$\frac{\pi N_c W}{P_r} \left\{ -1 + \left[ 1 + 2 \sqrt{\frac{2}{\pi}} \left( \frac{d_r}{\Omega} \right) \sqrt{\frac{P_r}{N_c W}} \right] \right\} \leq \sigma_c^2 \quad 3.36$$

For large signal to noise ratios it is approximately given by

$$\left( \frac{d_r}{\Omega} \right)^{1/2} \left( \frac{2\pi N_c W}{P_r} \right)^{3/4} \approx \sigma_c^2 \quad 3.37$$

When the system is operating at the FM threshold, so that Equation 3.37 is satisfied with equality, the signal to noise ratio approximation of Equation 3.35 becomes

$$(\text{SNR})_u \approx \frac{\sigma_c^2}{\pi} \frac{P_r}{N_c W} \quad 3.38$$

The performance of the OAM system for the first order Butterworth message spectrum can be determined from Equations 3.20 through 3.23 which are valid when the message spectrum is monotone for positive frequencies.

When the bandwidth constraint of Equation 3.21, in fact, constraints the system performance the signal to noise ratio is given by Equation 3.20. For the first order Butterworth message spectrum those equations can be reduced to

$$(\text{SNR})_u = \frac{\pi}{2} \left\{ \frac{\Omega}{\omega*} - \frac{(\Omega/\omega*)}{\sqrt{1 + (\omega*/\Omega)^2}} + \frac{\pi}{2} - \tan^{-1} \frac{\omega*}{\Omega} \right\} \quad 3.39$$

and

$$\frac{2}{3} \left( \frac{\omega*}{\Omega} \right)^3 + \left( \frac{\omega*}{\Omega} \right) - \left( \frac{\omega*}{\Omega} \right) \sqrt{1 + \left( \frac{\omega*}{\Omega} \right)^2} = \frac{P_s}{N_c W} \left( \frac{d_r}{\Omega} \right)^2 \quad 3.40$$

If the signal to noise ratio is to be large,  $\omega*/\Omega$  must be large and Equations 3.39 and 3.40 can be approximated by

$$(\text{SNR})_u \approx \frac{\pi}{4} \frac{\omega*}{\Omega} \quad 3.41$$

and

$$\frac{2}{3} \left( \frac{\omega*}{\Omega} \right)^3 \approx \frac{P_s}{N_c W} \left( \frac{d_r}{\Omega} \right)^2 \quad 3.42$$

Combining these last two equations yields

$$(\text{SNR})_u \approx \frac{\pi}{4} \frac{3}{2} \left\{ \frac{P_s}{N_c W} \left( \frac{d_r}{\Omega} \right)^2 \right\}^{1/3} \quad 3.43$$

Equation 3.43 gives the signal to noise ratio of the OAM system when  $d_r$  is small enough that the bandwidth constraint rather than the threshold constraint is dominate.

When the threshold constraint is dominate the signal to noise ratio is determined by Equations 3.22 and 3.23. For the first order Butterworth message spectrum these equations can be reduced to

$$(\text{SNR})_u = \frac{\pi}{2} \left\{ \frac{(\omega*/\Omega)}{(\omega*/\Omega)^2 + 1} + \frac{\pi}{2} - \tan^{-1} \frac{\omega*}{\Omega} \right\} \quad 3.44$$

and

$$\frac{\omega*}{\Omega} - \tan^{-1} \frac{\omega*}{\Omega} = \sigma_s^2 \frac{P_s}{2N_c W} \quad 3.45$$

As before, if the signal to noise ratio is to be large  $\omega*/\Omega$  must be large. Then

$$(\text{SNR})_u \approx \frac{\pi}{4} \frac{\omega*}{\Omega} \quad 3.46$$

and

$$\frac{\omega*}{\Omega} \approx \sigma_s^2 \frac{P_s}{2N_c W} \quad 3.47$$

Combining these two expressions yields

$$(SNR)_u \approx \frac{\pi}{8} \sigma_c^2 \frac{P_s}{N_o W} \quad 3.48$$

A comparison of Equations 3.43 and 3.48 shows that they will be equal when

$$\frac{d_r}{\Omega} = \frac{\sigma_c^2}{\sqrt{12}} \frac{P_s}{N_o W} \quad 3.49$$

For values of  $d_r/\Omega$  less than this value the signal to noise ratio is given by Equation 3.43 and the OAM system is operating above threshold. For larger values the system is operating at threshold and the signal to noise ratio is given by Equation 3.48.

#### References

1. Kennedy, R.S., "Analysis of Secure Fiber Optic Systems," RADC-TR-81-91, March, 1982, Section 6.
2. Van Trees, H.L., Detection Estimation, and Modulation Theory, Part II, John Wiley and Sons, Inc., 1971, Section 4.3.
3. Van Trees, H.L., op. cit., Section 5.2.
4. Van Trees, H.L., op. cit., pp. 118-120.
5. Van Trees, H.L., op. cit., Section 5.1.
6. Van Trees, H.L., op. cit., Section 4.2.

J. Kierstead

## A. INTRODUCTION

The Air Force has a high interest in nonlinear optical materials and devices. Research at the Solid State Services Division is centered around the development of efficient, high speed nonlinear optical materials that operate at relatively low laser intensities. Both photorefractive and resonant nonlinear optical interactions are being studied. Resonant interactions are the most promising, but have been difficult to study in detail because of broadening mechanisms that are present in most materials; for example, crystal fields in solids, and collisions in vapors. To eliminate these complications the nonlinear optical properties of an atomic beam will be studied. This will enable a systematic investigation, both experimental and theoretical, of the physics of resonant nonlinear optical interactions. Such studies are ultimately expected to result in the development of greatly improved low power nonlinear optical materials and devices, which will have applications in optical computing and optical signal processing.

Consulting efforts during this reporting period were directed toward the design and fabrication of the atomic beams to be used in the nonlinear optical studies. These atomic beams must be compact enough to easily fit on an optical table, yet have good optical quality window, a long lifetime, and sufficient throughput to achieve over 50% absorption of a resonant laser beam.

## B. EXPERIMENTAL PROCEDURE

The basic atomic beam design is shown in Fig. 1. The interaction region consists of a section of steel waveguide with knife-edge vacuum flanges welded to both ends. Holes are drilled at various locations in the waveguide, as shown, to admit laser light and to facilitate fluorescence detection. To maintain a high vacuum, these holes are covered with windows of good optical quality, having anti-reflection coatings.

A key design consideration is the technique for mounting these windows in a stress free manner so that no birefringence will be introduced. Commercial vacuum windows have an unacceptable amount of stress induced birefringence. The technique chosen here is to mount the windows in a O-ring sandwich as shown in Fig. 2. This geometry ensures that no sheer forces are present. To simplify fabrication, O-ring grooves are not used. Rather, the waveguide surface is polished to remove visible scratches as shown in Fig. 3 and a thin aluminum bushing is inserted into the hole in the waveguide, Fig. 4(a), to provide support for the vacuum side O-ring.

The O-rings sandwich is compressed using pressure plates bolted to an aluminum superstructure, which in turn is clamped onto the waveguide, as shown in Fig. 4(b). The O-ring pressure plates are of two types as illustrated by the drawings for Fig. 5. Type A has a tapered hole which allows either wide angle laser illumination or wide angle fluorescence collection. Type B has a threaded hole and acts as a light baffle to reduce the amount of room light which enters the atomic beam apparatus. For experimental flexibility, each interaction region port is equipped with



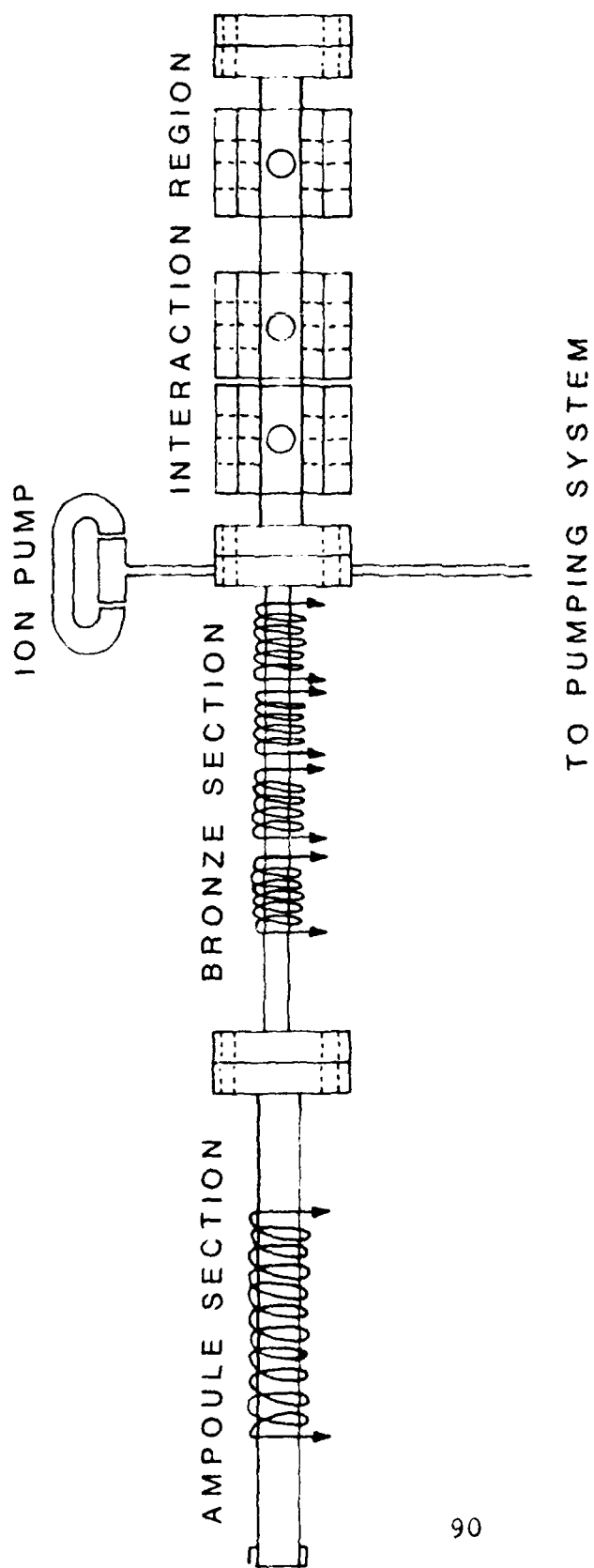


FIGURE 1. Complete atomic beam apparatus.

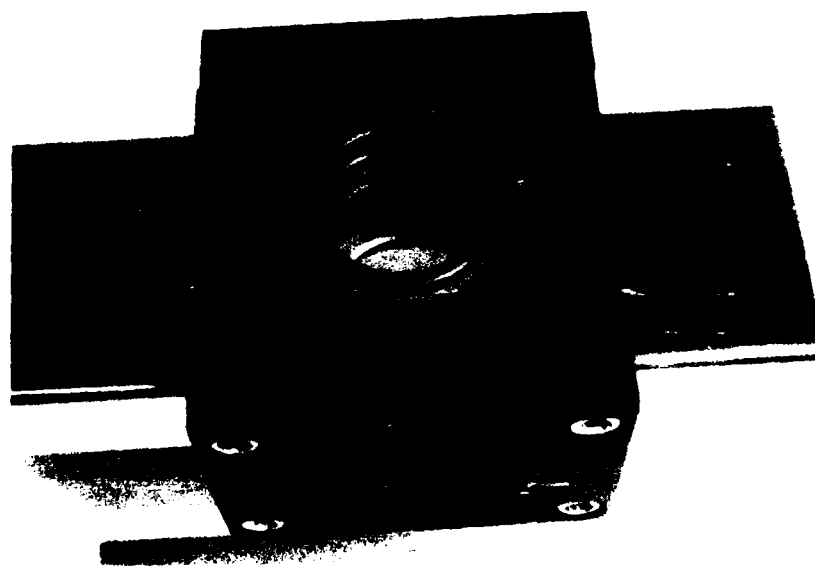
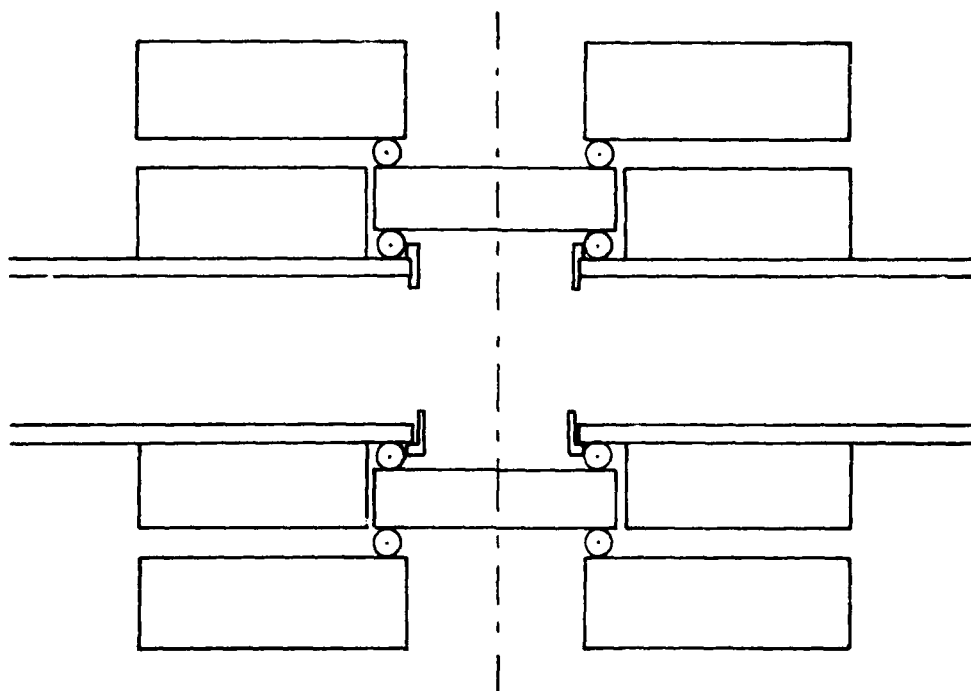


Fig. 2. (Top) Schematic drawing of O-ring Sandwich.  
(Bottom) Photo of O-ring sandwich.

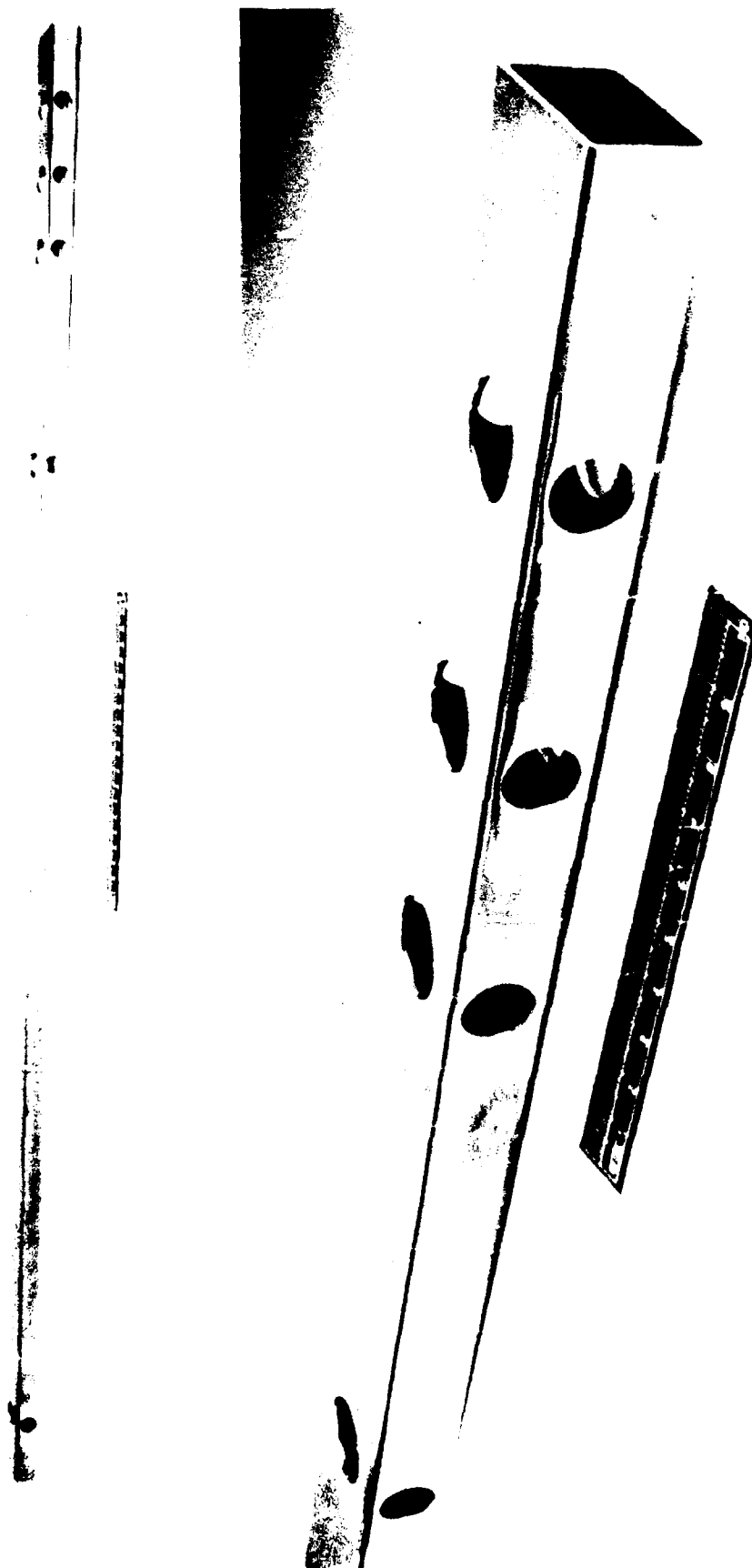
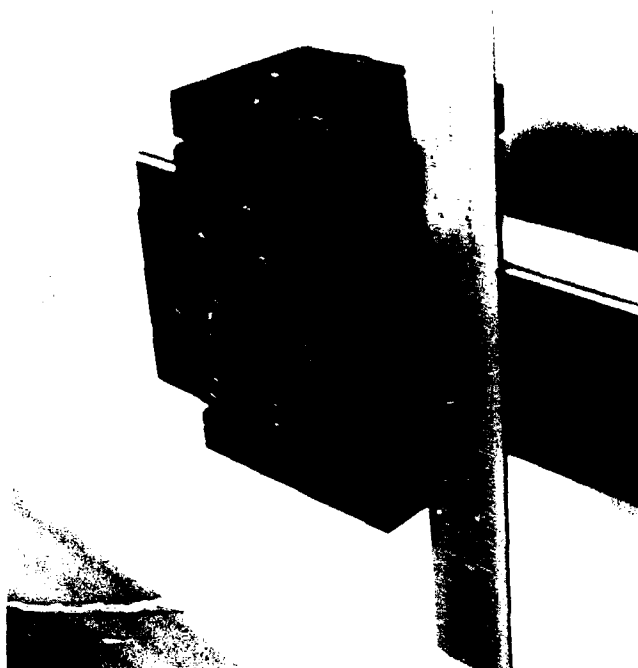


FIGURE 3. Photos showing polished waveguide surface near holes.

B



A



Fig. 4. (a) Photo showing vacuum side O-ring bushing (b) Photo showing completed window assembly including pressure plates.

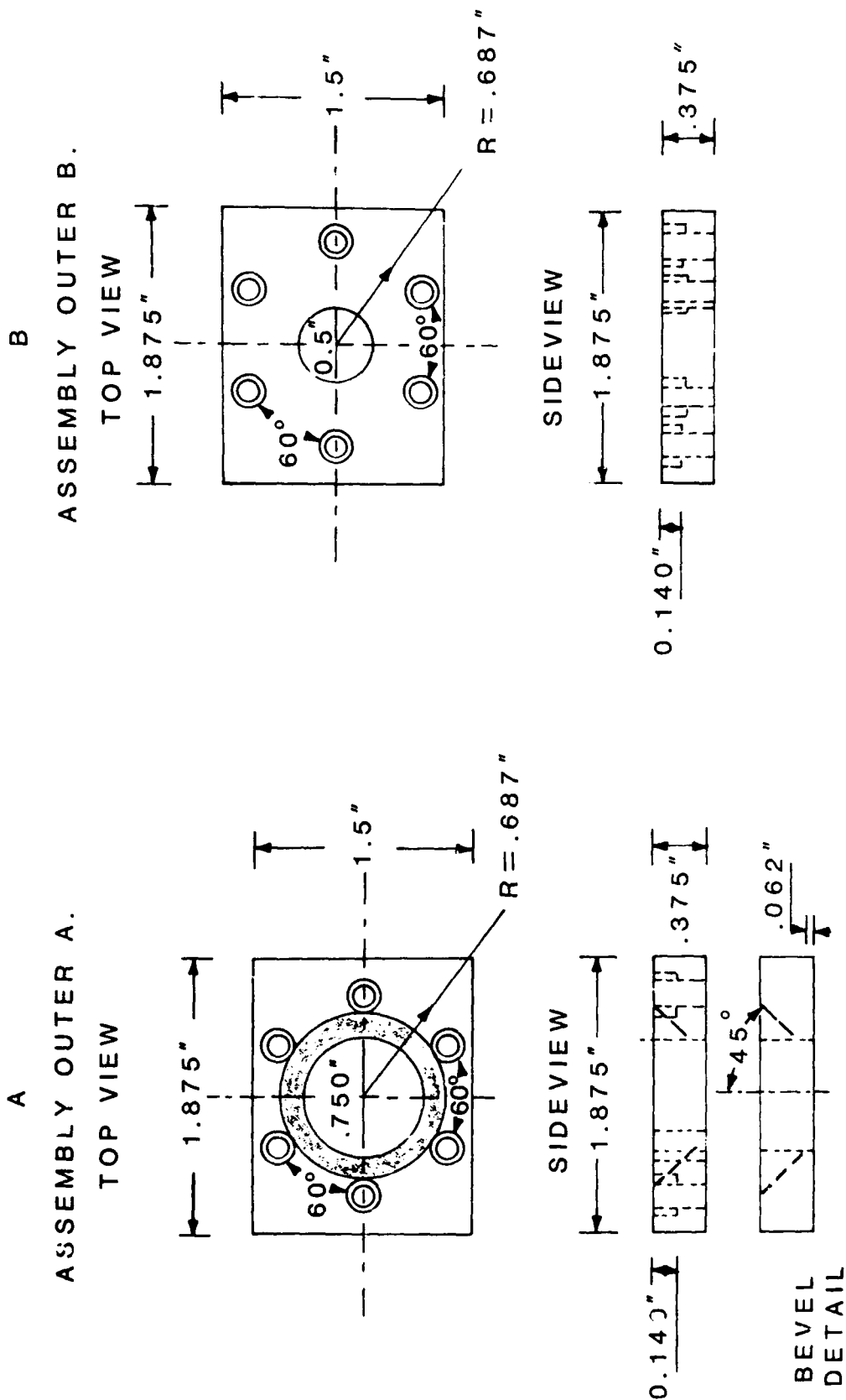


FIGURE 5. (a) Drawing of type A pressure plate.  
(b) Drawing of type B pressure plate.

both types of pressure plates. In preliminary experiments the laser beam was steered through the threaded plates and the fluorescence was collected using a sensitive detector mounted to one of the tapered plates. Finally, to reduce scattered light, all aluminum surfaces are black anodized.

To maintain a low background gas pressure during operation of the atomic beam, each interaction port is supplied with a separate graphite getter, as shown in Fig. 6. Without this getter the background gas generated by the atomic beam would lead to collisions and limit the usefulness of the apparatus for fundamental studies. As shown in the figure, the graphite getter has holes bored along all three axes. The size of the hole along the atomic beam axis determines its collimation, via geometry. The other holes are matched to the size of the holes in the waveguide.

The atomic beam source consists of a porous metal rod inserted in a stainless tube, shown in Fig. 1, which in turn is welded to a knife-edge vacuum flange. The porous metal rod is bored with a 2 mm dia. hole and serves as a recirculating heat pipe oven. In operation, the front section of the porous metal (nearest the interaction region) is kept just above the melting point of the atomic beam material, while the rear section is heated to a high temperature. Material not travelling along the axis of the porous metal sticks to the cold section and is returned to the hot end by capillary action. This recirculating oven design permits both a high throughput with a low source consumption. So far, two materials have been used : sodium and cesium. These materials were chosen because of their

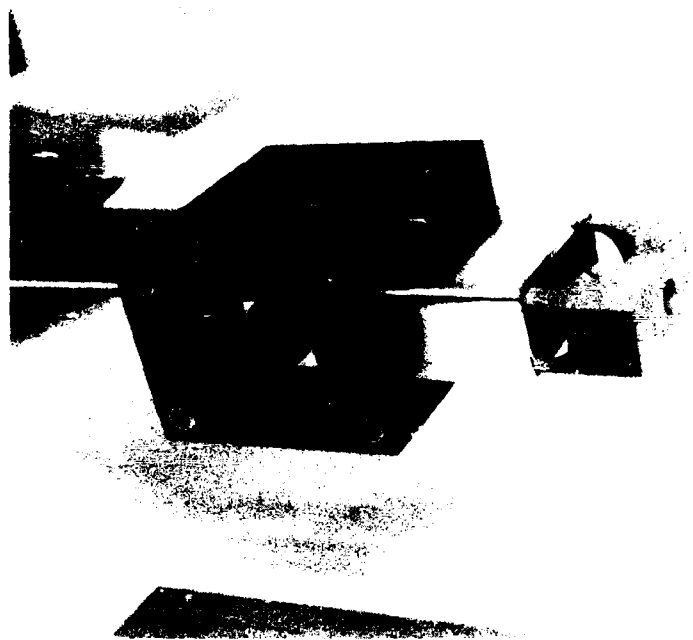


Fig. 6. Photo showing graphite getter

large resonant optical absorption and relative ease of handling.

### C. ASSEMBLY PROCEDURE

Several of the components of the atomic beam must be pre-baked under vacuum to remove contaminants. In particular, the porous metal must be baked at a temperature of 700 °C in the case of the porous bronze or 1100 °C for porous stainless. Porous bronze is the preferred material for use with Cs because its lower pre-bake temperature and better malleability simplifies oven assembly. Porous stainless, however, must be used for Na because of its ability to withstand the higher operating temperatures required. In addition to the porous metal, the anodized O-ring bushings are pre-baked to 400 °C and the graphite is pre-baked by the manufacturer to about 600 °C.

The interaction region and oven sections are first assembled separately and are then bolted together using the knife-edge vacuum flanges, where a double sided flange is also sandwiched in between, as shown in Fig. 1. This double sided flange has two pumping ports: one consisting of an ion pump and the other of either a valve or copper pinch tube, which can be connected to a larger capacity vacuum system during bake out. To complete the assembly, an ampoule section is bolted to the rear of the porous metal oven. This section contains a commercially available Na or Cs ampoule.

The complete atomic beam assembly is given a final baked out at 300 °C to remove surface moisture. After cooling to room temperature the ampoule is then broken its contents are driven over to the porous metal by heating.



#### D. RESULTS

A cesium beam and a sodium beam have been fabricated so far. The sodium beam has 5 ports in the interaction region with a total interaction length of 1 meter. An ultimate pressure of  $2 \times 10^{-6}$  was achieved, which translates into a mean free path of greater than 10 meters. Measurements made so far with a dye laser verify the absence of collisions out to about 30 cm from the oven. This Na beam can be operated at a maximum temperature of 450 degrees. At higher temperatures, a contaminant in the porous stainless steel causes an increase in background gas pressure. This contaminant could have been removed by baking at 1100 °C, but was not discovered until after this oven was assembled.

The cesium beam is more compact, having a total length of 20 cm and an ultimate pressure of  $5 \times 10^{-7}$ . Measurements made with a semiconductor laser verify the absence of collisions over the full 20 cm length. Detailed throughput vs. temperature measurements have not yet been made because of problems with the semiconductor lasers used to excite this atomic beam.

At present, the residual background pressure results from permeability and outgassing of the (Viton) O-rings. Current plans are to test Viton O-rings of square cross section and to test silver plated stainless O-rings. Kalrez O-rings have also been tried but were found to leak after bake out.

## E. CONCLUSIONS

Preliminary tests have been successful. The atomic beam is compact, has good optical quality windows and a large mean free path during operation. Throughput is not achieved it may be necessary to employ a supersonic oven design. Once sufficient throughput has been achieved to demonstrate greater than 50% absorption, nonlinear optical studies can begin.

**OPTICAL SIGNAL PROCESSING**  
**IN**  
**NONLINEAR POLYMERS**  
**AND OTHER MATERIALS**

**ANNUAL REPORT**

By:

Michael M. Salour

## I. INTRODUCTION

In recent years there has been a renewed interest in optical signal processing devices and optical computing. In this report the requirements of nonlinear optical materials are discussed and fundamental limits are derived. Of particular interest are a new class of materials based on nonlinear optical effects in polymers. These materials show large optical nonlinearity, have a very fast response time, and have the potential for low cost mass produced integrated optical devices. Finally, in this report the application of nonlinear four wave mixing in nonlinear polymers to optical logic and switching is investigated.

## II. ELECTRONIC PROCESSING

Until recently the development of computers has been dominated by serial processing. With this method arithmetic and logic functions are performed in a central processing unit (CPU) and programs are stored in a separate memory (random-access memory; RAM). These machines thus evaluate a problem sequentially. A difficulty with such a design is that the communication channel between the CPU and RAM limits the computer speed. This is often called the Von Neumann bottleneck. To eliminate the bottleneck, researchers are now developing parallel processing, so that several operations are carried out simultaneously rather than sequentially. Current supercomputers all incorporate some degree of parallelism -- typically fewer than 100 parallel channels although Thinking Machines has demonstrated 64,000 channels. Current supercomputers offer bit rates of  $\sim 10^{10}$  bits per second and future machines with up to  $10^{12}$  bits per second seem feasible. The next generation of machines will require considerable rethinking of conventional computer architectures, and there is an increasing trend to optimize machines for specific application rather than for general-purpose computing.

Electronic solutions to increased speed face fundamental limitations. This transfer time limit in a computer system can have serious consequences as clock cycle times and pulse widths shrink. The signals from different parts of the system can arrive at a gate at different times (clock skew). In most

computer systems the usual approach is to wait for inputs to settle before using the output of a gate. The settling time is normally RC time constant dominated, yet VLSI technology does not solve this problem. As the length of a wire shrinks by a factor of  $X$  and the cross section is reduced by  $X^2$ , the capacitance of the wire decreases by a factor of  $X$ , but the resistance increases by a factor of  $X$ . The RC time constant remains constant and the input charging time remains the same, independent of scaling.

In future generations of machines, optical processing will likely play a role. The potential of optics for information processing and memory has been realized for many years.<sup>1</sup> For example, a diffraction-limited optical image can contain  $\sim 10^8$  bits of information per square centimeter. Large amounts of information can be processed simultaneously in relatively small volumes, free of interference from other electromagnetic waves. In addition, wireless interconnection with non-interfering beams greatly facilitates the design of interconnections between submodules. Certain functions can be performed with simple linear optics, for instance, performing a Fourier transform with a lens. However, for any more general processing function with switches and digital design one requires an optical nonlinearity.

### III. NONLINEAR INTERACTIONS OF LIGHT

In all-optical processing one light beam or pulse is used to control a second signal beam or pulse. Since, photons do not directly interact with each other, an optical medium is required in which an optical property, such as the refractive index  $n$  or absorption coefficient  $\alpha$ , is changed by the propagation of a light beam in the medium. A nonlinear refractive index  $n_2$  can be defined by

$$n = n_1 + n_2 I \quad (1)$$

and a nonlinear absorption coefficient  $\alpha_2$  by

$$\alpha = \alpha_1 + \alpha_2 I \quad (2)$$

Here  $n_1$  is the linear index of refraction,  $\alpha_1$  the linear absorption coefficient and  $I$  the beam irradiance. In such a medium, the presence of one light beam affects the propagation of a second light beam. For example the optical absorption changes by an amount  $\Delta\alpha = \alpha_2 I$  in the presence of light of intensity  $I$ , and the intensity of the transmitted beam varies. Also, for a change of refractive index  $\Delta n = n_2 I$ , the phase of the transmitted signal varies. A phase change can be converted to an intensity change by using polarizers, by holographic techniques, or by placing the medium within a Fabry-Perot or Mach Zehnder interferometer. Most of the research to date has made primary use of the nonlinear index  $n_2$  rather than  $\alpha_2$ . However, recent work with the nonlinear absorption in quantum well semiconductor structures has demonstrated optical switching.

One should emphasize that the nonlinear index or absorption alone is not the most useful characteristic of a material for optical processing. A useful basis for comparison of different materials is the optical energy required to process a bit of information. This quantity depends not only on  $n_2$  but also on the wavelength of light in the medium and the response time of the medium, that is, the rate at which the index changes in response to the incoming radiation.

#### IV. OPTICAL SWITCHING

Considerable prejudice has developed against the use of optics for computing because of the following problems and alternate available technology.

- 1) The rapid growth of electronic digital integrated circuit technology.
- 2) The minimum size of an optical switching element is  $(\lambda/n)^3$ , where  $\lambda$  is the wavelength of light.
- 3) The photon energy  $h\nu$  is much larger than the thermal energy  $kT$ .
- 4) Optical nonlinearities are typically small.
- 5) Proposed optical switches have often been two terminal devices.

These basic problems imply large switching volumes with accordingly long propagation delay times between switching elements, and high heat dissipation. Detailed evaluations of these limitations have been made by researchers at IBM.<sup>1</sup> Additional limitations on switching are also discussed in Section VII of this report.

These basic problems have not, of course, changed. However, there have been several developments of importance which have stimulated a new look at the role of optics in information processing.

- 1) New materials such as nonlinear polymers and new nonlinear mechanisms have been discovered which have larger optical nonlinearities.
- 2) Mode-locked lasers are now readily available which deliver optical pulses of a few femtoseconds duration. These short, intense pulses should permit subpicosecond switching operations.
- 3) Fiber optics and integrated optics are available which permit the transmission and switching of very high bandwidth ( $>>10^{10}$  Hz) information channels.
- 4) The limitations of serial electronic processing have been realized.

Consequently, a near-term goal of optical processing is to use the capabilities of optics that are not readily achieved with electronics. This is particularly pertinent for both image processing and fiber-optic communications, where the information is already being carried on optical beams. To achieve this goal, the development of appropriate materials is essential. The important material parameters for all applications are:

- 1) Cost and ease of crystal growth.
- 2) The magnitude of the nonlinearity and the energy required to change  $\alpha$  or  $n$  by the required amount

- 3) The material response time -- that is, the speed with which  $n$  or  $\alpha$  can be changed.
- 4) The optical quality of the material and its resistance to optical damage.

## V. MATERIAL RESPONSE TIME

For serial processing, the main potential advantage of optics is ultrahigh speed. Since femtosecond optical pulses are available, it is desirable to have materials which respond on a subpicosecond time scale. The peak intensity of such an optical pulse can be very high even though the pulse energy is low. To avoid excessive transit time delays, such processing can be done in a pipeline mode, that is, with several optical pulses propagating in a transmission line simultaneously. A serial processor capable of processing  $10^{12}$  bits per second would appear to be a reasonable goal, in view of the potential of competing electronic technology. The only nonlinear mechanism that is known to respond on a picosecond or shorter time scale is the nonresonant electronic Kerr effect. This effect arises in transparent materials because of the nonlinear polarizability of a material due to the instantaneous action of the electric field of the light on its valence electrons. Nonresonant electronic Kerr nonlinearities are very usually weak, and high optical intensities are required to produce a significant index change. In addition to electronic effects, nonresonant Kerr effects can also be observed in transparent liquids containing anisotropic molecules that are partially aligned in the optical field, however the response time of the medium is increased typically to  $10^{-10}$  to  $10^{-12}$  second because of the time required to reorient the molecules. It is feasible that materials having resonant nonlinear optical effects which involve optical absorption may be developed with picosecond response times and much larger nonlinearities, but these have not yet been demonstrated. Resonant nonlinearities are discussed in the next section.

The response time requirement of materials can be greatly relaxed if one turns to parallel processing. For the same throughput of a processor, the required material response time is increased by the number of parallel channels, that is,



Maximum bit rate = (number of parallel channels) x (material response time)

For diffraction-limited optics with  $\sim 10^8$  bit/cm<sup>2</sup> a simple argument suggests that a material response time of  $\sim 10^{-4}$  second would be adequate for a rate of  $10^{12}$  bits per second with a 1-cm<sup>2</sup> nonlinear element. Long response times may even perform some memory functions. A much broader range of materials are available for optical processing on longer time scales. All of these effects involve absorption of the incident light:

- 1) The resonant Kerr effect with  $10^{-12} < \tau < 10^{-3}$  second,
- 2) The photorefractive effect with  $10^{-10} < \tau < 10^{+8}$  seconds, and
- 3) Electroabsorption with  $10^{-10} < \tau < 10^{-4}$  second,

where  $\tau$  is the material response time. These ranges are estimates based on currently available information. In the following sections, these various mechanisms for nonlinear index and absorption changes are discussed in more detail. The use of resonant effects may, however, produce undesired complications such as temperature or wavelength sensitivity.

## VI. MAGNITUDE OF NONLINEARITY

### A. Introduction

Since the change of refractive index  $\Delta n$  or absorption  $\Delta \alpha$  is proportional to the intensity of the input beam, the smaller the area corresponding to a single bit, the less optical energy is required for a switching operation. But there is a penalty for decreasing the focal spot size. This penalty is due to diffraction as shown in Figure 1. The confocal parameter (the effective interaction length  $L$  of the beam in the material) decreases in proportion to the area of the focal spot, that is,

$$L = \frac{\pi D^2}{2\lambda} \quad (3)$$

where  $D$  is the diameter of the beam waist at the focus and  $\lambda$  is the wavelength of light. For a  $1 \mu\text{m}^2$  spot size and  $n = 1$ , the interaction length is only  $3 \mu\text{m}$ . This distance is too short to achieve a significant phase change  $\phi (= \pi \Delta n L / \lambda)$  for most situations.

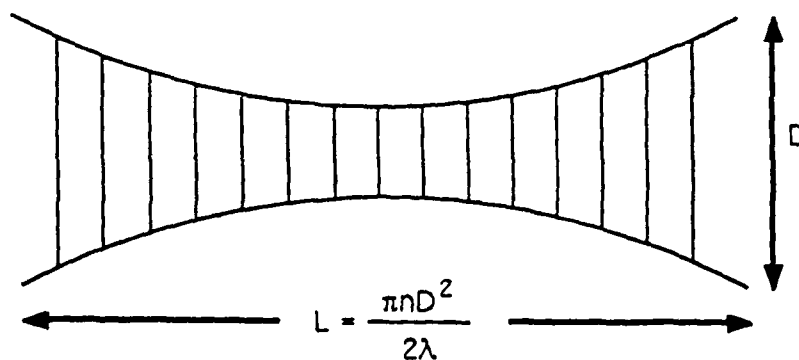


Figure 1. Cross Section of A Focused Optical Beam Showing the Effect of Diffraction

For  $\phi \sim \pi$  the required index change is  $\Delta n \sim 0.3$ . Therefore, either the focal spot must be increased with correspondingly increased energy requirements, or a guided wave structure (for serial processors) or holographic techniques (for parallel processors) which overcome the effects of diffraction must be used. With the latter techniques, phase changes of  $\pi$  are achievable with  $\sim 1\text{-}\mu\text{m}^2$  bit cross sections and long interaction lengths.

As mentioned above, a useful parameter for comparing the magnitude of the nonlinearity of materials is the energy required to switch or process a bit of information. For changes of refractive index, the transmission (neglecting reflection losses) of a material between crossed polarizers is

$$T = e^{-\alpha d \sin^2 \phi} \quad (4)$$

or the diffraction efficiency of a thick phase hologram is

$$\eta_p = e^{-\alpha d \sin^2 \phi / 2} \quad (5)$$

where  $\alpha$  is the optical absorption coefficient and  $d$  is the optical path length in the material. Thus, a phase change of  $\phi = \pi$  gives maximum contrast for the processing operation, that is, the change of diffracted power between the control beam on and off ( $\phi = \pi/2$  for maximum transmission in Equation 4). Values of  $\phi \ll \pi$  can be tolerated in many situations, the minimum value being determined by the tolerable signal-to-noise level, which is directly related to the bit error rate.

For the mechanisms involving nonlinear refraction, it is possible to make some general estimates of the minimum energy required for a phase change of  $\pi$  for each class of nonlinearity.

The switching relation is

$$\Delta \phi = \frac{2\pi n_2 I L}{\lambda} \quad (6)$$

Therefore

$$I = \frac{\lambda}{2 n_2 \ell} \quad (7)$$

$\lambda$  = wavelength  
 $n_2$  = nonlinear index  
 $I$  = optical power/area  
 $\ell$  = thickness of device.

The energy is

$$\epsilon = I \lambda^2 \tau_{\text{eff}} \quad (8)$$

$\tau_{\text{eff}}$  = effective time

#### B. Nonresonant Kerr Effect and Nonlinear Polymers

The electronic Kerr effect is the fastest of all mechanisms for optical processing. Because of the high speed, it responds to the instantaneous intensity of an optical pulse. It is now well established, both theoretically and experimentally, that the nonlinear index  $n_2$  is proportional to the density of bonds in the material and the orientation of the bonds with respect to the optical field, and depends critically on the degree of delocalization of electrons in the bond. Materials with the highest known values of  $n_2$  are highly conjugated long-chain molecules such as polymerized diacetylenes whose monomers have alternating single and triple bonds:  $R-C\equiv C-C\equiv C-R$ , where  $R$  is an organic functional group.<sup>2</sup> These solids have semiconductor character in the direction of the polymer chains and insulator character perpendicular to it. The components of the nonlinear polarizability of the polymer are some three orders of magnitude larger than those of the monomers. A limit to the degree of delocalization of the electrons is dictated by the required optical transparency of the material. The electronic absorption edge  $E_g$  shifts to longer wavelengths with increasing delocalization, that is,  $n_2 \propto E_g^{-6}$ . The nonlinear polymer polydiacetylene PTS [bis(p-toluene sulfonate)] probably represents the limiting case for operation at infrared wavelengths near  $1.0\mu\text{m}$ .<sup>3</sup> Another polymer with large optical nonlinearity is trans-polyacetylene. Table 1 shows the nonlinear index of this solid is large compared with that of

inorganic solids such as  $\text{SiO}_2$  and  $\text{LiNbO}_3$ . Nitroanilines, which more readily grow in single crystal form, may be useful for some applications. Also listed in Table 1 are examples of semiconducting materials which have larger nonlinear refractive indices at wavelengths in the infrared within the band gap of the material. In n-type InSb the nonlinearity is a free-electron effect due to the nonparabolicity of the conduction band. In GaAs, the effect is due to bound electrons. It is seen in Table 1 that InSb has a particularly large nonlinear index  $n_2$  at a wavelength of  $10 \mu\text{m}$ . However, the diffraction-limited bit size at  $10 \mu\text{m}$  is some 50 times larger than at  $1.3 \mu\text{m}$ , so that PTS requires less power per bit for processing than InSb. Another factor is that detectors are less sensitive at the longer wavelength.

These materials all show very fast nonlinearities  $\sim 10^{-14}$  sec. In contrast to the electronic Kerr effect, the molecular rotation Kerr effect depends on the orientation of molecules in the electric field of the light. It is unlikely that optical switching devices will be based on the molecular rotation effect. However, for comparison, the nonlinear index  $n_2$  of  $\text{CS}_2$  is listed in Table 1. Carbon disulfide has one of the largest values of  $n_2$  in the visible spectrum using molecular rotation.

TABLE 1. Nonresonant Nonlinearity  $n_2$  at Specific Wavelengths

Material	$\lambda$ ( $\mu\text{m}$ )	$n_2$ ( $\times 10^{14} \text{ m}^2/\text{W}$ )
$\text{CS}_2$	0.69	8
PTS	1.32	1000
2-Methyl-4-nitroaniline	1.32	170
GaAs	10	100
InSb	10	5000
Silica	1.0	0.06
$\text{LiNbO}_3$	1.0	$\sim 2.5$

### C. Resonant Nonlinearities

The nonresonant effects such as in typical nonlinear polymers depend on the response of a transparent material to the electric field of the light beam. As the frequency of light approaches an electronic resonance, some of the optical power is absorbed by the medium, causing a redistribution of the population among the energy levels. As a result, the dispersion associated with the absorption line is changed, giving rise to an intensity-dependent index of refraction. For light beams of constant intensity  $I$ , a nonlinear index  $n_2$  can still be defined according to Equation 1. However, the change of refractive index persists for the duration of the electron in the excited state. Thus, for a resonant nonlinearity the change of refractive index is integrated over the excited state lifetime  $\tau$ . If the optical pulse length  $\tau_p$  is short compared with  $\tau$ , then the change of refractive index  $\Delta n$  depends on the absorbed energy density  $\alpha I \tau_p / h\nu$  and not the instantaneous intensity  $I$ .

Because of the integrating effect of the excited state, resonant nonlinearities become energetically more favorable than nonresonant effects for longer pulses and lower intensities. The largest effects are achieved for very sharp absorption lines having a high oscillator strength such as those found in alkali vapors or at exciton absorption lines in semiconductors. Several examples are given in Table 2.

TABLE 2. Resonant Nonlinearities

Material	$\lambda$ ( $\mu\text{m}$ )	$n_2$ ( $\text{cm}^2/\text{W}$ )	$\tau$ (sec)
CdS exciton	0.49	$1.6 \times 10^{-6}$	$2 \times 10^{-9}$
InSb	5.3	$6 \times 10^{-5}$	$3 \times 10^{-7}$
GaAs (300K)	0.88	$2 \times 10^{-5}$	$2 \times 10^{-8}$
GaAs (MQW)	0.85	$4 \times 10^{-3}$	$3 \times 10^{-8}$

The closer the optical frequency is to the optical absorption, the greater is the change of refractive index for a given incident intensity. However, maximum crystal length is limited by the absorption length, and it is necessary to move away from the center of the absorption line to achieve sufficiently large phase shifts. For example, excitons provide a very high density of oscillators since excitons can be created up to a density comparable to the inverse cube of the exciton diameter. Generally, exciton absorption lines are well defined only at low temperatures. However, thin GaAs-GaAlAs multilayer heterostructures (multiple quantum wells) exhibit sharp exciton absorption lines even at room temperature. This is due to the increased confinement and binding energy of the exciton within the thin layer structure. When light at a wavelength just below the exciton peak was used an extremely large nonlinear index  $n_2$  was observed.

For device applications there are problems with resonant effects. The nonlinear behavior of such materials varies rapidly with optical wavelength because of the sharpness of the absorption peak. Thus, it is essential that both the optical wavelength, and the temperature of the materials be precisely controlled.

#### **D. Photorefractive Effect**

The photorefractive effect depends on the absorption of light in electro-optic crystals, but in this case the absorption bands are typically very broad and wavelength is non-critical. The effect is based on photoexcitation of free carriers, which then diffuse or drift in an externally applied electric field away from the light beam to trapping sites. The resulting redistribution of charge gives rise to space charge fields within the crystal in the illuminated regions. The space charge fields give rise to refractive index changes, through the electro-optic effect, which replicate the incident intensity. The induced index change  $\Delta n$  persists for the duration of the space charge field, which can vary from subnanosecond time scale in semiconductors to years in insulators. The photorefractive effect can produce nonlinear index changes  $\Delta n$  comparable to Kerr effects because the optically induced index change is not just a local (atomic scale) change in polarizability but is due to the displacement of

electrons and holes over a distance of micrometers. This large photoinduced dipole gives rise to an amplification of the index change. A photorefractive material can be viewed as having a built-in optical detector that generates an electric field.

The photorefractive effect was originally discovered<sup>5</sup> in  $\text{LiNbO}_3$  and soon after was found to be generally present in other electro-optic crystals. The largest nonlinear index changes are observed in materials such as ferroelectric  $\text{BaTiO}_3$  and  $\text{Sr}_{1-x}\text{Ba}_x\text{Nb}_2\text{O}_5$  (SBN), that have extremely large electro-optic coefficients  $r_{ij}$ , but the nature of the absorbing centers and traps in these materials is not known. However, it has been shown<sup>6</sup> that the index change per absorbed photon, which is important for optical processing, depends primarily on the photocarrier drift or diffusion length and the ratio  $n_i^3 r_{ij}/\epsilon_j$ , where  $\epsilon_j$  is the dielectric constant. This ratio is comparable in  $\text{Bi}_{12}\text{SiO}_{20}$ , InP, GaAs, CdTe  $\text{BaTiO}_3$  and SBN. The values of  $n_i^3 r_{ij}$  and  $n_i^3 r_{ij}/\epsilon_j$  for several photorefractive materials are shown in Table 3.

TABLE 3. Photorefractive Materials and Properties

Material	Useful wavelength range	Drift length ( $\mu\text{m}$ )	Relaxation Time		
			$\tau_d$ (sec)	$n_i^3 r_{ij}$ (pm/V)	$n_i^3 r_{ij}/\epsilon_j$ (pm/V)
InP	0.85–1.3	3	$10^{-4}$	52	4.1
GaAs	0.8–1.8	3	$10^{-4}$	43	3.3
$\text{LiNbO}_3$	0.4–0.7	$\leq 10^{-4}$	300	320	11
$\text{Bi}_{12}\text{SiO}_{20}$	0.4–0.7	3	$10^5$	82	1.8
$\text{Sr}_{0.6}\text{Ba}_{0.4}\text{Nb}_2\text{O}_6$	0.4–0.6		$10^2$	2,460	4.0
$\text{BaTiO}_3$	0.4–0.9	0.1	$10^2$	11,300	4.9
$\text{KNbO}_3$	0.4–0.7	0.3	$10^{-3}$	690	14

The relaxation time  $\tau_d$  depends only on the dielectric relaxation time of the material; in GaAs and InP this has been varied from the millisecond region to the microsecond region by varying the electronic conductivity. In insulators,



the relaxation time is considerably longer. The minimum energy per bit for processing via the photorefractive effect is approximately 1 pJ for a  $1\text{-}\mu\text{m}^2$  bit size. This is comparable to the resonant nonlinear index in GaAs multilayer structures.

Another property of the photorefractive effect that is unique among all mechanisms for nonlinear index change is the spatial phase shift between the incident intensity pattern and the induced index which depends on the direction of displacement of the photocarriers. In a holographic two-beam mixing experiment, as exhibited in Figure 2, this gives rise to transfer of energy from one beam to the other. A weak image beam can, in this way, be amplified by mixing it with an intense pump beam (carrying no information). Amplification factors of up to 100 have been achieved.<sup>7</sup> The photorefractive effect thus offers considerable versatility for processing information, particularly since the wavelength of operation is non-critical and beams of one wavelength can be used to control several other wavelengths. The effect has been used both for holographic processing as shown in Figure 2, where the transverse electro-optic effect is employed, and for real image processing as shown in Figure 3, where the longitudinal electro-optic effect is used. In the latter case, the minimum bit size is approximately equal to the thickness of the material. In the holographic case, the resolution is determined by the spatial frequency of the hologram. The minimum energy requirements for each mechanism for phase change of  $\pi$  are summarized in Table 4.

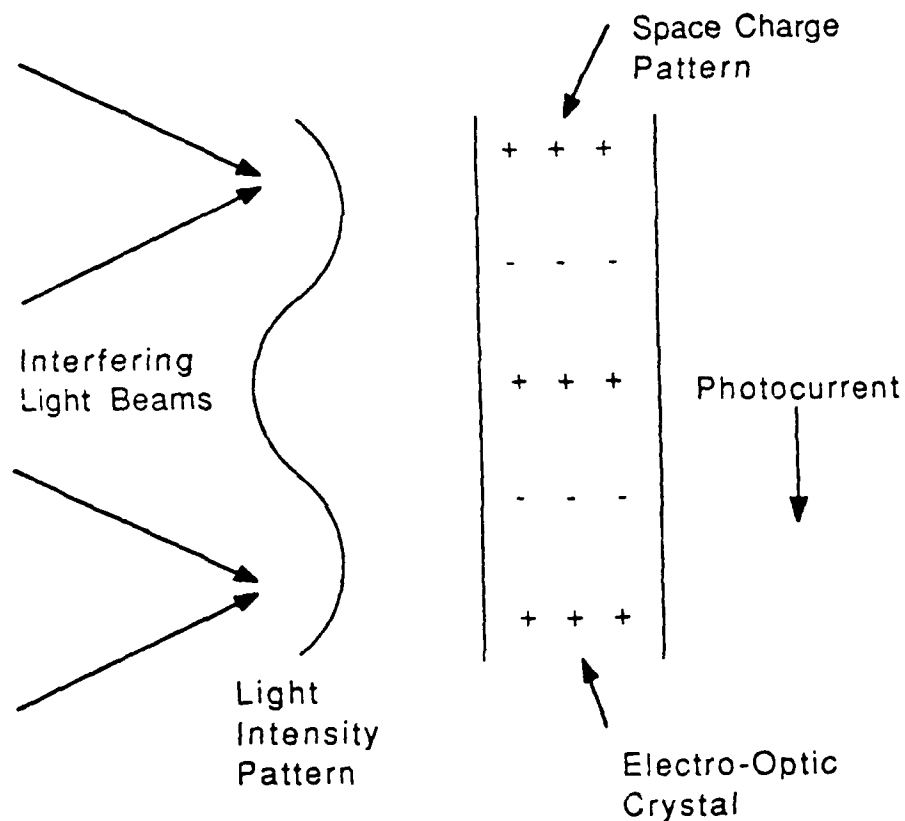


Figure 2. Two-Wave Mixing For Holographic Processing, Using the Photorefractive Effect

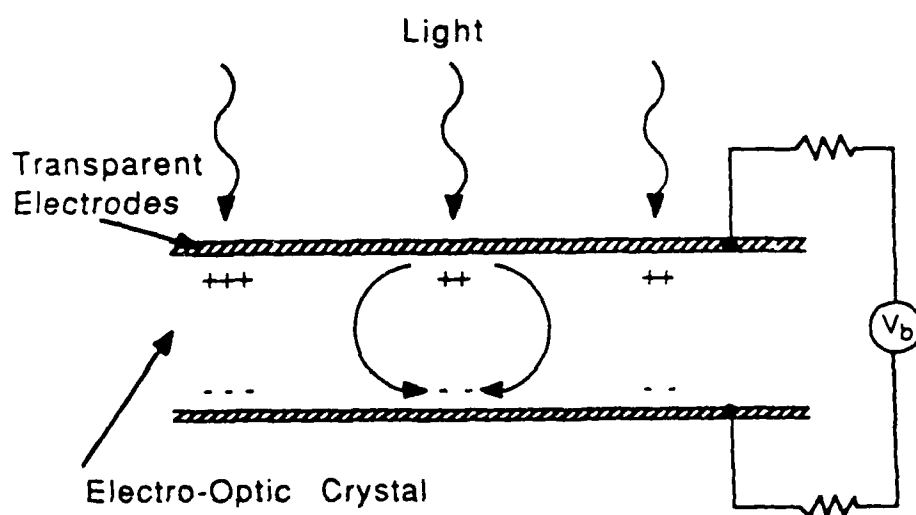


Figure 3. Image Storage Due To Charge Transfer In An Electro-Optic Material

**Table 4. Minimum Energy Per Bit For A Phase Change Of  $\pi$  Estimated For Each Of The Nonlinear Mechanisms.**

Material	Nonlinear Mechanism	$\lambda$ ( $\mu\text{m}$ )	$\tau$ (sec)	Energy (pJ/bit)
PTS	Nonresonant Kerr	1.3	$10^{-14}$	$0.2\tau_p \times 10^{12}$
GaAs (MQW)	Resonant Kerr	0.85	$2 \times 10^{-8}$	1
InSb	Resonant Kerr	5.3	$3 \times 10^{-7}$	10
Bi <sub>12</sub> SiO <sub>20</sub>	Photorefractive	0.6	$10^5$ (dark)	1
InP	Photorefractive	0.85-1.3	$10^{-4}$ - $10^{-6}$	1

This table clearly shows the advantages of the nonlinear polymers for picosecond pulse durations.

#### **E. Electroabsorption**

Another switching mechanism is the use of electroabsorption to produce a nonlinear absorption change in GaAs multilayer heterostructures.<sup>8</sup> As with the photorefractive effect, the effect used is hybrid; photocarriers resulting from optical absorption change the electric field inside the material and stark shift the exciton line. The PIN device is typically biased through a series resistor. Photocurrent resulting from optical absorption gives a voltage drop across the resistor, and changing the optical absorption. The results demonstrate that switching can be achieved with only  $4 \text{ fJ}/\mu\text{m}^2$  of optical energy, and an additional  $16 \text{ fJ}/\mu\text{m}^2$  of electrical energy from the bias circuit.<sup>9</sup> It is likely that a bit size of a few square micrometers is achievable. These devices will allow for parallel arrays but are RC time constant limited in response time. The device is also very wavelength sensitive.

### **VII. FUNDAMENTAL LIMITS ON OPTICAL SWITCHING AND SIGNAL PROCESSING**

For switching processes, in general, one can calculate the fundamental

switching energies that are needed for switching and the limitations on these energies.

### A. Quantum Limits

Quantum mechanics dictates that the energy-time uncertainty relation be observed for any switching operation. Thus,

$$\Delta E_{s,q} > \hbar/\tau$$

where  $\Delta E_{s,q}$  = quantum limited switching energy  
 $\hbar$  = Planck's constant/ $2\pi$  =  $1.05 \times 10^{-34}$  J-s  
 $\tau$  = switching time

The switching power per bit is limited by  $P_{s,q} = \Delta E_{s,q}/\tau = \hbar/\tau^2$ . Here the maximum switching rate is approximately  $1/\tau$ , and we are neglecting factors of the order of unity that depend on the specific pulse shape.

For a switching time of  $10^{-12}$ s the switching energy must exceed  $1 \times 10^{-22}$  J. If the switching rate is limited by  $1/\tau$ , the switching power is greater than  $1 \times 10^{-10}$  W for  $\tau = 10^{-12}$ s.

### B. Thermal Limits

Since any irreversible switch must operate at finite temperatures, then the switching energy must be greater than the characteristic thermal energy. Thus

$$\begin{aligned} \Delta E_{s,t} &> kT \\ &= 4.1 \times 10^{-21} \text{ J (at 300 K)} \end{aligned}$$

where  $k$  is Boltzmann's constant. The corresponding switching power per bit is limited by

$$P_{s,t} = \Delta E_{s,t}/\tau.$$

At  $\tau = 10^{-12}$  s the switching power per bit must exceed  $4 \times 10^{-9}$  W at a temperature of 300 K.

Because the quantum limit is inversely proportional to the square of the pulse duration, yet the thermal limit for the switching power is inversely proportional to the pulse duration, at very small pulse durations the quantum limit exceeds the thermal limit. The crossover point is at

$$\begin{aligned}\tau &= \hbar/kT \\ &= 2.5 \times 10^{-14} \text{ s.}\end{aligned}$$

At pulse durations less than this value, the quantum effects will exceed the thermal effects.

Therefore, at any pulse duration greater than  $2.5 \times 10^{-14}$  sec one can theoretically decrease the minimum switching energy per pulse by reducing the temperature of the switching device until one reaches the quantum limit.

### C. Shot Noise Limits

Shot noise may present a significant problem for reliable switching. The photon shot noise  $\Delta N_{\text{photon}} = N_{\text{photon}}^{1/2}$ . If we assume that we need 1000 photons for reliable switching, our lower limit on energy becomes

$$\Delta E_{s,s} = 1000 h\nu$$

where  $h$  = Planck's constant  
 $\nu$  = optical frequency

The corresponding power is  $P_{s,s} = \Delta E_{s,s}/\tau$   
at  $\tau = 10^{-12}$  sec and  $h\nu = 1.5$  eV

$$\begin{aligned}\Delta E_{s,s} &= 2.4 \times 10^{-16} \text{ J} \\ P_{s,s} &= 2.4 \times 10^{-4} \text{ W.}\end{aligned}$$

The shot noise limit has the same pulse duration dependence as the thermal limit and provides a larger lower bound than the thermal limit. Even with a smaller number of photons per pulse (i.e., <1000) the shot noise limit will likely exceed the thermal limit. The number of photons per pulse will be determined by the allowed error rate for the switching process.

#### D. Heat Transfer Limits

Yet another thermal factor for optical switching is given by heat transfer effects and the maximum allowable temperature rise in the switching element. This effect limits the number of switches dissipating power per unit area. For optical switching the maximum dissipation energy per switch is limited by

$$\frac{\Delta E_{s,m}}{\lambda^2 \tau} < I_m$$

Here  $I_m$  = thermal transfer limited power/area  
 $\lambda$  = optical wavelength  
 $\tau$  = pulse duration

$I_m$  is known to be limited to approximately 1000 W/cm<sup>2</sup> with the use of microchannel cooling technology and known materials for both substrates and convective fluids.<sup>9</sup> If optical switching is used,  $I_m$  may be significantly less than 1000 W/cm<sup>2</sup> because microchannel convective cooling may not be compatible with the optical elements and this value of power/area assumes a maximum temperature use of approximately 50°C. For these reasons the use of a value of 1000 W/cm<sup>2</sup> is likely an overestimate of the corresponding  $\Delta E_{s,m}$  value. This is particularly true for any device that exploits a resonant nonlinearity. One should also note that microchannel cooling technology is likely better suited to reflection mode devices rather than transmission mode optical switches.

The switching limit  $\Delta E_{s,m}$  places an upper bound on the dissipated switch energy rather than a lower bound such as  $\Delta E_{s,q}$  and  $\Delta E_{s,t}$ . However, in a device it is possible to have a larger  $\Delta E_{s,m}$  if the device is not operated at

the maximum repetition rate,  $1/\tau$ , or if the area per switch is greater than  $\lambda^2$ .

## VIII. FOUR WAVE MIXING AND OPTICAL COMPUTING IN NONLINEAR POLYMERS

One potential way of utilizing the large nonresonant nonlinearity of nonlinear polymers is with optical four wave mixing.

With four wave mixing, the signal is generated by a nonlinear optical interaction in the nonlinear optical interaction in the *nonlinear material*. Here

$$E_s = \chi^{(3)} E_1 E_2 E_p$$

Here  $E_s$  is the output signal wave amplitude

$E_1$  is the amplitude of input 1

$E_2$  is the amplitude of input 2

and  $E_p$  is the probe wave amplitude.

An example of a logic AND gate is schematically illustrated in Figure 4.

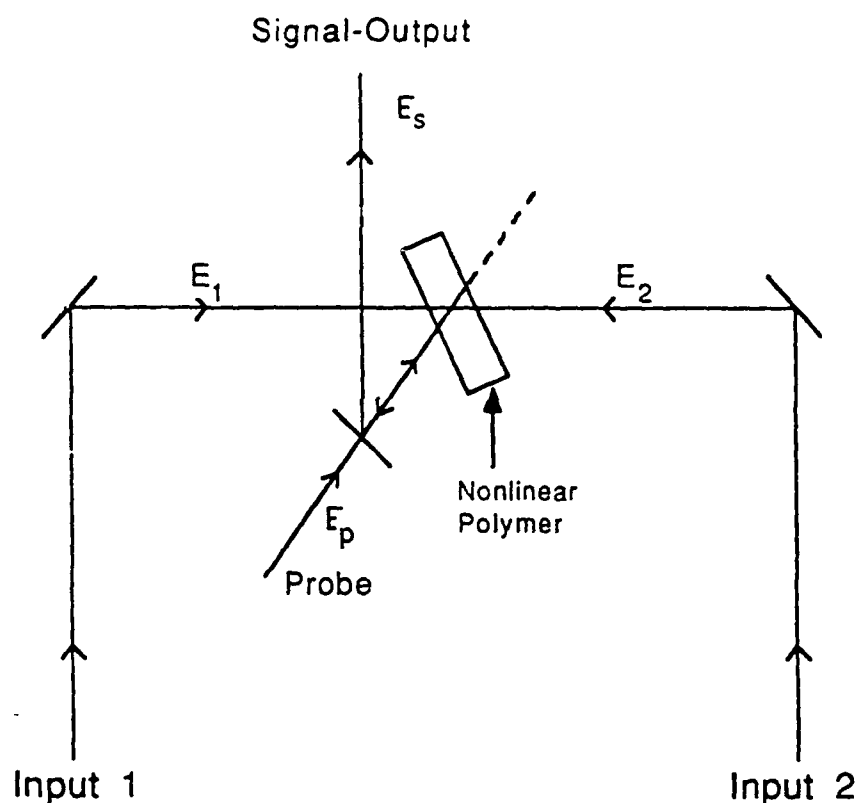


Figure 4. Four Wave Mixing AND Gate

In order to generate other logic operations from four-wave mixing one also needs a NOT operator. One way of creating this operation is to use an interferometer. Here one can use a reference wave with amplitude  $E_r$  such that the output amplitude  $E_{out}$  is  $E_{out} = E_{in} - E_r$ . When  $E_r = 1$  then  $E_{out} = 1$  if  $E_{in} = 0$  and  $E_{out} = 0$  if  $E_{in} = 1$ .

Other logic operators may be constructed by combinations of NOT and AND operators e.g.,

$$a \text{ XOR } b = \overline{(a \text{ and } b)} \text{ and } (a \text{ and } b).$$



Because nonlinear polymers have a very large  $\chi^{(3)} \sim 10^{-10}$  e.s.u., they are among the best known materials for high speed four wave mixing. Multiple quantum well materials and other materials with resonant nonlinearities have even larger  $\chi^{(3)}$ , but are very sensitive to temperature and wavelength, have slower response time, and may exhibit very strong absorption and sample heating.

## IX. CONCLUSIONS

A review of several types of materials for optical signal processings shows the potential of nonlinear polymers for very high speed devices. With parallel processors based on optical switching devices, bit rates of  $>10^{16}$  bits/sec seem feasible [ $10^5$  channels,  $10^{11}$  Nz,  $\tau_p \sim 10^{-12}$  sec]. If reactive nonlinearities are used, absorption effects are minimized. Other materials show large effective nonlinearities due to a resonant Kerr effect, photorefractive effects or electroabsorption effects. Devices based on these materials will not have the fast response time of nonlinear polymers and may be very wavelength or temperature sensitive. Temperature insensitivity is likely to be a very important device feature for small ultrahigh-speed parallel processors. An example of optical logic AND gate based on four wave mixing demonstrates how nonlinear polymers can be used in low-loss switching devices.

## REFERENCES

1. R. W. Keyes, Science 168, 796 (1970); 230, 138 (1985); R. W. Keyes, Optica Acta 32, 525 (1985).
2. D. S. Chemla, Rep. Prog. Phys. 43, 1191 (1980); J. Zyss, J. Mol. Electron. 1, 25 (1985).
3. G. M. Carter, Y. J. Chen, S. K. Tripathy, Appl. Phys. Lett. 43, 891 (1983).
4. D. A. B. Miller, D. S. Chemla, D. J. Eilenberger, P. W. Smith, A. C. Gossard, W. Wiegman Appl. Phys. Lett. 42, 925 (1983):
5. A. Ashkin, G. D. Boyd, J. M. Dziedzic, R. G. Smith, A. A. Ballman, K. Nassau, Appl. Phys. Lett. 2, 72 (1966).
6. A. M. Glass, Opt. Eng. 17, 470 (1978).
7. P. Guenther, Phys. Rep. 93, 199 (1982).
8. D. A. B. Miller, D. S. Chemla, T. C. Damen, T. H. Wood, C. A. Burrus, Jr., A. Bossard, and W. Wiegman, IEEE J. Quantum Electronics QE-21, 1462 (1985).
9. D. B. Tuckerman and R. F. W. Pease IEEE Elect. Dev. Lett. 2, 126 (1981).



# *MISSION of Rome Air Development Center*

*RADC plans and executes research, development, test and selected acquisition programs in support of Command, Control, Communications and Intelligence (C<sup>3</sup>I) activities. Technical and engineering support within areas of competence is provided to ESD Program Offices (POs) and other ESD elements to perform effective acquisition of C<sup>3</sup>I systems. The areas of technical competence include communications, command and control, battle management information processing, surveillance sensors, intelligence data collection and handling, solid state sciences, electromagnetics, and propagation, and electronic reliability/maintainability and compatibility.*